

ADDITIVE MANUFACTURING OF OXIDE DISPERSION
STRENGTHENED MULTI PRINCIPLE ELEMENT ALLOYS FOR FUTURE
AEROSPACE APPLICATIONS

by

LAURA G. WILSON

Submitted in partial fulfillment of the requirements

For the degree of Doctor of Philosophy

Thesis Adviser: Dr. Jennifer L. W. Carter

Department of Materials Science and Engineering

CASE WESTERN RESERVE UNIVERSITY

May, 2023

**Additive Manufacturing of Oxide Dispersion Strengthened Multi
Principle Element Alloys for Future Aerospace Applications**

Case Western Reserve University
Case School of Graduate Studies

We hereby approve the thesis¹ of

LAURA G. WILSON

for the degree of

Doctor of Philosophy

Dr. Jennifer Carter

Committee Chair, Adviser
Department of Materials Science and Engineering

Date

Dr. John Lewandowski

Committee Member
Department of Materials Science and Engineering

Date

Dr. Laura Bruckman

Committee Member
Department of Materials Science and Engineering

Date

Dr. Claire Rimnac

Committee Member
Department of Mechanical and Aerospace Engineering

Date

¹We certify that written approval has been obtained for any proprietary material contained therein.

To my many graduate school friends who weathered this storm alongside me and without whom I couldn't have made it. To my parents and sister who have always been there to offer encouragement, hugs, and laughs. To everyone else in my support network who has helped me survive this process. And especially to my husband who is always by my side and forever reminding me that I can do it.

Table of Contents

List of Tables	vii
List of Figures	ix
Acknowledgements	xviii
Acknowledgements	xviii
Abstract	xix
Abstract	xix
Chapter 1. Introduction	1
Application	1
Aims	3
Approach	5
Project Success Terms	8
Scientific Insights	8
Chapter 2. Literature Review	10
High Temperature Materials	10
Powder Manufacturing: Mixing	18
Additive Manufacturing	19
Statistics	23
Conclusions	24
Chapter 3. Acoustic Mixing of Oxide Dispersion Strengthened LPBF Feedstock	26
Introduction	26
Experimental Methods	34
	iv

Results	40
Discussion	42
Conclusions	47
Chapter 4. AM Parameters' Effect on Printed ODS NiCoCr	49
Introduction	49
Experimental Methods	52
Results	64
Discussion	78
Conclusions	94
Chapter 5. Overall Conclusions	96
Powder Experiment Conclusions	96
Printed Material Conclusions	98
Overall Conclusion	101
Scientific Contributions	102
Chapter 6. Future Research	104
Optimization Studies	104
Powder particle size vs Porosity	105
Strength vs grain size	105
Multivariate Linear Models and Beyond	106
Material Alternatives	106
Micro-Fatigue and Full-Scale Fatigue Comparisons	107
Appendix A. Supplemental Experiments	108
Introduction	108

Particle Size Distribution	108
Morphologi Powder Dispersion Tool	109
Appendix B. Tension Test Result Figures	110
Appendix. Complete References	114

List of Tables

3.1	Various techniques to quantify nanoparticles and their pros and cons for assessing the distribution of yttria nanoparticles dispersed in a NiCoCr matrix.	33
3.2	The polishing routine for mounted powder samples of Ni-base superalloys, done at NASA Glenn. This routine was followed by a vibratory polish with 0.5 μm colloidal silica suspension for 24 hours.	39
3.3	Classification results from qualitative analysis of SEM and EDS image data.	45
4.1	Summary table of the mixing conditions and time parameters that define each mix set.	54
4.2	The polishing routine for printed samples of Ni-base superalloys, done at CWRU	58
4.3	Test matrix for tension tests. Each of these samples was prepared using mixing parameter Set 1 (mixing condition C, time 2t).	64
4.4	Tension test results in both SI and metric units. Yield stress is calculated at 0.2% of the yield. The sample names represent the two room temperature (RT1 and RT2) and 2000	
	°F elevated temperature (ET1 and ET2) specimens.	75
4.5	Measured density values following Equation 4.3 and using the data from this study. (* the $V_f(\text{oxide})$ values are the average values of the	

	normalized amounts of yttrium calculated from the TOF-SIMS results on the bulk samples.)	79
4.6	Table of the porosity % values experimentally measured (averaged across the four mixing conditions with standard deviation in parentheses) and porosity % values calculated from the multivariate linear model equation.	84
4.7	Comparative table of yield strengths for elevated temperature tension tests.	91

List of Figures

- 1.1 This is the process flowchart that the dissertation follows. The colored lines moving around the flowchart represent the individual process loops and are explained in the key. The loops start at the white triangle, move through the main stages of the process (Processing, Microstructure, and Properties, represented in the three colored circles around the outside of the flowchart), and feed into the models. Subsequent loops are informed by the models and then "pass go" and start again. 6
- 2.1 Schematic showing the powder bed fusion additive manufacturing process. Powder, stored in the hopper, is spread over the retractable build plate, a laser melts the powder in a specific pattern, the powder bed is lowered, and the process repeats. 20
- 2.2 3D render of the multi-feature block used in this study, similar to the Gao block. Two views of the same block CAD model are shown to reveal all features. 22
- 3.1 Images of the mixed powder in the mixing containers after (a) 0.5t time, (b) t time, (c) 1.5t time, and (d) 4t time. After 1.5t time, the appearance of the mixed powder does not change significantly. The NiCoCr metal powder is gray and the yttria powder is white. 36
- 3.2 The jar on the right is bowed as a result of overheating. On the left is a new jar for comparison. The yellow lines highlight the difference. 36

3.3	This is the DOE matrix for the TOF-SIMS semi-quantitative surface chemical analysis, showing the 17 mixing parameter combinations used for powder analysis.	37
3.4	Normalized TOF-SIMS results of yttria (Y/Co), within the mixing parameter space.	40
3.5	This is the TOF-SIMS results of yttria, within the mixing parameter space defined by the mixing parameter matrix, showing the 17 mixing parameter combinations used for powder analysis. The boxes are colored by a hue scale, with darkest hue representing the lowest amounts of yttrium and lightest hue representing the highest amounts of yttrium.	41
3.6	Comparison of TOF-SIMS results from the powder samples (from Figure 3.4) and representative SEM images (BSE) from powders mixed with the same parameters. The visually obvious higher and lower amounts of oxide on the metal powder surfaces correspond to the amount of yttrium calculated via TOF-SIMS analysis.	42
3.7	Comparison of secondary electron SEM images of uncoated (a) NiCoCr and ODS NiCoCr with a thin coating (b) and thicker coating (c) of the oxide powder, relating to no mixing, low mixing time and condition, and higher mixing time and condition, respectively. The uncoated powder image is supplied from Dr. Tim Smith.	43
3.8	Comparison of good and poor ODS coatings. (a) shows a secondary electron image of a sample with inconsistent coverage on less than 25	

	percent of the surface, while (b) shows a secondary electron image of a sample with fairly consistent, greater than 75 percent coating surface coverage. (c) shows the EDS spectral image of yttrium for a sample with inconsistent coverage with many patches and clumps, and (d) show an EDS spectral image of yttrium with consistent coverage on all particles.	44
3.9	This is the DOE matrix for the qualitative analysis, showing the 9 mixing parameter combinations used for powder analysis. The darkest hue boxes represent poor mixes, the lightest hue represents the best mix, and the hues in between represent fair mixes based on the qualitative classification results.	46
4.1	Large yttria agglomerations, several indicated by the arrows. For scale reference, the diameter of the white sample jar is nominally 2 inches.	55
4.2	Gao block layout on the build plate with normalized print parameters along the outside.	56
4.3	Setup for collecting Archimedes' density. The setup includes the wire sample holder (dry holder: A and submerged holder: D, with attaching points: E), beaker (B) for holding the liquid (C), laboratory scale (F), and beaker stand (G).	57
4.4	Sample from Set 3, built with 1 <i>p</i> laser power and 1 <i>ss</i> scan speed. The left image (a) is the stitched micrograph of the polished sample cross-section. The right image (b) is the same micrograph after segmentation.	59

- 4.5 Sample from Set 2, built with 1.6*p* laser power and 1.3*ss* scan speed. The left image (a) is a segment of the SEM micrograph. The dark spots are the oxide particles. The right image (b) is the same micrograph after segmentation, with the mask applied on top of the oxide particles. 62
- 4.6 Schema of the design for ~2.5 inch (6.35 cm)long, ~0.25 inch (0.635 cm) diameter cylindrical tensile samples having $\frac{1}{4}$ – 20 threaded ends tapering down to a smooth, ~0.125 inch (0.317 cm) diameter gauge section, which satisfy ASTM Standards E8¹ and E21² for room temperature and elevated temperature tensile testing, respectively. The complete engineering drawing is shown in Appendix B Figure B.5. 63
- 4.7 Density of samples from each mix set (color), in a grid of AM parameters. Each data point represents the average value, and error bars show one standard deviation. 65
- 4.8 Porosity of samples from each mix set (color), in a grid of AM parameters. Each data point represents the average value, and error bars show one standard deviation. 66
- 4.9 Porosity plotted against density, with normalized scan speed represented by color and normalized laser power represented by shape. The linear regression line is shown in blue. 67
- 4.10 Porosity (less than 1%) plotted against density, with normalized scan speed represented by color and normalized laser power represented by shape. 68

4.11	Number of grains (edge grains excluded) from EBSD Grain ID Maps, in a grid of AM parameters.	69
4.12	Grain aspect ratios with error bars (edge grains excluded) from EBSD Grain ID Maps, in a grid of AM parameters.	70
4.13	An EBSD map from a representative sample (Set 3, laser power $1.6p$, scan speed $1.4ss$ (a.k.a. build location 33)), showing the elongated grain structure parallel to the build direction (z-direction). The build direction is up-and-down relative to the 3D printer axes, and left-to-right in the orientation of the EBSD analyses.	71
4.14	Distribution of the number of yttria particles detected from the oxide image analysis in the bulk samples from each mixing condition set, regardless of printing parameter.	72
4.15	Distribution of the number of yttria particles detected from the oxide image analysis in the bulk samples from each mixing condition set, organized by printing parameters.	73
4.16	TOF-SIMS results of yttrium, from multiple locations in four printed samples.	74
4.17	SEM secondary electron images showing both sides of the broken room temperature tensile samples. RT1 = top (a,b), RT2 = bottom (c,d). The images show the mirrored halves exhibiting the cup-and-cone structures from ductile fracture and necking represented by the smaller area of the fracture surface compared to the rest of the gauge section.	76

- 4.18 SEM secondary electron images showing both sides of the broken 2000 °F tensile samples. ET1 = top (a,b), ET2 = bottom (c,d). The flatter fracture surface and lack of significant necking is indicative of a brittle fracture. 77
- 4.19 SEM secondary electron images showing a 0.5mm x 0.5mm close-up of part of ET2, a 2000 °F tensile samples. Features which are likely weld pools are visible (average width 0.055 mm), an example of which is marked with the two-headed arrow. 78
- 4.20 Porosity (less than 1 %) plotted against density, with normalized AM parameters represented by color and shape. Plot axes are switched from Figure 4.10 so porosity (i.e. volume fraction) is on the x-axis. The upper boundary of the rule of mixtures, calculated from equation 4.4, is shown in the plot as well. 80
- 4.21 Porosity vs build parameter plot (top,a). The bottom plot (b) shows approximate zones for keyholing, lack of fusion, and optimum in relation to laser power and scan speed. The dashed black box represents the approximate location of this dissertation's data. 82
- 4.22 Porosity vs build parameter plot with the multivariate linear model overlaid in color. The same color scales apply to the points (measured values) and the background (predicted) for porosity. The white line represents porosity = 1%, with the space below the line representing porosity <1. 83

- 4.23 Residuals plot from the porosity vs processing parameters model. The non-random nature of the residuals indicate that a non-linear model would have fit better with the data. 85
- 4.24 Average grain size for each sample plotted against build parameters. The background gradient shows the predicted values according to the model and the points represent the measured values. The same color scale applies to both predicted and measured values. The model has $R^2 = 0.57$. 86
- 4.25 Average number of grains per sample plotted against build parameters. The background gradient shows the predicted values according to the model and the points represent the measured values. The same color scale applies to both predicted and measured values. The model has $R^2 = 0.70$. 87
- 4.26 Residuals plot from the average grain size vs processing parameters model. The random nature of the residuals indicate that a linear fit was appropriate for the model. 88
- 4.27 Residuals plot from the number of grains vs processing parameters model. The random nature of the residuals indicate that a linear fit was appropriate for the model. 89
- 4.28 Yield strength of materials similar to ODS NiCoCr from room temperature tensile tests. The ODS NiCoCr from this work is marked with a star. The data points are grouped by material category, colored by fabrication category, and represent data from multiple studies.³⁻¹⁶ 91

4.29	Room temperature engineering stress-strain tensile test results for non-mixed NiCoCr, ODS NiCoCr mixed with different parameters than this project, and ODS NiCoCr from this dissertation (bold). This figure shows data from both this dissertation and Smith et al., 2020. ¹⁷	94
4.30	Elevated temperature engineering stress-strain tensile test results for non-mixed NiCoCr, ODS NiCoCr mixed with different parameters than this project, and ODS NiCoCr from this dissertation (bold). This figure shows this dissertation's data added to the results from Smith et al., 2020. ¹⁷	95
5.1	Results of the qualitative analysis (a) and the semi-quantitative analysis (b) both imposed on the mixing parameter matrix. Both tables follow a similar hue map coloration, with darkest boxes representing poor coatings with less yttrium, lightest boxes representing good coatings with the most yttrium, and intermediate boxes representing intermediate values.	98
5.2	Results of the screening analyses. The left plot (a) shows the results of the EBSD analysis of the grain size and the right plot (b) shows the porosity results. Both plots are colored following the models of the respective analyses and indicate the idealized AM parameters are indicated in the lower-left corner (1.3-1.6 for laser power and 1-1.2 for scan speed).	99
5.3	Results of the engineering stress-strain tension tests on idealized LPBFAM produced ODS NiCoCr material. The top plot (a) shows the	

	stress-strain curve from the room temperature tension tests, and the bottom plot (b) shows the stress-strain curve for the elevated temperature tension tests. Both plots include results from this analysis as well as the material printed from the similar project at NASA Glenn ¹⁷ .	100
5.4	Results of the oxide distribution result (a) and the TOF-SIMS results (b) from the idealized printed samples. The results from Mix Set 1, which is mixing condition C and time 2t, shows a wider distribution of values, as indicated by the height of the box in both box plots. This suggests an inhomogeneous oxide distribution.	101
B.1	Engineering stress/strain curves for room temperature tensile tests.	110
B.2	True stress/strain curves for room temperature tensile tests.	111
B.3	Engineering stress/strain curves for 2000 °F tensile tests.	111
B.4	True stress/strain curves for 2000 °F tensile tests.	112
B.5	Engineering drawing for the threaded tensile specimens.	113

Acknowledgements

0.1 Acknowledgements

This research was funded through a NASA Aeronautic Scholarship and Advanced STEM Training and Research Program Fellowship.

Thanks are owed to Dr. Jennifer L. W. Carter, Dr. Timothy M. Smith, and Dr. David L. Ellis for their advice, insight, and mentoring throughout the entire research project and graduate school career.

The authors would also like to thank NASA Glenn collaborators, including Wayne Jennings, Pete Bonacuse, Joy Buehler, and Dr. Cheryl Bowman, for their support and facilities assistance.

Additional thanks are owed to NASA Glenn engineer Josh Stuckner for his image analysis code and oxide distribution analyses described in Chapter 4.

Many of the analyses were performed with facilities at Case Western Reserve University, and the authors would specifically like to thank Dr. John T. K. Kim, Dr. Jeff Pigott, Nichole Hoven, and Dr. Ina Martin for their help and expertise. TOF-SIMS was conducted at the Case School of Engineering, Swagelok Center for Surface Analysis of Materials (SCSAM). Financial assistance for instrument time and scientific training was provided by the SCSAM Fellowship program which is supported by The Swagelok® Center for Surface Analysis of Materials Endowment Fund. Porosity macros were written by and used with the assistance of David Scannapieco. The authors would also like to thank Caroline Horn and David Walker for their assistance with sample polishing and Archimedes' density data collection, respectively.

Abstract

Additive Manufacturing of Oxide Dispersion Strengthened Multi Principle Element Alloys for Future Aerospace Applications

Abstract

by

LAURA G. WILSON

0.2 Abstract

Oxide Dispersion Strengthened (ODS) materials have long been of interest for their high temperature applications, and additive manufacturing enables their manufacturing viability. The ODS multi-principle element alloy NiCoCr was prepared using powder metallurgy techniques, additively manufactured, and evaluated for its processing-microstructure-property relationships. The high temperature foundations of nickel-base superalloys and ODS materials were combined with the manufacturing advantages of 3D printing and the chemical simplicity of NiCoCr to inspire this work, which was divided into powder and printed material assessments. The project was achieved through multiple iterative project loops to assess the processing parameters' impact on the microstructure and mechanical properties of the feedstock powder and printed material. The powder investigations (Chapter 3) focused on understanding the oxide coating that formed on the metal powder following acoustic mixing. Time of Flight Secondary Ion Mass Spectrometry was used to semi-quantitatively assess the amount of yttrium on the

surface of the mixed powders, and indicated that a combination of higher mixing condition energy and moderate mixing time resulted in the most oxide coating on the NiCoCr powder. The results were supported by a qualitative assessment of scanning electron images of coated powder particles. Following mixing, the ODS NiCoCr was consolidated by Laser Powder Bed Fusion. The evaluations of the printed material (Chapter 4) first considered screening experiments including Archimedes' density, porosity, and grain size and number metrics from electron backscatter diffraction data. After the ideal additive manufacturing parameters were identified, both the oxide homogeneity and yield strength were discussed for the idealized printed material. Overall, the project suggests that the combined use of qualitative or semi-quantitative powder surface analysis with Archimedes' density analyses can be a valid high-throughput technique which can lead to process optimization of Laser Powder Bed Fusion additively manufactured ODS material.

1 Introduction

1.1 Application

The aerospace industry is always looking to push the temperature limits of materials to improve fuel efficiency. Researchers have for decades studied high temperature materials that can push that ceiling for components in the hot section of turbine engines.^{18–21} Components in turbine engines such as turbine blade edges must be designed to face high centrifugal and thermal stresses combined with steep temperature gradients.²⁰ Ni-based alloys have filled this role for decades, and advances continue to be made regarding their temperature capabilities, oxidation and corrosion resistance, and stress tolerance so that they may better fit that role.^{18–21} Alternative materials which can operate beyond the temperature range of Ni-based alloys necessitate the use of carbon/carbon composite materials and refractory metals. At temperatures above those, ultra-high temperature ceramics are required.²⁰

NASA has long been interested in high-temperature materials research for use in turbine engines, too, along with rocket combustion chambers, reentry vehicle surfaces,

and advanced space power systems. NASA Glenn Research Center has been at the forefront of NASA's material research front with advances to Ni-based superalloys for turbine engines since the 1950s, and continues to be interested in developing high temperature materials for improved emissions and safety.²¹ The National Strategy for Advanced Manufacturing, as well as NASA's Technology Taxonomy outlines the continued need for high-temperature materials and additive manufacturing to produce complex-shaped parts for future aerospace missions.^{22,23}

Nickel-base superalloys have for decades been the material of choice for researchers studying high temperature applications in the aerospace industry. Multi-principle Element Alloys (MPEAs) have also been studied in the past couple of decades as a high-temperature material. Both of these groups of materials face a similar problem in the temperature limitations of their primary strengthening mechanisms, however. In order to make significant strides past those temperature limits, composite materials involving the integration of higher-temperature phases are required. Previous studies have shown temperature increases with additions of single elements (Mo²⁴, Ti^{25,26}, and Al²⁶), other nano-sized particles²⁷, as well as with oxides.^{19,28,29}

This dissertation is evaluating a high temperature composite material, an oxide dispersion strengthened (ODS) multi-principal element alloy ODS NiCoCr. ODS materials were well studied in the 1960s-1980s time frame, and were considered to be a "silver bullet" in terms of increasing the temperature capability of nearly any alloy.³⁰ Much of the research into ODS materials was halted, however, due to the high level of difficulty and high costs associated with manufacturing ODS alloys. ODS alloys were traditionally manufactured with hot-dye extraction followed by complex cold working and processing to make the required shapes with specific properties of interest, an often difficult

and timely process.^{19,30–32} Many of the ODS material manufacturing challenges can be overcome now, however, with the use of additive manufacturing (AM).

AM, and specifically laser powder bed fusion (LPBF) AM, allows for low-cost, low material waste consolidation of metal components from powder feedstock material. Powder metallurgy allows for high chemical accuracy and customization of the material to be manufactured.^{33,34} LPBF AM can produce complex-shaped parts with little to no post-working needed.^{35,36}

AM is the key technology that enables the simple and cost-effective production of ODS components, which have higher temperature capabilities than Ni-based superalloys or MPEAs alone, in the complex shapes required for engine components in the aerospace industry. AM of ODS MPEA material (NiCoCr for this dissertation) further enables this through a simpler material that allows for the focus of the investigation to be on the ODS material and not the complicated chemical reactions occurring during the various processes.

1.2 Aims

This dissertation begins with an literature review of relevant topics (Chapter 2), and then the work is broken into two main parts, before a final discussion chapter (Chapter 5) and a chapter dedicated to future work (Chapter 6). The first main part (Chapter 3) deals with understanding the effect of the powder preparation parameters on the quality of the oxide distribution AM feedstock material. The powder is prepared via acoustic mixing with a Resodyn acoustic resonance mixer.³⁷ While there are several parameters at play

during the complex mixing process, the main two parameters that influence the quality of the mix are the mixing time and a mixing condition energy¹.

Mixing energy and mixing time are the main variables that can impact the powder mix in the acoustic mixer.^{37–39} An initial qualitative analysis of ODS NiCoCr powder (discussed in Chapter 3.4) revealed a significant difference in the amount of oxide (yttria) powder coating the surface of the NiCoCr powder following various mixing parameter combinations. The literature-supported concepts of the mixing parameters' impact on the mixed material along with the initial qualitative experimental results combined to inspire the first project aim.

The second part of this dissertation work (Chapter 4) explores the impact of the AM parameters on the resulting microstructure and mechanical properties of the LPBF printed parts. A number of studies have concluded that the microstructure of LPBF printed components are impacted by the printing parameters, specifically laser power and scan speed, but also hatch spacing and layer thickness.^{40–42}

This dissertation focuses on the impact of laser power and scan speed; especially in relation to printed part porosity, laser power and scan speed have been shown to have an impact. Several studies have shown that too low laser power combined with too high scan speed can result in incomplete melting of the material, that lower scan speeds can lead to more complete melting, and that too high laser power can result in deleterious over-melting effects that lead to cracking and porosity. All studies agree that a balance in parameters must be found that results in idealized microstructure and mechanical properties.^{41,43–45} It was therefore an essential aim of this dissertation to investigate and

¹As this is a NASA funded dissertation, some of the values discussed in this work have intellectual property sensitivity, and therefore are normalized. In particular, the manufacturing parameter values are normalized.

find the balance of AM parameters that resulted in LPBF produced ODS NiCoCr with idealized microstructure and mechanical properties.

1.3 Approach

An iterative process was designed to most efficiently work through the dissertation. The knowledge gained from initial experiments and evaluations informed a more efficient parameter selection for successive experiments and directed the aspects of the project that required further scrutiny. This manner of project flow not only allowed for efficient use of time and materials, but also conformed to the iterative study design concepts of reworking and convergence, which involves step-wise improvements to parameters to achieve defined goals.⁴⁶ While the importance of iterative study designs are well documented,^{46,47} few studies employ and document this approach in the published content of their research, unlike the present dissertation, which does.

The project flow was built around materials science's ubiquitous Processing - Microstructure - Properties (P|M|P) triangle. The Processing stage of this dissertation consists of both powder processing and additive manufacturing. The Microstructure and Properties stages include evaluations of the powder and printed bulk material. The combination of data from powder processing, additive manufacturing, microstructure analyses, and mechanical testing feeds into statistical models that inform the different steps of the project as well as the final process map (Figure 1.1 provides a graphical representation of the overall dissertation flow). The flowchart illustrates how this is an iterative process: the knowledge gained during one process loop feeds into the models and informs the next process loop; the information from the previous loop is crucial to the design of the next.

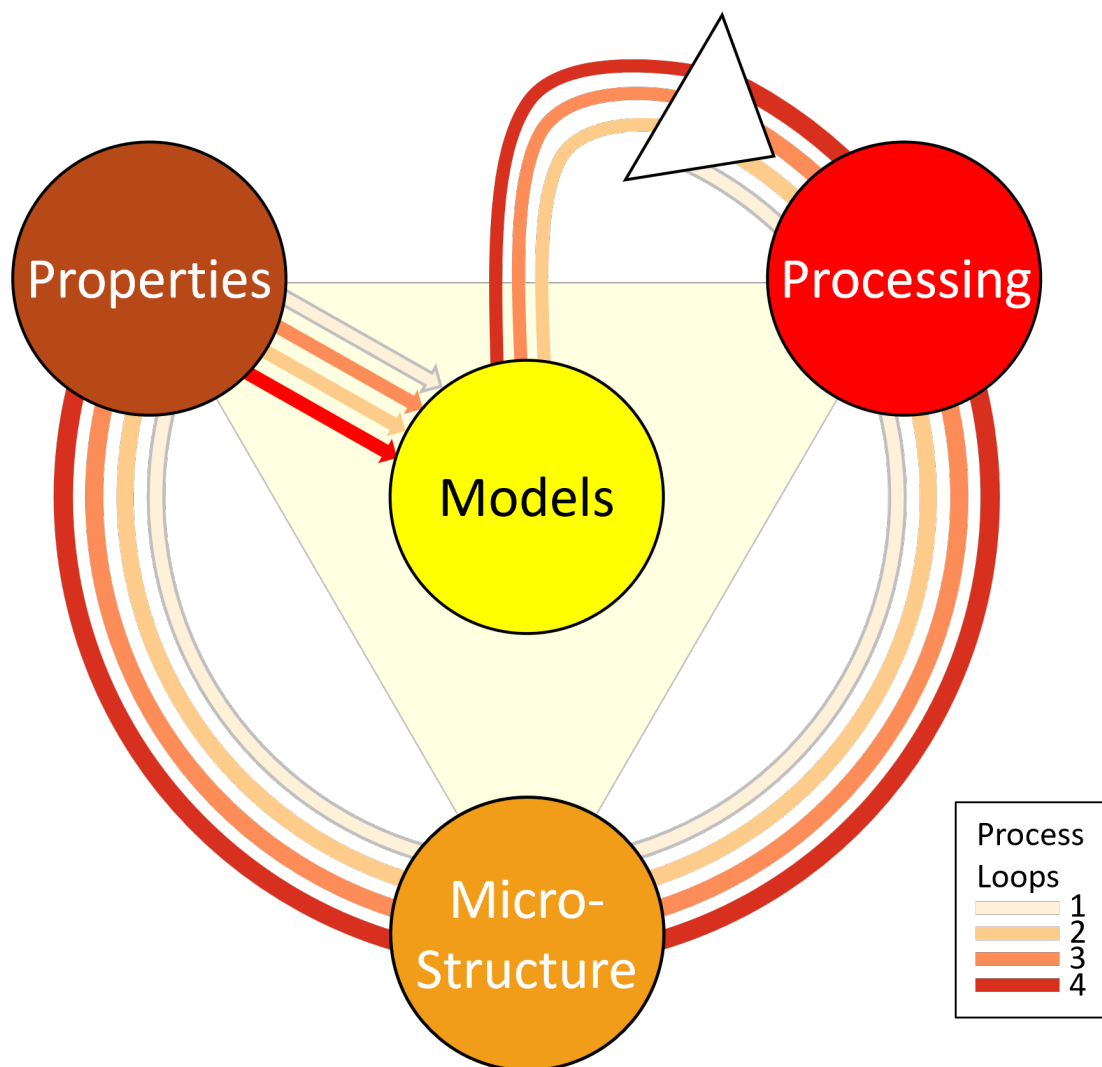


Figure 1.1. This is the process flowchart that the dissertation follows. The colored lines moving around the flowchart represent the individual process loops and are explained in the key. The loops start at the white triangle, move through the main stages of the process (Processing, Microstructure, and Properties, represented in the three colored circles around the outside of the flowchart), and feed into the models. Subsequent loops are informed by the models and then "pass go" and start again.

Along with iterative study design, the dissertation also followed the principles of a design of experiments (DOE) approach in conjunction with the project loops.⁴⁸ The first loop consisted of qualitative comparisons with the mixing time and mixing condition as

the factors. Subsequent loops progressed to the screening/characterizing areas where the goal was to quantitatively understand the process and investigate the more and less important factors, based on models. Initial, linear modeling was included in the project to determine the mathematical relationship between the factors (AM parameters in this case) and the output (microstructure and properties). While the dissertation did not move into the optimization area of DOE, many of the steps leading up to it were completed, and the concepts are discussed in the Future Work chapter (Chapter 6).

The first aim of the dissertation is quantitatively investigated through a powder coating analysis by Time of Flight Secondary Ion Mass Spectrometry (TOF-SIMS). Seventeen powder samples are mixed, each with a different combination of mixing time and mixing condition. TOF-SIMS is then used to semi-quantitatively evaluate the amount of yttria on the surface of the NiCoCr powder. These semi-quantitative results are related to the qualitative investigation of oxide coating quality, which involved scanning electron microscopy (SEM) images and Energy Dispersive Spectroscopy (EDS) analysis of powder samples mixed with nine parameter combinations.

The second project aim focuses on a screening evaluation of the microstructure and properties (porosity, density, grain size, number of grains, and oxide distribution) of multi-feature blocks printed by LPBF AM with three different laser powers and three different scan speeds. These AM parameters' impact on the Archimedes' density is first considered and how that relates to material porosity. Electron Backscatter Diffraction (EBSD) was used to gather grain metrics on the printed material, and the scan speed and laser power's impact on the grain size and number of grains is investigated and modeled.

These screening experiments yielded idealized printing parameters which were used to print tensile samples (which were tested and compared to similar materials) and to investigate the oxide distribution in printed samples.

1.4 Project Success Terms

Based on the criteria that the oxide in ODS materials needs to be homogeneously distributed^{19,30,49}, the oxide coating quality following various mixing parameter combinations was evaluated on consistency. A more consistent and even coating (as determined during the qualitative analysis) correlated with more oxide detected in the TOF-SIMS experiments.

The screening evaluations of the printed material operated on the concept that in order to have mechanical properties comparable to traditionally manufactured material, AM materials should be fully dense.^{35,36,50,51} It was also considered that, at moderate to low temperatures, Hall-Petch strengthening is the dominant strengthening mechanism^{52,53}, so a higher number of grains would be more ideal. At high temperatures, however, which is of more interest for the ODS NiCoCr material, Orowan strengthening is dominant^{26,27,52,54}, so homogeneous oxide distribution in the printed material with larger grains was the mark of success.

1.5 Scientific Insights

Not only is ODS NiCoCr a new material and part of a process that was developed and patented at NASA Glenn during the dissertation, but the dissertation presents a number of novel ways to characterize this material and similar materials. The application of

iterative process loops is a well understood though seldom applied approach to experimental design as reported in the literature.^{46,47,55}

In terms of powder analysis, this dissertation's use of TOF-SIMS to semi-qualitatively evaluate the oxide coating on acoustically mixed ODS NiCoCr samples is a novel contribution to the field. At the time of this dissertation, TOF-SIMS has not been used to evaluate oxide coated metal powders. The methodology outlined in this study is applicable to other coated powders as well. The qualitative framework for characterizing the powder surface, as described in this dissertation, can also be applied to a variety of materials and serves as a characterization guide.

Additionally, while the relationship between AM parameters is documented in innumerable studies,^{e.g. 36,41,56} this study presents numerical models to quantify the relationship between the laser power and scan speed and the printed material microstructure. This dissertation also documents the use of Archimedes' density measurements as a quick screening tool.

2 Literature Review

2.1 High Temperature Materials

High temperature materials are those which are capable of withstanding constant or quickly cycling temperatures and varying levels of operating stress. High temperature materials must also exhibit oxidation resistance at those temperatures.^{20,21} These and other high temperature materials have been greatly important to the aerospace industry due to the efficiency of power conversion's direct relation to operating temperature.²⁰ High temperature metals in aerospace are primarily used in hot sections of turbine engines, heat exchangers, and other power conversion components.¹⁸⁻²¹

Research into high-temperature materials at NASA Glenn Research Center has focused on not only turbine engine hot sections, but also rocket combustion chamber liners, the surface of atmospheric reentry vehicles, and space power systems. The research has specifically focused on understanding the processing - structure - property relationships of the high-temperature materials and the interactions with the harsh, application-specific environments.²¹ High-temperature materials research continues to fit into the current technology areas NASA will advance in order to achieve their future aerospace missions and activities.²²

Not only are NASA and other research agencies interested in higher-temperature materials, but there is significant interest in manufacturing these materials into complex-shaped components. Highly complicated metal components, such as combustor domes and compact heat exchangers are at the forefront of current high temperature materials research, and cannot easily be made with traditional, subtractive manufacturing techniques. These complicated shapes necessitate advanced manufacturing techniques like additive manufacturing (AM), which has been noted by numerous agencies including NASA.^{22,23,57,58}

2.1.1 Nickel-base Superalloys

Ni-based superalloys have been studied for decades as a high temperature material important to the aerospace industry. Over these decades, advances have come in the form of improved alloy compositions and novel processing alterations of Ni-based superalloys in order to increase their operating temperature.^{18,33,59} Nickel-based superalloys have been used for applications with temperatures up to tens of degrees above 1000 °C. Cr and Co have been alloying elements within nickel-base superalloys, for example, to act as oxidation resistance and solid solution strengthening elements.^{18,20,60}

In order to achieve the high temperature strengths that make Ni-based superalloys such a desired material, they need to contain a large variety of elements. These alloys contain elements to enable γ' precipitation strengthening and oxidation and corrosion resistance, which all combine to give these alloys notably stable properties up to 1000 °C, or around 60% of their melting temperature.^{18,33,51} These complex chemistries require very precise heating and processing in order to form the correct volume fraction and size of the γ' phases necessary for precipitation strengthening.³³ Nickel-base superalloys,

especially those with high γ' volume fractions, are, however, often difficult to thermomechanically process (i.e., working or forging) as they require specific microstructural processing to avoid cracking.^{43,44,51,61}

In addition to the complex processing requirements of Ni-based superalloys, the progress in increasing the temperature capabilities of Nickel-base superalloys has long been nearing an asymptote.¹⁸ The dissolution of the γ' precipitates, which is the main strengthening mechanism in Ni-based superalloys, presents a hard limit on the operating temperature of these materials.^{18,31,33,62,63} There is a need to transition from solid-solution strengthening to precipitate or dispersion strengthening, which are methods of strengthening alloys at temperatures above those at which precipitation strengthening is effective.^{31,63}

Issues surrounding the complex chemistry required by Ni-based superalloys contributed to the need for powder metallurgy (PM). Powder metallurgy started to become popular due to the ability to achieve high material purity and homogeneity, not to mention that powdered metal billets were easier to work and shape than their forged predecessors.^{33,59,64} Powder metallurgy also allows for the low-cost manufacturing of unique components not achievable with traditional manufacturing methods, due in part to PM's high material and energy efficiency.^{34,59}

Alloy powder is traditionally made by a prealloying process which can include mechanical milling, chemical methods, or atomization.^{34,65,66} Mechanical powder manufacturing methods include mechanical alloying and milling, both of which can alter the morphology of the original powders and potentially introduce contamination in the

form of either the a mixing additive or the grinding media.^{65,66} Chemical methods require a reaction medium in addition to the elements intended to be mixed.⁶⁵ Atomization methods can be used to create powder with a specific composition and size distribution, but is not a method to combine multiple dissimilar powders.^{66,67}

Once the powder is made with the correct alloy chemistry, PM parts have commonly been consolidated in a die with the aid of heat and pressure. It is difficult, however, to impart the consistent material density throughout a complex part with rigid die compaction.³⁴ PM parts also inherently contain porosity, for which the level is dependent on the consolidation methods and parameters, as well as heat treatments.^{33,34} Internal porosity is commonly reduced with hot isostatic pressing (HIP), but this can only alleviate porosity to an extent.^{33,34,40,43,60,68}

In addition to the porosity and consolidation issues inherent to PM, powder metallurgy superalloys, specifically, are considered difficult to extrude due in part to the high strain rates and intense controls required to produce the desired microstructure and mechanical properties.⁶¹ These difficulties arise from the complex chemistries of Ni-based superalloys, and despite the high chemical purity and customizability advantages of powder metallurgy, Ni-based superalloys are still considered difficult to manufacture.^{33,51,61} Multi-principle element alloys (MPEAs), on the other hand, are a class of material with less complex chemistries that have been studied as an alternative material for high temperature applications.^{69,70}

2.1.2 Multi-Principle Element Alloys (MPEA)

MPEAs, formerly referred to as high and medium entropy alloys (HEA and MEA respectively), have been developed and explored in since the early 2000s.⁷⁰ HEAs are composed of five or more elements (3 or 4 for MEAs) in near-equiatomic proportions to

originally promote solid-solution strengthening.^{9,24,71–73} They are described as having high configurational entropy among their elements, which favor a single solid solution phase (as opposed to the formation of intermetallic compounds). The simplified mechanism behind HEAs is a balance between entropy and enthalpy achieved through a minimization of Gibbs Free Energy.^{69,70} Diffusion is also said to be slow in HEAs, supported by several studies referring to high activation energies and difficult substitutional diffusion.⁷⁰

The CoCrFeMnNi family (known as the Cantor alloy) is one of the most widely studied HEA, from which NiCoCr has been shown to have a great strength, ductility, and toughness combination, with a melting temperature of 1690 K.^{8,25,71,72} NiCoCr is hardened through multi-phase regions (face-centered-cubic or primitive -FCC or FCP- normally with regions of hexagonal-close-packed -HCP), low stacking fault energy, and deformation twins, all which help to hinder deformation movement.^{71–76} This HCP (sigma) phase is Cr-rich, and has been shown form at temperatures at 700 C and lower, and to increase strength and decrease ductility.^{70,74,77}

While MPEAs alleviate many of the chemical complexities from Ni-based superalloys, they face a similar intrinsic strengthening asymptote derived from solid solution strengthening. In recent years, research has shifted to exploring elemental doping or other phase additions to induce precipitation strengthening in MPEAs. A study by He et al.²⁴, for example, combined thermomechanical processing with molybdenum-doping of an equiatomic NiCoCr MEA in order to increase its strength and ductility, which was achieved through precipitation hardening and hierarchically related recrystallized and non-recrystallized zones. The fully recrystallized Mo-doped NiCoCr MEA, aided by solid

solution strengthening from the Mo, exhibited a yield strength 12% higher than the non-doped NiCoCr MEA.²⁴ It has also been shown that micro-additions of Ti and C to NiCoCr promote equiaxed grains in drop-cast material. The Ti additions improved the tensile properties of the NiCoCr, primarily due to TiC forming as temperature stable particles that acted as heterogeneous nucleation sites for grain growth.²⁵ Elemental additions (of Al and Ti) to the FeCoNiCr matrix were shown to increase strength through formation of nanoscale precipitates, but that these precipitates dissolved at high temperatures (>800 °C).²⁶ While these studies have shown that precipitates can be used to impart strength to MPEAs, precipitates will always have an inherent stability limit lower than the melting temperature of the base alloy. This will result in similar asymptotic performance issues that currently hinder the advancement of nickel-base superalloys.

2.1.3 ODS

Dispersion-strengthened alloys lack the same performance asymptote of solid-solution strengthened alloys because they rely on strength from an ex-situ added dispersed phase. It has been noted from previous studies that precipitation and dispersion strengthening generally have a stronger effect on mechanical properties than solid-solution hardening, which supports the need for dispersion-strengthened materials in a variety of traditionally solid solution-strengthened alloys.⁷⁰ The dispersed phase is finely distributed within the crystalline matrix, which yields more strength than the matrix phase alone.⁷⁸ Regarding the size of the dispersed phase, it has been shown that nano-sized particles integrated into a metal matrix have a beneficial effect on the mechanical properties of the metal matrix material.²⁷

In ODS materials, the dispersed particulate phase is an oxide, traditionally thoria or yttria. These ODS materials were studied throughout the 1960s, 70s, and 80s, and were

thought of as a potential go-to solution for extending the high temperature capabilities of nearly any alloy system as they could remain stability at high temperatures, above 55%-70% (up to 90%) of the melting temperature of the pure metal alloy.^{26,30,79} Many commercial ODS alloys contain 0.5-1.3 (1.14 avg) wt% yttria.⁷⁹ The main interest in using oxides as the dispersed phase for circumventing the asymptotic temperature performance of nickel-based superalloys revolves around their stability and strengthening capabilities in the 800 °C to 1200 °C temperature range.^{30,34}

Not only do the oxide dispersoids add strength by providing stable particles of appropriate size within the matrix to pin defects at temperatures higher than that which other precipitates would dissolve, but these particles enable the retention of thermomechanically introduced strengthening mechanisms, too.³⁰ The yield strength of ODS materials is associated with the stress required to move dislocations along slip planes greater distances than the dispersoids are spaced apart.⁷⁸ The oxide dispersoids add strength to the material because they successfully pin grain boundaries and dislocations during processing and performance.⁸⁰ Dislocation motion in ODS materials is believed to be hindered by either direct interference from the dispersed particles or from the lattice strain induced from the matrix accommodating the dispersoids.⁷⁸ Regardless, it is well understood that Orowan type strengthening (particle strengthening through a dislocation bypass) is the dominant type of strengthening seen in the ODS samples.^{26,52-54,81,82}

ODS powders, like other PM materials, are typically made by mechanically alloying the oxide particles with the metal, then compacting and/or extruding at high temperatures in order to consolidate the material.^{26,32,60,79} The resulting consolidated billets exhibited some advantageous characteristics over comparable cast material, but tensile

and rupture ductility, for example, were lower, and parts required additional processing in order to achieve similar mechanical properties of traditional alloys.^{19,28,29,31} Another issue identified when creating complex parts from ODS materials was that the uneven distribution of cold work required to create the complex part shapes would result in larger variations of strength, as compared to wrought materials which would be forged into similarly complex shapes.³⁰ It was eventually believed that ODS materials would not be a cost-effective panacea over traditional cast or wrought materials, mainly due to manufacturing difficulties and expenses.^{30,31}

Precipitation strengthening, while similar to dispersion strengthening, does not involve an extrinsic phase addition. Precipitates can strengthen materials also through Orowan strengthening or Zener pinning (pinning of grain boundaries)²⁷, however the extrinsic addition of the dispersion phase reduces diffusion-mediated evolution. Diffusion strengthening also motivates the requirement for conventional powder manufacturing.

Oxide dispersion strengthened (ODS) Ni-based alloys and superalloys have been studied as a viable material improvement over solid-solution strengthened Ni-based superalloys.^{19,28,29} ODS and other precipitation strengthening mechanisms are most effective at high temperatures, while solid-solution strengthening remain effective at lower temperatures.^{52,53} In numerous studies, for example, it has been shown that ODS Ni-based superalloys did benefit from γ' precipitate strengthening at intermediate temperatures and dislocation pinning from the oxide dispersoids at high temperatures. Since the oxides are not precipitated from the melt, they are stable at higher temperatures where other precipitates (such as γ') would dissolve.^{19,29,30,78,79}

As with Ni-based superalloys, ODS has shown promise in MPEAs. Many studies have explored the benefits of ODS to increase the temperature capabilities of MPEAs. For example, a study of FeCoNiCr strengthened by yttria found that not only were ODS MPEAs feasible, but they can exhibit superior mechanical properties compared to non-ODS HEAs.²⁶ Another study investigated ODS CoCrFeMnNi and found that the oxides enabled ultrafine microstructures and increased tensile strength in the material.⁸³ One other study found that the addition of Mn to CoCrFeNi during the LPBF process formed oxides, and the resulting ODS material had high strength and intermediate ductility.⁸⁴ These and similar studies attribute strength and smaller grain sizes to the oxide particles ability to pin grain boundaries^{17,85}

2.2 Powder Manufacturing: Mixing

Alloy powders are traditionally prepared by both mechanical (ball milling and regular mixing) and non-mechanical (gas atomization, electrodeposition, agent-assisted deposition) mixing method.^{49,86} An additional powder preparation method, useful to create homogeneous composite powders, is acoustic mixing.

Acoustic mixing has been used to make powder blends in the pharmaceutical community, often in combination with a liquid to create a slurry.^{38,87} Acoustic mixing has been used in the materials science community, as well, both with and without the aid of a lubricant.^{17,86,88–90}

Acoustic mixing's use in powder processing of composite powders relies on electrostatic forces and cohesion between the particles and has been used in numerous studies.^{86,91} Han et al.⁹², used a high speed mixing technique, similar to acoustic mixing, to make a composite powder of 1 wt% TiC and Hastelloy X superalloy. They found that the

mixing technique resulted in an even distribution of the TiC particles on the surface of the metal particles. Mizes et al.⁹³, specifically explain how the Derjaguin approximation is used to estimate the force of Van der Waals and electrostatic attraction between particles. A basic description of this is that as the shape of the contact between particles gets sharper, the adhesion decreases. Soulier et al.⁸⁶, used various mixing techniques, including acoustic, to coat (roughly 35 μm) aluminum powder with (roughly 35 nm) satellite particles of SiC. They found that acoustic mixing lead to complete electrostatic adhesion of the nanosized guest particles and the Al host particles and that the forces in the acoustic mixing process helped reduce agglomeration of guest particles on the surface, as compared to the other mixing methods.

Regardless of how the powder is produced, powder consolidation issues still hinder the process.

2.3 Additive Manufacturing

In tandem with transitions in the design of nickel-base superalloys for high-temperature applications to make industries reliant on the powder metallurgy method, there has been the emergence of additive manufacturing which has the potential to solve challenges associated with manufacturing complex shapes from powder metallurgy compositions. Industrial and research interest in AM has boomed in the past couple of decades.^{35,36,41,68} AM offers several key cost and manufacturing benefits, while allowing for parts with superior characteristics to cast and forged parts, creation of complex-shaped parts, and less material waste.^{35,94}

The first metal AM machines were built in the 1980s, and the PBF (Powder Bed Fusion) method was soon after developed.⁹⁵ Laser PBF (LPBF, also called Selective Laser

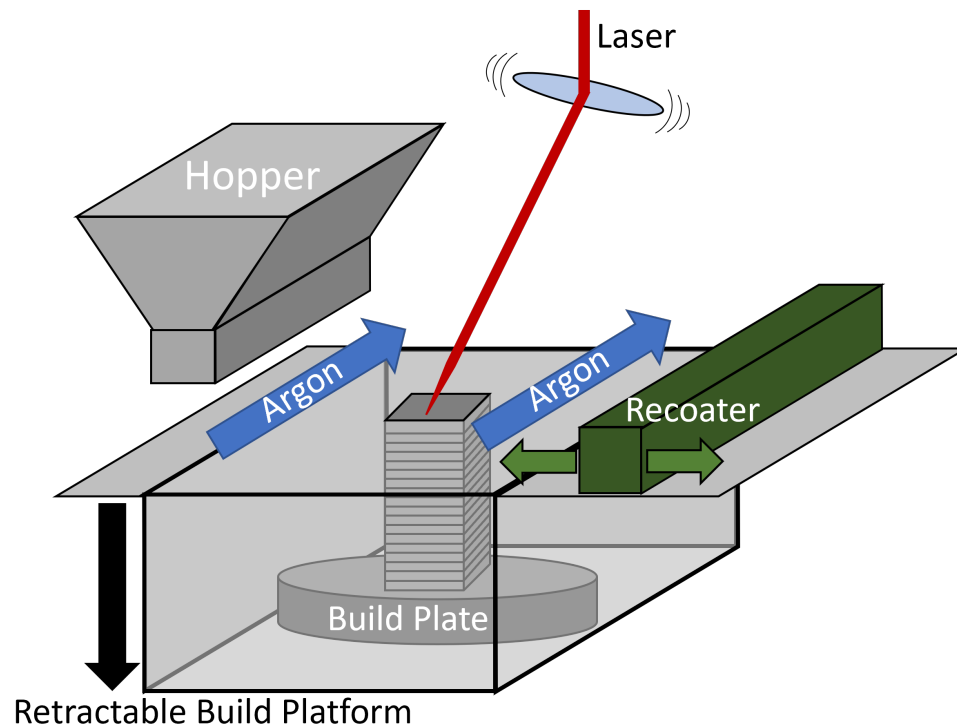


Figure 2.1. Schematic showing the powder bed fusion additive manufacturing process. Powder, stored in the hopper, is spread over the retractable build plate, a laser melts the powder in a specific pattern, the powder bed is lowered, and the process repeats.

Melting –SLM) AM systems are one of the more predominant techniques for fabricating AM metal parts.^{35,36} In general, LPBF AM involves a feedstock powder that gets spread over a retractable build plate; the laser shines on the powder bed in a specific pattern, predetermined by the input drawing, and melts the metal powder; then the build plate lowers a small amount, more powder is spread over it, and the process repeats.^{35,96} A general layout of a LPBF AM setup is shown in Figure 2.1.

AM components are susceptible to numerous defects which must be accounted for during the processing and post-processing stages. Due to their thermal history–cyclic melting, solidification and directional heat extraction–it is understood that anisotropy

and defects are introduced in the microstructure of AM parts, which are then translated to anisotropic mechanical properties, often related to the build direction.^{35,41} Some of the other inherent defects that must be overcome in AM include lack of fusion, porosity, complex residual stresses, cracking, and high surface roughness.^{35,68,95,97} Keyholing defects can form under AM conditions of overly high laser power and low scan speeds, while lack of fusion defects form when too high scan speeds are coupled with low laser power.^{98–101}

It is important to consider the AM parameters' impact on these defects. A common practice when investigating different parameters in the AM process is to build and measure some sort of multi-feature block.^{17,40,102–106} A modified version of Gao blocks is used in this study. The Gao blocks are roughly 1 cm³ parameter build blocks with slanted bottom sides, a rounded surface, and notches, all of which are designed to be measured and correlate to the AM conditions. Gao and colleagues intended their Gao block to serve as a quick evaluation tool that would readily show differences in the manufacturing processes used.¹⁰⁷ A diagram showing different views of the modified Gao block shape and features is in Figure 2.2.

2.3.1 AM for High-Temperature Materials

A wide variety of studies have successfully utilized additive manufacturing Ni-based superalloys, especially Inconel 718^{35,36,104} and Inconel 625,^{36,104} along with others,^{51,97} and they all essentially agree that complex heat treatments are necessary to incite the precipitation of gamma prime phases of appropriate size and volume percentage. Ni-based superalloys with high γ' fraction are termed as non-weldable, as they are subject to strain-induced cracking and require complex thermomechanical processing to get a desired microstructure.^{43,44,51,61,97,108,109} The formation of parts with high residual

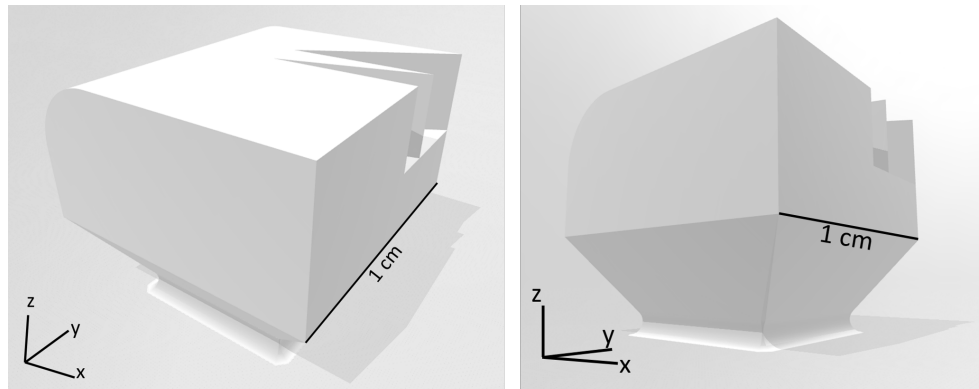


Figure 2.2. 3D render of the multi-feature block used in this study, similar to the Gao block. Two views of the same block CAD model are shown to reveal all features.

stresses, which require complicated thermal processing to reduce, is a common component of the AM process, which makes it difficult to AM Ni-base superalloys.⁵¹ These leads to the desire to decrease the process design complexity to study ODS processing without the γ' kinetics by starting with a single-phase base alloy.

A number of studies have evaluated single-phase base alloys like MPEAs built by AM.^{69,94,102,110–113} Wang et al., showed that a gas-atomized HEA powder was successfully built via electron-beam AM into a 99.4% dense sample.¹⁰² A handful of studies have produced HEAs via SLM and shown that these materials have superior mechanical properties compared to cast HEAs, likely attributed to the small grain size achieved through the high cooling rates of the SLM process.^{26,110} Brif and colleagues evaluated the mechanical properties of SLM AM FeCoCrNi, and, like many others,^{26,94,102,110–112} believed that the engineering benefits of HEA materials far outweighed the inherent complexity of manufacturing them and they concluded overall that MPEAs produced by AM were shown to have increased yield strength compared to MPEAs made by traditional melting

and casting methods, credited to the fine grain microstructure achievable through the fast cooling rates in PBF.⁶⁹

The conventional materials for high-temperature applications have historically been nickel-base superalloys, but MPEAs are a less complex material alternative. Oxide dispersion strengthening can further increase the temperature capabilities of a material, too. Producing ODS by conventional PM techniques, however, has proven difficult and costly. The conventional mixing process of mechanical alloying present a problem due to it altering the original shape of the powders. Acoustic resonance mixing was chosen for this project both because it does not induce mechanical deformation (like mechanically alloying does), nor does it rely on chemical reactions, and it is a novel material processing technique of interest to NASA.^{17,80} Conventional PM and ODS material consolidation technologies are also problematic, but AM provides a solution to that.

2.4 Statistics

One final piece of the puzzle is how to deal with the high number of variables that impact the design of additive manufacturing processing routes. As many as 50 to 100 different variables of influence have been identified for the LPBF AM process. As the amount of AM data and processing-microstructure-property insights are generated, the use of statistics and modeling is critical to AM technologies being fully integrated into the production.^{51,95,114,115} Statistical evaluations allow for data validation, and development of consistent data models and repositories based on pedigreed, validated data and databases makes it possible for future studies to utilize the data and findings from past studies.

One resource for details of statistical and modeling study setup is the Engineering Statistics Handbook put out by the National Institute of Standards and Technology (NIST). The NIST e-handbook outlines statistical methods for designing an experiment, which can be used to determine the experimental flow.⁴⁸ The handbook discusses different generic categories for experimental design, including comparative, screening, response surface, and regression modeling designs. Comparative experiments are designed to investigate the effect of changing one primary variable, without considering the influence of the other variables. Screening designs are used to identify the most important factors or effects and assess linear relationships but can suggest that curvature is present, which can then be confirmed by a response surface experiment.^{48,116} Response surface experiments are designed to find an extremum of a response of an interaction between factors.⁴⁸ This method is used to improve or optimize the settings for a process. Regression models such as full- and fractional-factorial designs involve testing all or an efficient selection of parameters in the experimental space.^{48,116}

2.5 Conclusions

The tandem development of the better-performing Ni-based superalloys to rely on complex alloying additions that now hinder both conventional powder manufacturing and the emergence of additive manufacturing to solve long-standing issues of manufacturing PM alloys with ever-increasing component geometries motivates the resurgence

of ODS alloy development to alleviate the limitations of relying on intrinsic strengthening mechanisms in simpler MPEA compositions. The major manufacturing challenge for these combined technologies (MPEA+ODS+AM) is the reliance on conventional mechanical alloying to mix the intrinsic MPEA matrix material with the ODS powders. Therefore, this work started with the hypothesis that acoustic mixing could effectively eliminate this manufacturing challenge. Very early in the program, it proved a valid hypothesis and the work translated to relying on statistical designs of experiments aimed to gain insight into the following questions:

- What are the quantitative effects of mixing parameters on the oxide coating on acoustically mixed ODS NiCoCr powder?
- What are the quantitative impacts of the AM parameters on the grain size, oxide distribution, and porosity of printed ODS NiCoCr material?
- What are the linkages between the powder and bulk processing parameters, powder properties and microstructure, and the resulting printed material properties and microstructure?

3 Acoustic Mixing of Oxide Dispersion Strengthened LPBF Feedstock

3.1 Introduction

Oxide dispersion strengthening (ODS) was a revolutionary idea that, during the 1960s-80s, was thought to be applicable to any metal alloy system in order to increase its temperature capabilities. The prevailing thought was that adding approximately half to one weight percent of an oxide (like thoria or yttria) could increase microstructural stability at temperatures above 55%-70% of the melting temperature of the pure metal alloy. Not only do the oxide dispersoids add strength by providing stable particles of appropriate size within the matrix to pin defects at temperatures higher than which other precipitates would dissolve, but these particles also enable the retention of thermomechanically introduced strengthening mechanisms.³⁰ At the time, this seemed like a panacea for solving many of the high-temperature material needs of the aerospace industry, but ODS materials were difficult and costly to manufacture with the current available technologies.

Conventionally, ODS alloys were manufactured by first mechanically alloying powder then subsequently solid-state consolidating the powder into bulk products. Mechanical alloying relies on high-energy interaction between powders to be mixed and mixing media (often stainless steel balls) to plastically deform the powders, essentially cold welding them together. The repeated welding and fracturing of the powders typically results in coarse, non-spherical powder.¹¹⁷ Apart from altering the morphology of the original powders, mechanical alloying can introduce contamination in the form of either the a mixing additive or the grinding media.^{65,66}

After producing the ODS powder, it needed to be consolidated, but consolidation of powders into complex shapes resulted in challenges in homogeneity. Like other powder metallurgy materials, ODS materials were usually consolidated by compacting and/or extruding at high temperatures.^{26,32,60,79} This resulted in a need for complex post processing and working in order to achieve the material properties of interest. These complicated processes and uneven distribution of work made it difficult to produce complex-shaped parts. Parts produced in this manner would yield too much variation in strength as compared to wrought materials, which could be simply forged into complex shapes.³⁰ Because of these pitfalls, ODS technology was largely set aside.

A way to overcome these manufacturing challenges is with additive manufacturing (AM). AM has been of interest to the industrial and research communities for the past few decades. AM combines powder metallurgy with the ability to produce complex-shaped metal components.^{36,118} More on AM and its benefits can be found in Chapter 2, but needless to say, AM is an enabling technology of much interest to the scientific community. The combination of ODS and AM technologies means that metal components with superior high-temperature capabilities can be manufactured with complex

part geometries and at a fraction of difficulty compared to when they were initially studied.³⁶

AM feedstock powder is generally spherical and has a size distribution and rheology that promote even packing behavior.^{35,49,119,120} In Laser Powder Bed Fusion (LPBF) systems, the powder needs to be able to exit the hopper and be spread evenly across the build plate. As flowability is one of the key metrics to the success of powder AM, a number of NIST¹¹⁹ and ASTM standards,^{121–123} and other research studies^{35,49,120} focus on the evaluation and qualification of powder for AM.

AM feedstock powders are traditionally prepared by a process of melting, casting, and gas atomization.^{49,85,102} This is because the alternative process of mechanical alloying can result in non-spherical, rough powder morphology, as well as material contamination from the mechanical alloying media.^{85,86} Gas atomization, however, normally results in spherical powders which are suitable for AM.⁶⁷

Composite powders for additive manufacturing, such as ODS powders, are traditionally produced by both mechanical (ball milling, regular mixing) and non-mechanical (conventional mixing and agent-assisted deposition) mixing methods.^{38,49,86} Studies investigating the characteristics of composite powders often showed a difference in powder flowability owing to powder morphology and presence or lack of satellite particles. One study which looked at the flowability and other characteristics of two powders, one with and one without nano-sized satellite particles, found that the satellite particles contributed to increased particle interlocking and thus decreased flowability compared to the powder without satellites.¹²⁴ An investigation of a composite powder (5 wt.% B₄C with Ti-6Al-4V) produced by traditional mixing and ball milling by Fereiduni et al., showed that the composite powders all had lower flowability than the original

metal powder; this was linked to increased mechanical interlocking due to the surface-attached guest powders and reduced contact surface area from increased roughness of the composite powder particles. The reduced sphericity of the ball-milled powder also contributed to decreased flowability of the composite powder.⁴⁹ It has been concluded by several studies that feedstock powder with a high density of satellite particles would compromise flowability and make non-ideal composite powder feedstock.^{49,102}

The size ratios of the individual powders comprising the composite powder are important to consider. The size difference between the host and guest/satellite powders in the Fereiduni et al. study was roughly 15:1 (15-45 μm sized host particles with 1-3 μm guest particles), and the study found decreased flowability for all of the composite powders compared to the un-mixed host powder.⁴⁹ A much higher size difference between guest and host particles has been shown to actually increase flowability of the composite powders. In a study involving the flowability characteristics of cornstarch mixed with various sizes of silica powders showed that the larger cornstarch powder when coated with the nano-sized silica powder (size ratio $\sim 750:1$), had improved flowability compared to both the cornstarch alone and the cornstarch mixed with larger silica powder (size ratio $\sim 30:1$). The authors attributed this to the decrease in cohesive forces between the cornstarch particles in the presence of nano-sized satellite particles due to the reduced surface contact.⁹¹

Size ratios among powders in a composite material can be manipulated to produce advantageous flowability. One study looked specifically at different methods of mixing nano-sized particles with micron-scale host particles as a method of increasing the flowability of the host material. Soulier and colleagues investigated a composite powder consisting of aluminum host powder and silica guest powder with a size ratio of $\sim 1000:1$

combined with a drum mixer, high and low shear mixers, and acoustic mixer. They concluded that each of the mixing methods resulted in powder with improved flowability compared to the unmixed powder, and that acoustic and high-shear mixing were both effective in breaking up silica agglomerates and resulted in a mixture that was stable during spreading.⁸⁶ The powder used in the current study is a composite of NiCoCr host powder with nano-sized yttria oxide powder (size ratio $\sim 166:1$), which is much closer to the size ratio of the powders that had improved flowability from the guest particles, and the ODS NiCoCr powder was mixed with acoustic mixing.

Acoustic mixing, which has primarily been used in the pharmaceutical and polymer industries to combine powders, utilizes ultrasonic resonance vibrations to induce complex mixing motions and quick homogenization of powder, and doesn't require the assistance of a lubricant or liquid medium.^{38,39,87} Acoustic mixing has also been utilized in making metal composites. In the study looking at acoustic mixing of silica guest and aluminum host particles, it was found that acoustic mixing resulted in a complete distribution and adhesion of the guest particles to the host particles and that the improved composite powder flowability would be viable candidate for LPBF AM.⁸⁶ Acoustic mixing was used to combine larger iron powder with smaller NiZnCu-ferrite particles to produce a uniformly mixed soft magnetic composite material with the small ($\sim 0.5 \mu\text{m}$) particles coating the larger ($>75 \mu\text{m}$) powder.⁹⁰ Another study used acoustic mixing to produce uniformly distributed and dispersed coating of bi-metal nano-sized Al-based alloy pairs to the surface of ammonium perchlorate to produce a core-shell structure.⁸⁹ Acoustic mixing has been proven to be an effective way to attain a homogeneous distribution of mixed components, something that is of crucial importance to ODS materials for achieving the full strengthening potential within the matrix.⁴⁹

Regardless of how they are combined, the high creep and yield strength of ODS materials is based on a homogeneous distribution of the nano-scale oxide.⁷⁸ The distribution of oxide is set during the powder mixing and can be modified during the additive manufacturing by localized melting. Therefore, it is essential to quantify and analyze the oxide nanoparticles at these stages.

There are a number of ways to quantify the dispersed secondary phase/particles within a metal matrix, from electron to X-ray based methods. The ability to characterize the chemistry and morphology of which depends on a number of factors including technique resolution, signal overlap, and ease. The most ubiquitous ways to assess particles is by SEM imaging and subsequent qualitative interpretation of the micrographs. Image analysis techniques can be applied to the micrographs, but this usually involves lengthy and complicated analyses.

For initial quantitative analyses, various electron based techniques such as Wavelength Dispersive Spectroscopy (WDS), Energy Dispersive Spectroscopy (EDS), and Electron Backscatter Diffraction (EBSD) can be employed. These methods require relatively minimal sample preparation, and the data are quick to collect. Because relatively high voltages—e.g. >5kV—are required to evoke the proper signal (characteristic X-ray excitation for EDS and WDS and dynamical diffraction for EBSD), the interaction volume of the electron beam with the sample will be too large—e.g. >500nm—to quantitatively identify nanoscale particles. Likewise, the ability to resolve the characteristic chemical signal overlaps dictate the chemical resolution of these techniques.¹²⁵ Transmission Electron Microscopy (TEM) is well known to provide the highest resolution analysis and can measure a sufficiently small area to capture nano-scale features, but lengthy sample

preparation is required, which does not practically allow for analysis of enough samples for statistical significance.

Other methods including X-ray Photoemission Spectroscopy (XPS) and Auger Electron Spectroscopy (AES) also collect data with a sufficiently small interaction to analyze nanoscale particles. These methods were not selected, however, due to potential peak overlap issues and sampling statistics. Photoelectron energy similarities and Auger peak energy overlaps (primarily from the transition elements: Co peaks range from 658-792 eV and Ni peaks range from 677 to 867 eV) make these techniques nonviable or at least challenging for this dissertation.^{126,127} Also, considering the detection limit of XPS and the dispersed oxides which were of interest, it was suggested that a method with higher sampling statistics was used.

The Time of Flight Secondary Ion Mass Spectrometry (TOF-SIMS) method provides the most advantages relative to the other techniques, in regards to this project's restraints. TOF-SIMS has sufficiently high resolution to analyze nano-scale surface particles, is a fairly quick analysis requiring minimal sample prep, and because the technique measures ion masses of the sample, there are no peak overlaps to contend with.¹²⁸ TOF-SIMS is a semi-quantitative method, but this is not enough of a negative to deter from its use for this project. These techniques and their pros and cons are summarized in Table 3.1.

Technique	Pro	Con
EDS, WDS, EBSD	<ul style="list-style-type: none"> •Simple sample prep •Quick analysis 	<ul style="list-style-type: none"> •Large interaction volume
SEM Micrographs + image analysis	<ul style="list-style-type: none"> •Simple sample prep •Can resolve particles 	<ul style="list-style-type: none"> •Complicated analysis
XPS, Auger	<ul style="list-style-type: none"> •Surface Sensitive 	<ul style="list-style-type: none"> •Peak overlaps •Detection limit
TEM	<ul style="list-style-type: none"> •Pinnacle of resolution 	<ul style="list-style-type: none"> •Extensive sample prep •Not viable for many samples
TOF-SIMS	<ul style="list-style-type: none"> •Surface sensitive •No peak overlaps •Quick analysis •Simple sample prep 	<ul style="list-style-type: none"> •Semi-quantitative

Table 3.1. Various techniques to quantify nanoparticles and their pros and cons for assessing the distribution of yttria nanoparticles dispersed in a NiCoCr matrix.

The objective of this study was to understand the sensitivity that acoustic mixing has to creating powder with a uniform oxide distribution. The literature on composite powder mixing indicates that acoustic mixing should be a suitable option for mixing ODS + MPEA powder with a size ratio greater than 50:1. In order to investigate this, SEM direct imaging and TOF-SIMS were selected as complementary techniques.

3.2 Experimental Methods

The analysis of the mixing parameters' effect on the oxide distribution on the powder was done in two phases. The initial phases of experiments were designed to qualitatively evaluate the impact of two powder processing inputs (mixing condition A-E and mixing time 0-4t) on the effectiveness of coating NiCoCr powder particles with yttria. The goal was to screen the variable field and down-select mixing parameters to use in the next phase of experiments. After defining the design space and qualifying the effect of the mixing parameters on the ODS powder, the next aim was to quantify the effect of the mixing parameters on the powder. This was done in the second phase of experiments, which involved semi-quantitative surface chemical analysis by Time of Flight Secondary Ion Mass Spectrometry (TOF-SIMS) to provide semi-quantitative information about the yttria dispersion in the powder and bulk materials. The objective of the experimental approach was to model the impact of mixing parameters on the distribution of oxide around metal powder both qualitatively and semi-quantitatively.

NASA's concern for intellectual property sensitivity for this project mandated the normalization of processing variables. For this dissertation, the mixing parameters (mixing time and mixing condition) are normalized. Mixing time is given in increments of t, and mixing condition is presented in sequential increases from A to E.

3.2.1 Acoustic Mixing

The metal powder (size 10-45 micron range) was an equiatomic mixture of Ni, Co, and Cr, plus slight additions of Re and B, received from Praxair Surface Technologies. The

powder size range was verified by conducting six measurements of the particle size distribution, as described in Appendix A Section 2. The oxide powder was nominally 100-200 nm sized Y_2O_3 powder from American Elements. The metal powder (NiCoCr) was combined with 1.0 weight percent of the oxide (Y_2O_3) powder, as supported by previous ODS studies^{29 19 79}, and then the two powders were mixed in a resonance mixer (Resodyn³⁷) to produce the ODS MPEA powder.

Powders were mixed in either metal (holding ~950 g of powder) or plastic (holding ~250 g of powder) containers. Resodyn claims that their resonant mixing process and equipment are all scalable, so the size of the container was of negligible importance; weight percent of oxide powder and total container fullness are more important.³⁷ Weight ratio of metal to ODS powder and container fill percentage were held constant at 99:1 and 85% respectively. Powder was weighed on a standard lab scale with resolution of 0.001 g, and all powder handling was conducted in a fume hood.

The containers of powder were mixed acoustically at NASA Glenn Research Center in a Resodyn LabRAM II mixer (flow dynamics described in Coguill et al.³⁹) Various mixing times (0.5t to 4t) and various mixing conditions (A, B, C, D, and E) were used. Figure 3.1 shows images of the powders after various mixing times. The jars were clamped into the mixing fixture and the mixing time and condition were adjusted for each batch. In order to avoid the mixing containers overheating, the samples were mixed for 1t minute increments with at least 2t minutes of cooling time in between. Early experiments using mixing conditions D and E resulted in the plastic jars losing structural integrity and bowing (as seen in Figure 3.2). All subsequent mixing experiments were conducted in metal containers.

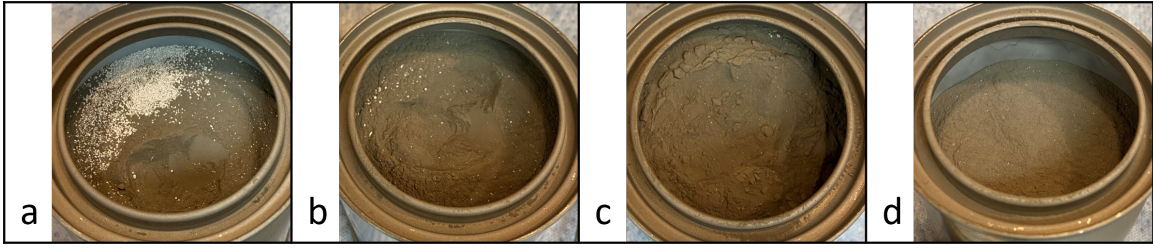


Figure 3.1. Images of the mixed powder in the mixing containers after (a) 0.5t time, (b) t time, (c) 1.5t time, and (d) 4t time. After 1.5t time, the appearance of the mixed powder does not change significantly. The NiCoCr metal powder is gray and the yttria powder is white.

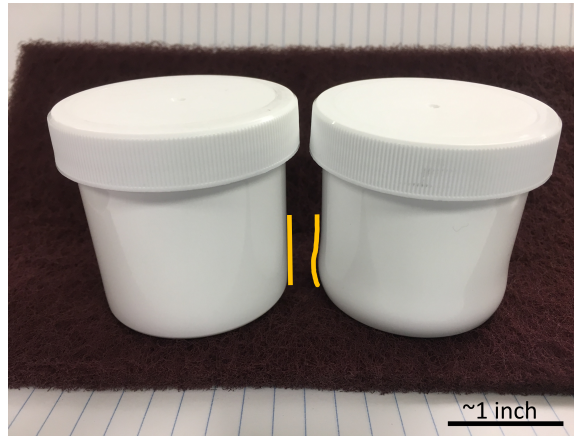


Figure 3.2. The jar on the right is bowed as a result of overheating. On the left is a new jar for comparison. The yellow lines highlight the difference.

After the successful completion of each mixing parameter set, roughly 10 grams of powder (~5 ml) was removed from each mixing container and placed into individual small glass jars for analysis. Figure 3.3 shows the mixing parameter combinations evaluated in this chapter. Opening the containers posed a risk of exposing the powder samples to ambient humidity, which was anecdotally believed to decrease the powder's flowability, but because these samples were not designated for use on the 3D printer, flowability was not of concern.

	Mixing Condition →				
	A	B	C	D	E
0.5t					X
t		X	X	X	X
1.5t				X	
2t	X		X	X	X
2.5t			X	X	
3t		X		X	X
3.5t					
4t			X	X	

Figure 3.3. This is the DOE matrix for the TOF-SIMS semi-quantitative surface chemical analysis, showing the 17 mixing parameter combinations used for powder analysis.

3.2.2 TOF-SIMS

Small amounts of each mixed powder sample were spread across carbon tape on a sample holder and evaluated. A Physical Electronics nanoTOF TRIFT V (at CWRU), using a Primary Liquid Metal Ion Gun (LMIG) with 69Ga^+ at 30 kV and 1 nA (DC) was used for analysis. Raster sizes of $400\ \mu\text{m} \times 400\ \mu\text{m}$ were used to collect the data, which meant that the data represented an average from an area that consisted of more than 150 coated powder particles. The analysis used the bunched, positive data acquisition mode, and the samples were charge compensated with both electron and ion neutralization. The

TOF-SIMS results for yttrium were then normalized by dividing the area under the yttrium peak by the integral of the whole spectrum, and then standardized by dividing the normalized counts for the yttrium peak by the normalized counts for the Co peak in that spectrum. These conversions allow for the comparison of TOF-SIMS results among multiple samples and spectra. The ratio of yttrium to cobalt for the design space explored in this study was not large enough for that normalization method to induce significant variation in the data as the amount of yttrium on the surface increased.

3.2.3 SEM and EDS

SEM samples of the loose powder were prepared by dispersing the ODS NiCoCr powder onto a carbon tape circle mounted on a standard SEM pin stub. Loose particles were removed from the stub using a can of compressed air. (This was done manually and using the Malvern Panalytical Morphologi analyzer at NASA Glenn, which is described in [Appendix A Section 3](#).) Samples for SEM imaging and EDS analysis were mounted in epoxy and polished to reveal a cross-section of powder particles. These samples were platinum-coated to make them conductive for SEM analysis.

Metallographic polishing of the mounted NiCoCr + Y₂O₃ powder samples followed the method developed in-house by the NASA Glenn Research Center metallography engineer Joy Buehler for Ni-base superalloys. The polishing routine is shown in [Table 3.2](#). The polishing routine was followed by polishing on the vibratory polisher for about 24 hours with 0.5 μm colloidal silica suspension.

Cloth	Grit (μm)	Time	Lubricant	Force (N)	Rotation Speed (rpm)
Piano	220	40 sec	water	150	300
Largo	9	10 min	pink lube	150	150
Largo	6	10 min	pink lube	150	150
Largo	3	10 min	pink lube	150	150
Nap	1	10 min	pink lube	150	150

Table 3.2. The polishing routine for mounted powder samples of Ni-base superalloys, done at NASA Glenn. This routine was followed by a vibratory polish with $0.5 \mu\text{m}$ colloidal silica suspension for 24 hours.

A TESCAN MAIA 3 (at NASA Glenn) and a ThermoFisher Apreo 2S (at CWRU) were used to image powder samples. Ten images of the whole particles (roughly 1-3 individual powder particles in each image) were collected from each sample using secondary electron imaging at 5 kV, 10-15 nA spot size, and working distance around 10 mm. At least one individual powder particle from each sample was also imaged with backscatter electrons under the same beam conditions. Five overview images were collected from each sample with a $1000 \mu\text{m}$ field of view to capture >100 particles. The polished, cross-sectioned powder samples were imaged at 15 kV, 10-15 nA spot size, and working distance of 15 mm. These beam conditions achieved good energy dispersive spectroscopy (EDS) signal, which was used to collect chemical information on the samples. Five to eight secondary electron images were collected of representative powder particles and clusters of particles. Three EDS spectral images were collected for Co, Cr, Ni, and Y.

3.3 Results

Figure 3.4 shows the results from the powder samples of the standardized and normalized yttrium (i.e. Y/Co) results plotted within the mixing parameter space. The mixing time is on the bottom axis, and the mixing condition is represented by the shape/color of the points. Figure 3.5 presents the TOF-SIMS results as a heat-map type figure overlaid on the mixing parameter matrix.

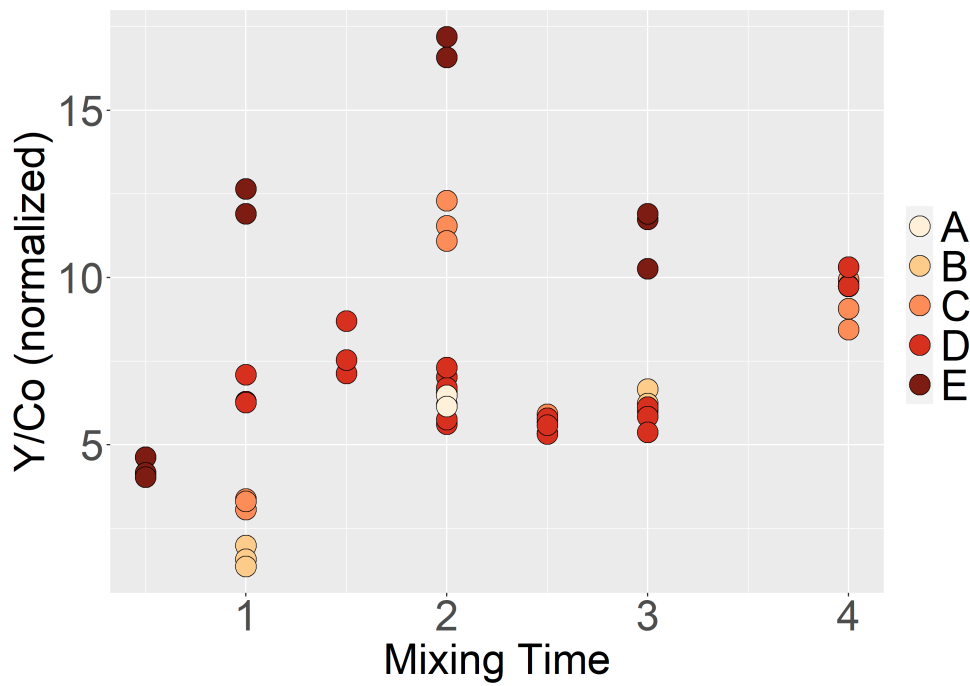


Figure 3.4. Normalized TOF-SIMS results of yttria (Y/Co), within the mixing parameter space.

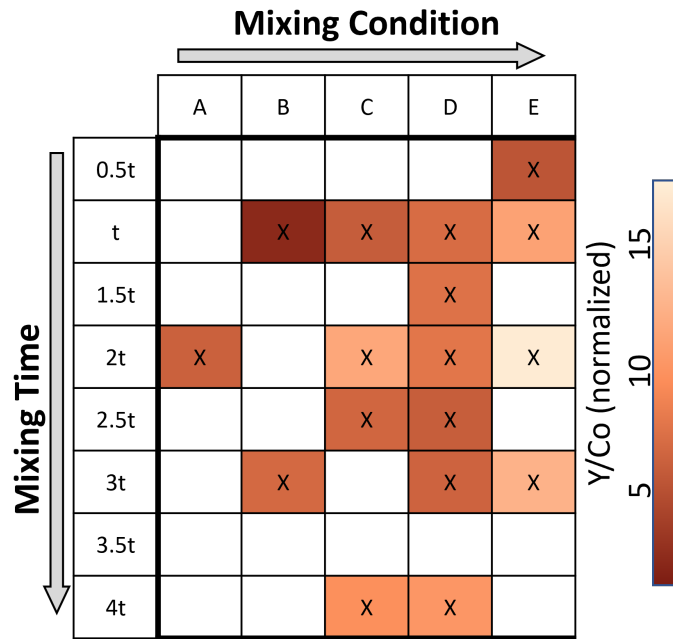


Figure 3.5. This is the TOF-SIMS results of yttria, within the mixing parameter space defined by the mixing parameter matrix, showing the 17 mixing parameter combinations used for powder analysis. The boxes are colored by a hue scale, with darkest hue representing the lowest amounts of yttrium and lightest hue representing the highest amounts of yttrium.

In order to prove that the TOF-SIMS results were valid, they were compared with SEM micrographs of various mixed powders. Figure 3.6 shows, for three representative samples, the mixing parameters, a backscatter electron (BSE) image of an individual powder particle post-mixing, a 15x15 μm area, and the TOF-SIMS results. The amount of oxide coating seen on each of the samples reflects the amount of yttrium detected by TOF-SIMS, proving that this method is accurate for analyzing the oxide coverage after the mixing process.

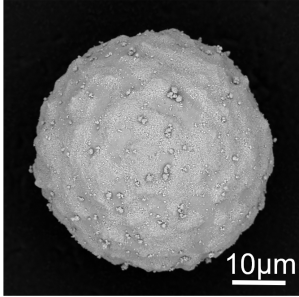
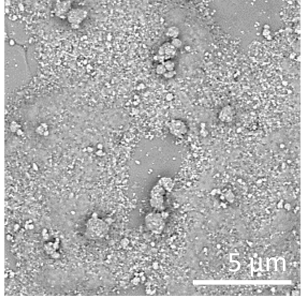
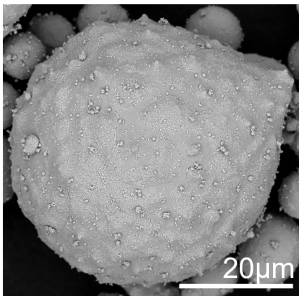
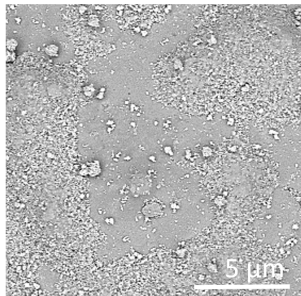
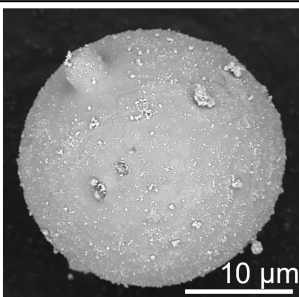
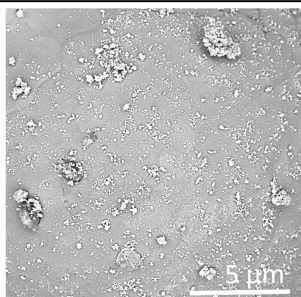
Mix Parameters	Whole Particle Image	Equal Area Image	Yttrium (Y normalized/ Co normalized)
E, 2t			16.89
D, 2t			6.48
C, t			3.25

Figure 3.6. Comparison of TOF-SIMS results from the powder samples (from Figure 3.4) and representative SEM images (BSE) from powders mixed with the same parameters. The visually obvious higher and lower amounts of oxide on the metal powder surfaces correspond to the amount of yttrium calculated via TOF-SIMS analysis.

3.4 Discussion

Prior to the TOF-SIMS analysis, an initial screening exercise to qualitatively characterize the oxide coating was conducted by visual inspection of SEM images of nine powder

samples. Figure 3.7 shows comparative images from mixed ODS NiCoCr and non-mixed NiCoCr to show the effect of the oxide powder on the surface of the metal powder. Oxide coating was evaluated on coverage (referring to the amount of surface coverage on the metal powder particles in the field of view, <25%, <50%, 50-75%, or >75%), consistency (how uniform the oxide coating was from all particles in the field of view, yes or no), and thickness (how thick the oxide coating appeared and whether it was clumpy, patchy, or dusted on the surface of the metal particles). Low mixing time and condition combine for inconsistent, clumpy coverage (Figure 3.8 a and c), while higher mixing time and condition yielded a more even oxide coating lacking clumps (Figure 3.8 b and d). The qualitative classification results, presented in Table 3.3 and illustrated in Figure 3.9, indicate that more mixing time at a higher mixing condition result in a more consistent, even, full coverage of the powder.

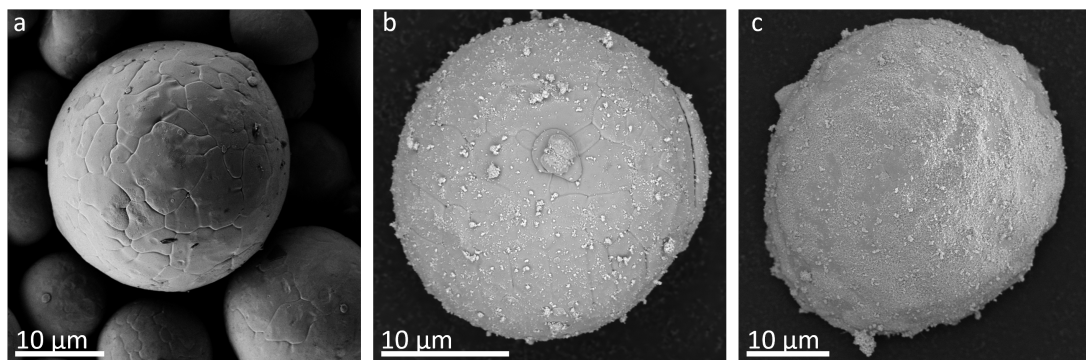


Figure 3.7. Comparison of secondary electron SEM images of uncoated (a) NiCoCr and ODS NiCoCr with a thin coating (b) and thicker coating (c) of the oxide powder, relating to no mixing, low mixing time and condition, and higher mixing time and condition, respectively. The uncoated powder image is supplied from Dr. Tim Smith.

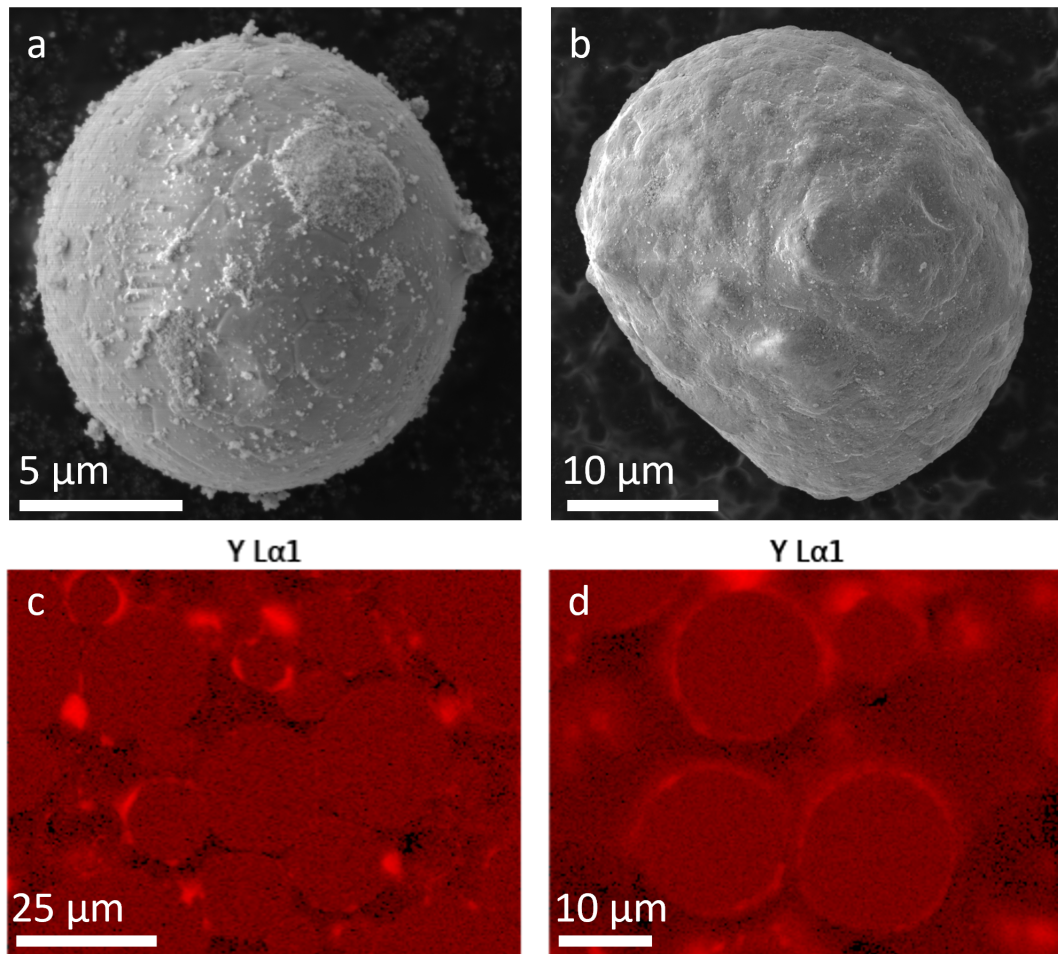


Figure 3.8. Comparison of good and poor ODS coatings. (a) shows a secondary electron image of a sample with inconsistent coverage on less than 25 percent of the surface, while (b) shows a secondary electron image of a sample with fairly consistent, greater than 75 percent coating surface coverage. (c) shows the EDS spectral image of yttrium for a sample with inconsistent coverage with many patches and clumps, and (d) show an EDS spectral image of yttrium with consistent coverage on all particles.

Mixing Time	Mixing Condition	Coverage (%)	Consistency	Thickness
1t	A	<25	not	dusting and some clumps
1t	B	>50	not	patches on most particles
1t	C	75	fairly	patches and clumps on every particle
1t	D	>50	fairly	patches and clumps on every particle
2t	A	>25	not	dusting, many patches
2t	B	50	fairly	patches on every particle
2t	C	>75	fairly	patches on every particle
4t	A	>50	not	dust and clumps on every particle
4t	B	>50	fairly	some patches and dust on most particles

Table 3.3. Classification results from qualitative analysis of SEM and EDS image data.

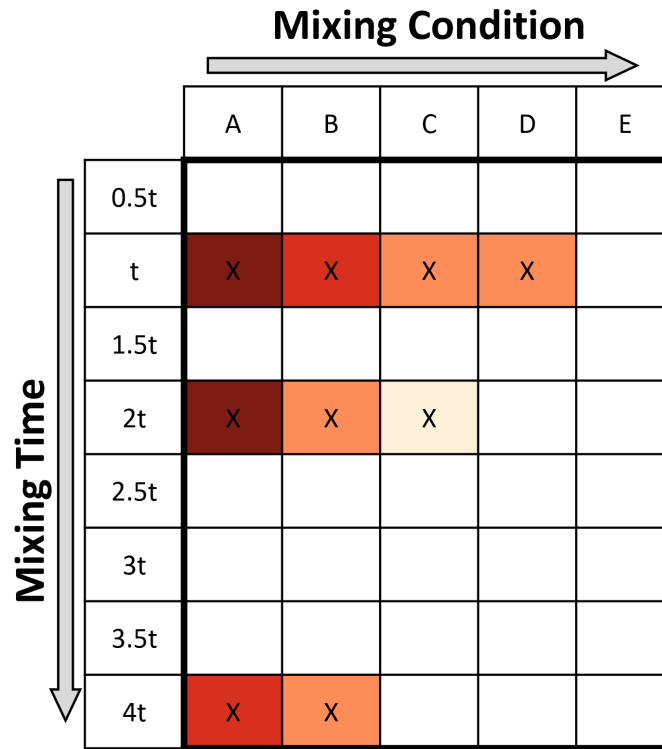


Figure 3.9. This is the DOE matrix for the qualitative analysis, showing the 9 mixing parameter combinations used for powder analysis. The darkest hue boxes represent poor mixes, the lightest hue represents the best mix, and the hues in between represent fair mixes based on the qualitative classification results.

The findings suggested a trend in mixing parameters that higher mixing time combined with higher mixing condition resulted in a better (more surface coverage, consistency, and even thickness) coating. This local maxima was not confirmed by these experiments, however. These samples were mixed in the plastic containers, which meant that the structural integrity of the containers limited the design space of the mixing experiments. Likewise, the qualitative nature of the classification model prompted a more quantitative model to more fully understand the oxide surface coating.

Not only can the ODS feedstock powder be characterized by TOF-SIMS, but TOF-SIMS results can also be used to aid in design optimization. Isolating the time component (Figure 3.4) revealed a humped trend in mixing times and which time resulted in the most yttrium. When looking across the different mixing times for each mix condition, the time "2t" was at the peak. This is most obvious for mix condition E and C. Both of these samples show an upward trend in yttrium up to 2t time and then a downward trend after 2t mixing time. It is believed that the yttrium is being built up on the surface as the mixing time increases, but after a certain point (past 2t time), the increased mixing knocks off the yttria particles. Therefore, the TOF-SIMS results indicate that 2t of mixing time results in the most yttrium on the surface of the metal powder particles. In a similar manner, if the mix condition is isolated (Figure 3.4), it can be seen that the highest mix condition (E) results in the most yttrium detected. Across the various mixing times, more yttrium was detected on samples prepared with mixing condition E. These results combine to show that TOF-SIMS results can be used in the process optimization for mixing the feedstock powder.

3.5 Conclusions

Various mixing parameter combinations were used to process ODS feedstock powder for LPBF AM. The resulting mixed powders were evaluated by TOF-SIMS and the semi-quantitative yttrium result were compared. The results and comparison with SEM micrographs of the mixed powders show that TOF-SIMS can be used to accurately assess the oxide coating on these feedstock material, and can be used for design optimization (i.e. identifying which mix parameters result in higher amounts of yttrium on the surface).

TOF-SIMS proves to be an efficient and accurate method for evaluating the surface chemistry of any composite powder. This surface-sensitive analysis technique involves simple sample preparation and relatively quick evaluation time, and can be applied to a spread of powder samples to comparatively understand the surface chemistry. Not only is TOF-SIMS a new way to characterize the pre-printed, mixed ODS NiCoCr feedstock powder, but it is an applicable method to characterize other composite powder systems, as well.

4 AM Parameters' Effect on Printed ODS NiCoCr

4.1 Introduction

Additive manufacturing has been used for the past few decades as a way to manufacture complex-shaped metal parts for a number of industries including the aerospace industry. One of the common aerospace materials that has been the focus of years of research as an AM material are nickel-base superalloys. Ni-based superalloys have been engineered to maintain noteworthy mechanical properties at temperatures around 900-1100 °C.^{18,33} They contain a variety of elements to enable γ' precipitation strengthening and oxidation and corrosion resistance, which combine to give these alloys notably stable properties up to 1000 °C, or around 60% of their melting temperature.^{18,33,51}

However, Ni-base superalloys require very precise heating and processing to form the phases necessary to precipitation strengthening in Ni-superalloys, in their volume fraction and size.³³ Precipitation hardened Ni-base superalloys are highly susceptible to cracking during processes involving complex thermal histories such as welding or additive manufacturing.^{43,44} Some Ni-base superalloys are sometimes categorized as

non-weldable due to strain-age cracking from high gamma prime fraction.^{51,109} Multi-principle Element Alloys (MPEAs), which have a much less complex chemistry, provide a good solution to many of these issues.

MPEAs have been the focus of numerous research projects over the past couple of decades. These materials have 3-5 (generally less than 10) elements that combine with high configurational entropy and solid solution phases.⁷⁰ MPEAs have been additively manufactured and have proven successful in many research studies. Almost all of the issues with additively manufacturing MPEAs relate to the AM process and not to any complex chemical interactions within the material.^{69,102,110}

Oxide dispersion strengthening (ODS) has been applied to both MPEAs and Ni-based superalloys to increase the operating temperature of the materials. In the 1960s, when ODS alloys were first becoming a major research interest, it was thought that ODS could be applied to any alloy to increase its operating temperature. One of the major drawbacks of ODS materials, which largely contributed to them falling out of research interest was that they were difficult and expensive to manufacture. Another issue identified through past attempts at creating complex parts from ODS materials was that the uneven distribution of cold work required to create the complex shapes of these parts would result in too much variation of strength.³⁰ Additive manufacturing (AM) provides a manufacturing method that overcomes these challenges and allows for ODS material to be printed into complex shapes more easily.

The AM parameters used in laser powder bed fusion (LPBF) have been known to impact the microstructure and physical properties of AM components, and many studies have investigated which parameters are most important. In one study, for example,

which looked at the influence of the LPBF parameters on steel samples, the authors concluded that the combination of laser power and scan speed had the largest impact on the microstructure of the LPBF parts compared to the other parameters investigated. They also concluded that LPBF steel samples had higher UTS and yield strength than traditionally manufactured samples.⁴¹ Another study looking at a LPBF titanium alloy investigated how the hatch spacing, layer thickness, scan speed, and laser power influenced the porosity of the sample. They determined, based on a Pareto chart, that the combination of scan speed and hatch spacing had the highest impact on the relative density (porosity) of the samples. They also found that HIP and aging could be combined to produce a fully dense part.⁴⁰ A study of the processing parameters' impact on an AM Ni-based superalloy looked at the material porosity and the microstructure of the printed parts. They used EBSD to analyze the grain structure, taking note of areas of many random crystal orientations, indicative of melting and resolidification.⁴³ Like many others^{42,45,118}, these studies determined that the combination of AM parameters, which influenced the energy density going into the part, influenced the sample porosity and number of grains.

When built with the correct balance of parameters, numerous studies have discussed that the mechanical properties of AM parts can match or exceed those of traditionally manufactured parts.^{e.g. 35,36,78} Many also discuss the importance of HIP or heat treatments to close surface pores and have fully dense parts. With that in mind, Hosseini and Popovich (2019) reviewed dozens of published AM Inconel 718 results and found that fully dense LPBF produced Inconel 718 had on average a higher room temperature yield strength than wrought, direct laser deposition, direct electron beam (wire) deposition, or electron beam melting produced samples. They also showed that AM Inconel 718 had

comparable, though slightly lower, yield strength than wrought Inconel 718 at 650 °C.⁹⁸ Information is lacking on the full mechanical properties (fatigue, crack growth, creep, etc.) of AM parts, but tension test data is one of the more commonly reported metrics.³⁶

The first objective of this study was to screen a set of samples printed with varying laser power and scan speed combinations to determine the impact of the AM parameters on the porosity of the LPBF samples. The screening experiments were also designed to explore the effect of the laser power and scan speed on the microstructure of the LPBF samples. After determining the idealized laser power and scan speed, the second objective of this study was to both understand how these processing parameters affect the oxide distribution and to compare the tensile properties of the idealized material to similar materials.

4.2 Experimental Methods

In order to achieve the first project objective—determining the impact of the AM parameters¹ on the printed microstructure—porosity and density measurements were collected on each of 36 samples, mixed with four parameter sets (representing good and bad oxide coatings, as described in Chapter 3) and nine LPBF AM parameter sets. The 36 samples were also evaluated by electron backscatter diffraction (EBSD) to gain information about their grain size distribution. The grain size and number data were modeled to reveal quantitative relationships between the laser power, scan speed, and grain metrics.

¹NASA's concern for intellectual property sensitivity for this project necessitated the normalization of processing variables. For this dissertation, the mixing parameters (mixing time and mixing condition) and additive manufacturing parameters (laser power and scan speed) are normalized. Mixing time is given in increments of t , and mixing condition is presented in sequential increases from A to E. Laser power and scan speed are represented by three normalized values each: $1p$, $1.3p$, and $1.6p$ for laser power and $1ss$, $1.2ss$, and $1.4ss$ for scan speed.

The results from both of these screening evaluations yielded idealized AM parameters that produced dense parts.

The second project objective was then achieved through analysis of samples produced with the ideal AM parameters. Tensile samples were printed and tested at room temperature and elevated temperature, and then compared to similar material yield strength and ultimate tensile strength from literature. The oxide distribution of the idealized printed samples was also analyzed by TOF-SIMS and image analysis of SEM micrographs, from which conclusions about the pre-processing (mixing) of the ODS feedstock powder were made.

4.2.1 AM Screening Procedure: Acoustic Mixing

The LPBF feedstock powder was a mixture of yttrium oxide and equiatomic NiCoCr powder. The oxide powder was 100-200 nm in size, nominally, and the metal powder was 10-45 microns in size, nominally. The two powders were combined in metal containers for mixing. Roughly 900 grams of NiCoCr (plus trace Re and B) powder was combined with roughly 9 grams of yttria powder and mixed in the Resodyn LabRAM II mixer (described in Coguill et al.³⁹) at NASA Glenn Research Center. The samples were sealed inside the metal containers and mixed for various parameter pairs of time and mixing condition, making sure that periodic mixing breaks were taken to prevent the containers and samples from overheating. The mixing parameters are summarized in Table 4.1. Additional information on the mixing process and related evaluations can be found in Chapter 3.

Two ~910g samples were generated for each mixing parameter pair. After mixing, the two containers of sample were combined into a larger metal container and rolled to homogenize for 60-90 minutes at ~100 rpm to produce the larger volume of sample required for additive manufacturing. Prior to printing, the mixed powder batches were

Mix Set	Mixing Condition	Mixing Time
Set 1	C	2t
Set 2	E	2t
Set 3	E	t
Set 4	A	2t

Table 4.1. Summary table of the mixing conditions and time parameters that define each mix set.

subjected to a number of evaluations and small samples are were set aside for imaging, as explained below. After mixing and prior to AM, any large agglomerations of yttria (similar to those seen in Figure 4.1) were sieved out with a 230 mesh screen.

4.2.2 AM Screening Procedure: Printing

Two sets of samples were printed for this dissertation: multi-feature blocks and bars. The multi-feature blocks were used for all characterization except tension testing, which was conducted on the bars (details in Section 4.2.7). The AM was done on NASA Glenn Research Facility's EOS M100 3D printer. The EOS M100 printer is a powder bed fusion style printer, using a laser as it's energy source.¹²⁹ A general schematic of the PBF-AM process is shown in Figure 2.1 and explained in the Literature Review section (section 2.3). The multi-feature block printing layout for this dissertation produced 36 blocks in a 3x3 grid of blocks with normalized print parameters detailed in Figure 4.2. The four mixing condition sets (Table 4.1) produced 4 sets of feedstock powder and were each printed following the nine same printing conditions (i.e., scan speed and laser power) to produce the 36 samples. After printing, the blocks were cut off of the build plate.

4.2.3 AM Screening Procedure: Density Measurements

Density measurements were collected using the whole multi-feature blocks and following the Archimedes' density principle. At least three measurements were collected on

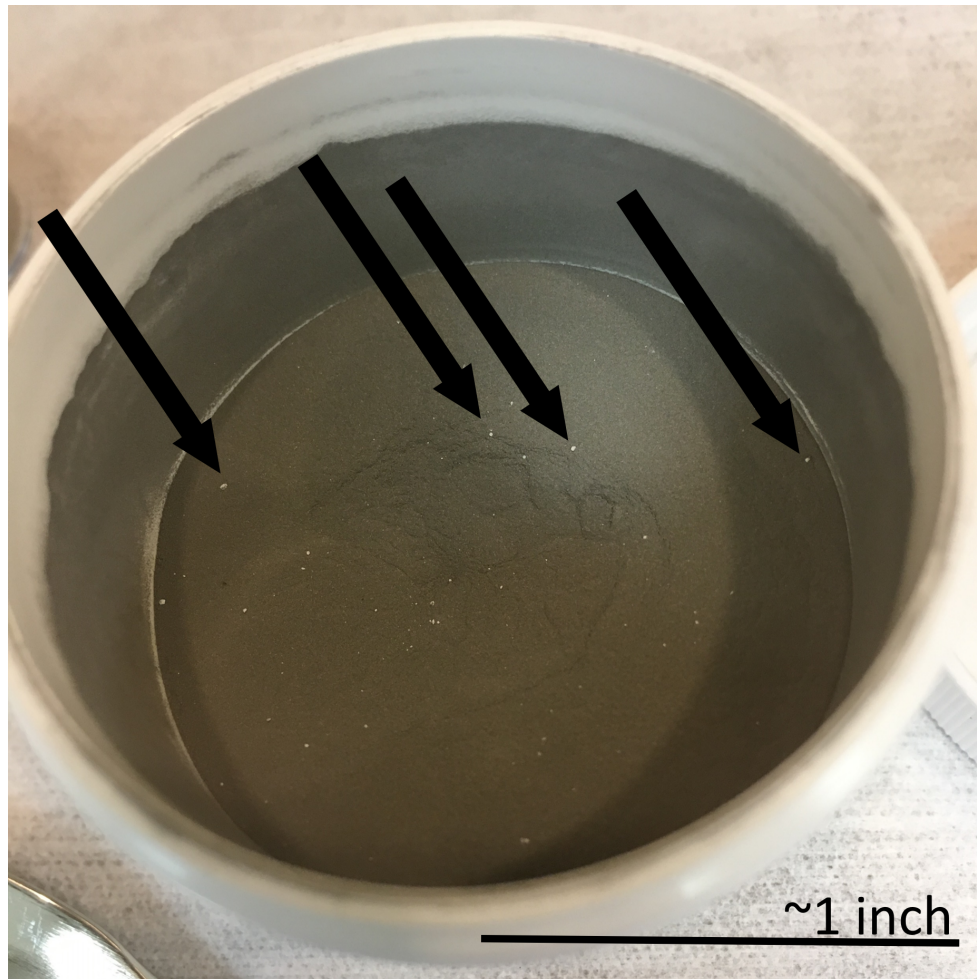


Figure 4.1. Large yttria agglomerations, several indicated by the arrows. For scale reference, the diameter of the white sample jar is nominally 2 inches.

each of the 36 multi-feature blocks (4 different mixing parameter sets of 9 blocks each, representing 3 different laser powers and 3 different scan speeds). The setup and procedure follows the diagram in Figure 4.3. The stand (G) is placed over a lab scale plate (F), without touching it (E), and the beaker (B) is placed on the stand. The wire holder (A) is hooked to the underside of the scale plate (F). The beaker is filled with enough liquid (C, water, acetone, etc.) to fully submerge the lower sample holder (D). A thermometer is also placed in the liquid to monitor its temperature. After noting the liquid temperature,

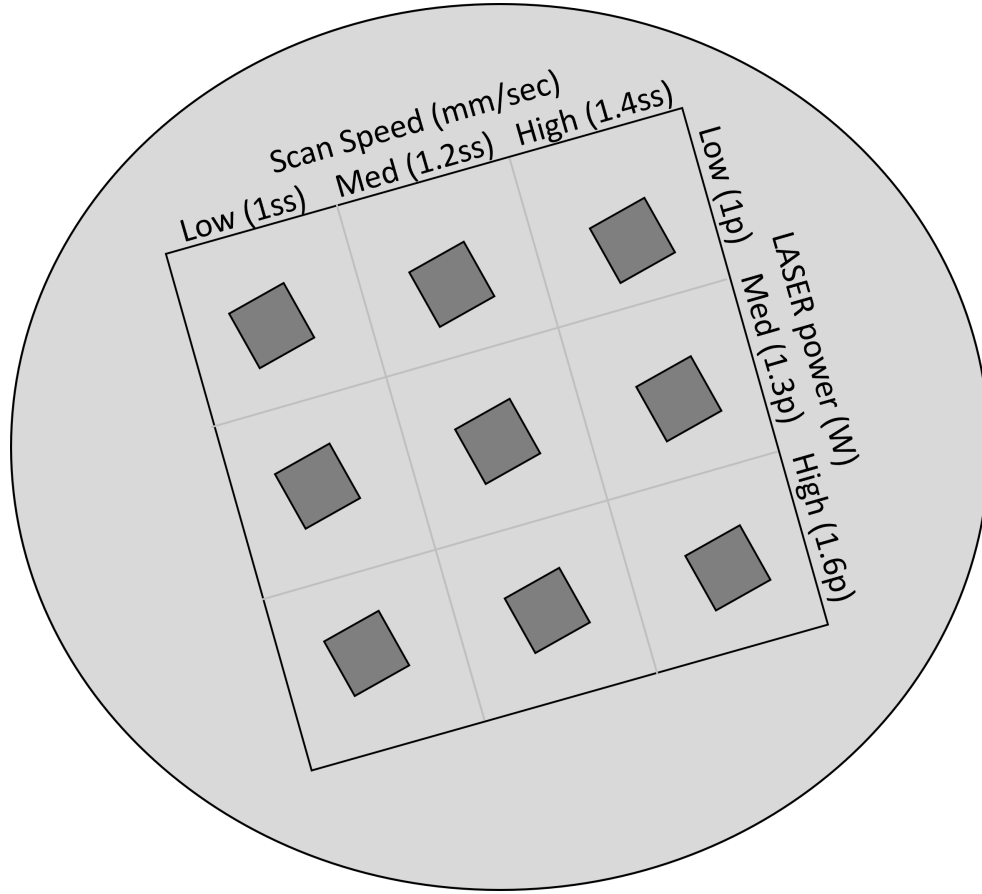


Figure 4.2. Gao block layout on the build plate with normalized print parameters along the outside.

the sample is placed on the upper sample holder (A) and its weight is measured with the scale. The sample is then placed on the submerged sample holder (D) and weighed. The sample density (ρ_{sample}) can then be calculated following the formula:

$$\rho_{sample} = \rho_{liquid} * \frac{w_{dry}}{w_{dry} - w_{wet}} \quad (4.1)$$

Where ρ_{liquid} is the density of the liquid put into the beaker, and is dependent on the liquid temperature.¹³⁰ This is multiplied by the fraction of the dry weight over (dry minus wet weight) of the sample. Initially, deionized water was used in the experiments,

but it proved to be too viscous; air bubbles stuck to the side of the blocks when submerged into the DI water. Therefore, acetone was used instead; its lower surface tension makes it an advantageous liquid for using the Archimedes method on rough samples.¹³¹ Three repetitious measurements were collected for each sample.

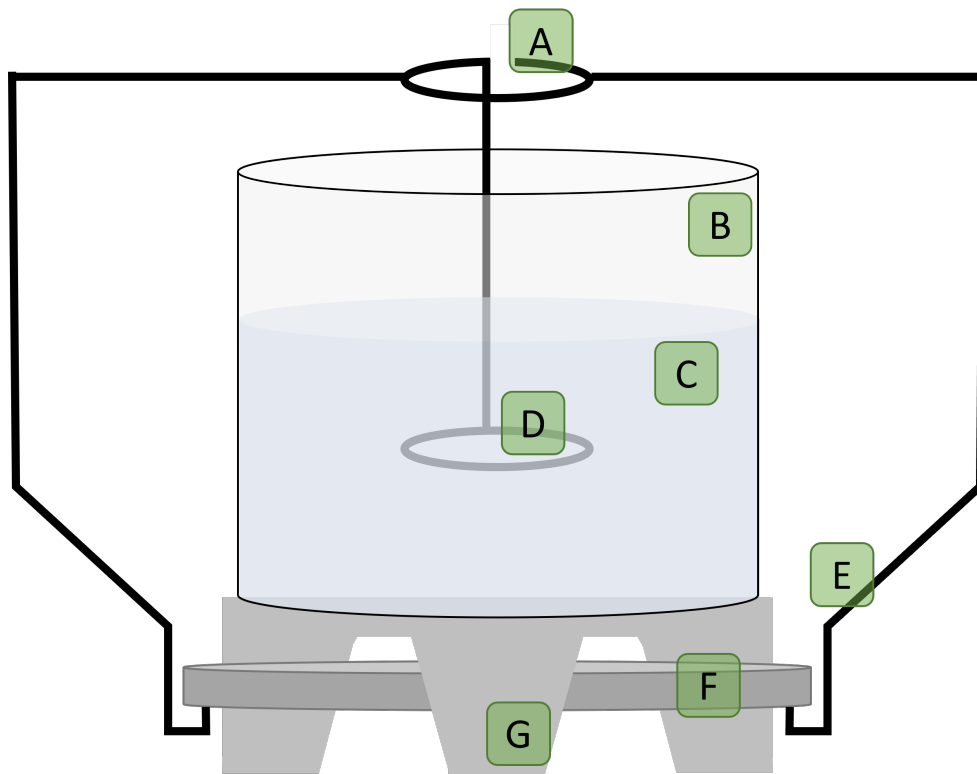


Figure 4.3. Setup for collecting Archimedes' density. The setup includes the wire sample holder (dry holder: A and submerged holder: D, with attaching points: E), beaker (B) for holding the liquid (C), laboratory scale (F), and beaker stand (G).

4.2.4 AM Screening Procedure: Porosity Measurements

Porosity measurements were collected on the 36 samples by using halved multi-feature blocks using optical imaging and image analysis. Prior to this, the samples were prepared with standard metallographic techniques.

Printed multi-feature block samples were cut in half using wire Electrical Discharge Machining (EDM, by an outside vendor Arc Drilling Inc.). One side of each sample was then polished to a mirror finish. Polishing was done with SiC grit papers ranging from 400 down to 800 grit size, followed by diamond suspensions, and a final vibratory polish using colloidal silica. The method is similar to that for powder preparation, but slightly different due to polishing media and supplies availability; Table 4.2 outlines the procedure. The polisher at Case Western Reserve University (Allied Metprep 3) was set up using platen speed of 230 rpm, sample speed of 150 rpm, contra rotation, and single force. The vibratory polishing was conducted for at CWRU 24 hours, on a Buehler VobroMet 2 vibratory polisher using colloidal silica.

Cloth / Grit (μm)	Time	Lubricant	Force (lbs)
400 grit paper	3 min	water	10
600 grit paper	10 min	water	10
800 grit paper	5 min	water	5
Nap with 6 μm diamond suspension	5 min	green lube	5
Nap with 3 μm diamond suspension	5 min	green lube	5
Nap with 1 μm diamond suspension	5 min	green lube	5

Table 4.2. The polishing routine for printed samples of Ni-base superalloys, done at CWRU

Once polished, the samples were imaged using a Keyence VHX-5000 laser confocal microscope (version 1.6.1.0, system version 1.04, at CWRU). After the initialization sequence completed and the optimum lighting conditions were selected, stitching was set up. Because the samples were flat, 2D stitching was used; the boundaries of the image collection were set up so that the entire surface was imaged at 200x.

Image analysis, using ImageJ (version 1.53e), was completed using a macro (written by David Scannapieco) that tabulated the dimensions and number of pores on the sample. The macro required a scale (determined by measuring the length of the scale bar

on the image and calculating the pixels/micron ratio) and for the area of interest to be outlined (using the polygon selection tool). Then the image was converted to an 8-bit image and auto-thresholded to result in a white background with black spots as a mask on top of any identified features on the image. The lighting conditions and fine polish on the sample meant that these features were essentially only the pores on the sample. The features were then analyzed and a table was compiled with pore count, area, major and minor axis dimensions, roundness, and other metrics. Figure 4.4 shows an example (Set 3, 1p, 1ss) before and after segmentation.

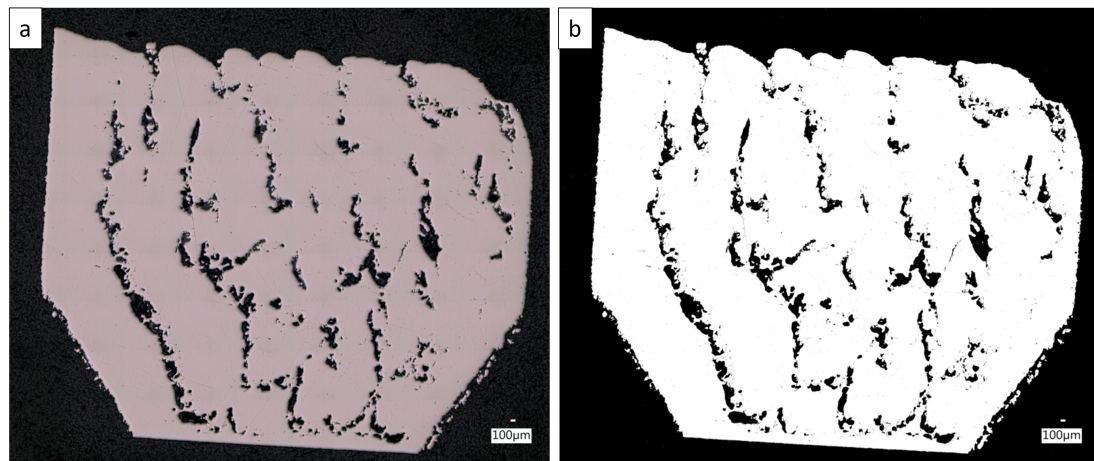


Figure 4.4. Sample from Set 3, built with 1p laser power and 1ss scan speed. The left image (a) is the stitched micrograph of the polished sample cross-section. The right image (b) is the same micrograph after segmentation.

4.2.5 Grain Size Distribution

Electron Backscatter Diffraction (EBSD) data were collected on CWRU's ThermoFisher Apreo 2S, using 20 kV and 15 nA. Polished samples were secured with carbon tape to a SEM stub, which was placed in the 45° pre-tilted stub holder position on the stage. The SEM was set into dynamic focus mode to accommodate the large tilt angle, the

working distance was set to 15mm, and the stage was rotated by 25°. Now, with the sample tilted a total of 70°, the EBSD detector was inserted. ThermoFisher's Pathfinder 2.8 software was used for these analyses. After setting up the project folder, a quick reference image was collected. The background image, required for proper calibration, was collected for roughly 3 seconds and at a low magnification. The background image was used if it did not show any diffraction bands and the pattern quality was over 60% for various locations within the image. The only crystals detected for this project were FCC (Face-centered cubic). The distance to the detector and the pattern center were then calibrated, and a new background image was collected (again for about 3 seconds) with the new camera settings. EBSD maps were collected at both 350x (~1350 μm x ~900 μm area) and 1000x (~450 μm x ~300 μm area) for each sample, with a 2.35 μm and 0.82 μm step size, respectively, and the maps were 'slightly' enhanced by the software. Grain boundaries were drawn where misorientation angles exceeded 5 degrees.

4.2.6 Models

Data for this project were collected and ingested into comma-separated variable (CSV) files via the programming language R in order to enable efficient statistical analyses and evaluation. R with Rstudio¹³² made data organization easier and allowed for comparative screening analyses aided by statistical graphics.¹³³ Exploratory data analysis⁴⁸, largely using the graphing tools within the ggplot2 library¹³⁴, were used to visualize and explore data trends. Statistical methods (from the stats package¹³⁵) such as t-tests, were used in validating some of the conclusions seen in the graphical layout of the data.

4.2.7 Idealized AM Mechanical Properties Comparison: Printing

The AM for the idealized mechanical properties comparison was done on NASA Glenn Research Facility's EOS M100 3D printer, as described in Section 4.2.2.¹²⁹ The cylindrical bar samples were nominally $\frac{1}{4}$ inch (0.635 cm) diameter and 2.5 inches (6.35 cm) long. They were printed with scan speed of 1 *ss* and laser power of 1.3 *p* and mixed with mixing condition Set 1 (Table 4.1).

4.2.8 Idealized AM Mechanical Properties Comparison: Oxide Distribution

Scanning Electron Microscopy (SEM) was used to view the oxide distribution on the printed samples. A ThermoFisher Apreo 2S (at CWRU) was used to image the oxide distribution on the printed, cross-sectioned, polished samples. The in-column backscatter detector was used with a working distance of about 10 mm, 20 or 30 kV of accelerating voltage, and 1.6 nA of current to collect at least three images at 35,000 x magnification of each sample (11.8 μm width of view). Image analysis using a neural network (from python code written by NASA Glenn engineer Josh Stuckner) was then applied to generate oxide distribution metrics. Roughly 150-300 particles were identified and measured in each image. Figure 4.5 shows, as an example, a segment of a micrograph (Set 2, 1.6 *p*, 1.2 *ss*) before and after segmentation. The dark spots in the original micrograph are the oxide particles. The mask is applied over the particles, and is shown in the segmented micrograph.

4.2.9 Idealized AM Mechanical Properties Procedure: Yttrium Distribution

One sample from each mixing parameter set, with the same AM parameters (1.6 *p* laser power and 1 *ss* scan speed) was evaluated by TOF-SIMS. Case Western Reserve University's Physical Electronics nanoTOF TRIFT V was used for analysis. The Primary Liquid

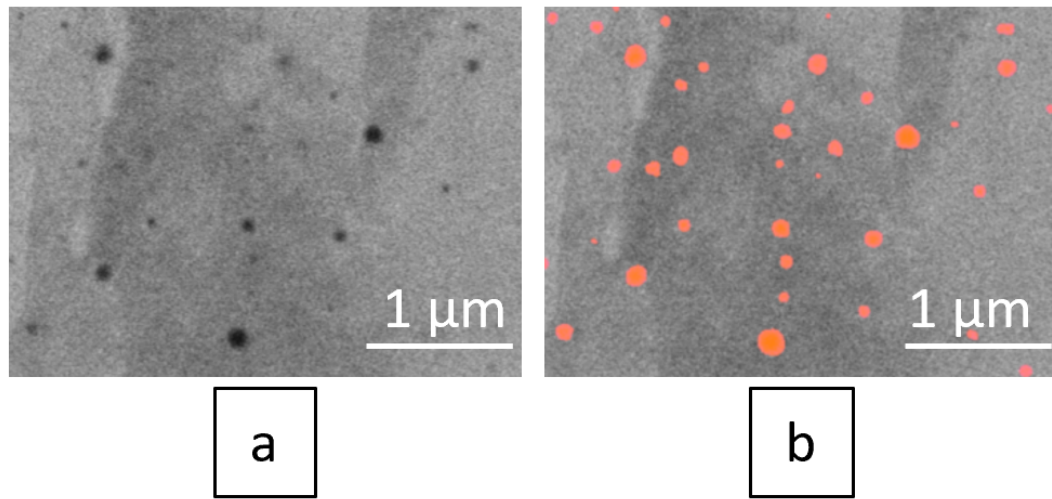


Figure 4.5. Sample from Set 2, built with 1.6*p* laser power and 1.3*ss* scan speed. The left image (a) is a segment of the SEM micrograph. The dark spots are the oxide particles. The right image (b) is the same micrograph after segmentation, with the mask applied on top of the oxide particles.

Metal Ion Gun was used in unbunched mode with 69Ga^+ at 30 kV and 1 nA (DC). Prior to collection, a 1mm by 1mm area was sputtered using the argon source at 250 nA and 3 keV for two minutes, which removed roughly 10 nm of surface material. For analysis, ion and electron neutralization were both used for charge compensation on the samples. A $50\text{ }\mu\text{m}$ by $50\text{ }\mu\text{m}$ area was rastered over in three locations per sample. The TOF-SIMS results were normalized by dividing the integral of the yttrium peak by the integral of the entire spectrum, and then standardized by dividing the normalized yttrium counts by the normalized cobalt counts.

4.2.10 Idealized AM Mechanical Properties Procedure: Tension Testing

The sample blanks for tension testing were printed as bars with laser power 1.3*p* and scan speed 1*ss* using mixing parameter Set 1 (mixing condition C, time 2*t*). The samples

were machined at Aero Prep LLC (Cincinnati, OH) into standard cylindrical style tensile samples with threaded grips and a smooth gauge section (~2.5 inch (6.35 cm) long, ~0.25 inch (0.635 cm) diameter, and ~0.75 inch (1.9 cm) gauge length, generic design shown in Figure 4.6). After machining the bar samples, four samples were sent to Met-cut for evaluation. The test matrix is shown in Table 4.3. The tension tests followed ASTM Standard E8¹ and E21² for room temperature and elevated temperature testing, respectively. Tests were conducted at 70 and 2000 degrees Fahrenheit. Calculations were made at 0.2% yield. The room temperature samples were tested at 0.5% per minute (0.0085%/sec) strain rate (through yield, then at 5% per minute strain rate to failure) and the high temperature samples were tested a strain rate of 0.049/min or 0.0008/sec (based on crosshead speed of 0.04 in/min and initial gauge length of 0.81 inches). An extensometer was used to measure elongation during the tests, but final elongation was not measured to avoid damage to the fracture surfaces. Fracture surfaces, from each half of the broken tensile samples, were imaged on a Tescan MAIA3 at 5 kV.

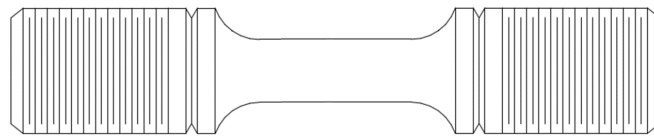


Figure 4.6. Schema of the design for ~2.5 inch (6.35 cm) long, ~0.25 inch (0.635 cm) diameter cylindrical tensile samples having $\frac{1}{4}$ – 20 threaded ends tapering down to a smooth, ~0.125 inch (0.317 cm) diameter gauge section, which satisfy ASTM Standards E8¹ and E21² for room temperature and elevated temperature tensile testing, respectively. The complete engineering drawing is shown in Appendix B Figure B.5.

Sample	RT1	RT2	ET1	ET2
Temp (°F)	70	71	2000	2000

Table 4.3. Test matrix for tension tests. Each of these samples was prepared using mixing parameter Set 1 (mixing condition C, time 2t).

4.3 Results

4.3.1 AM Screening Results: Density and Porosity

The results of the Archimedes' density measurements were plotted with error bars representing the range of one standard deviation (Figure 4.7) and show relative consistency between mixing sets but density variation most prominently between laser powers. The results from the porosity calculations were plotted in the same way (Figure 4.8), and show similar trends.

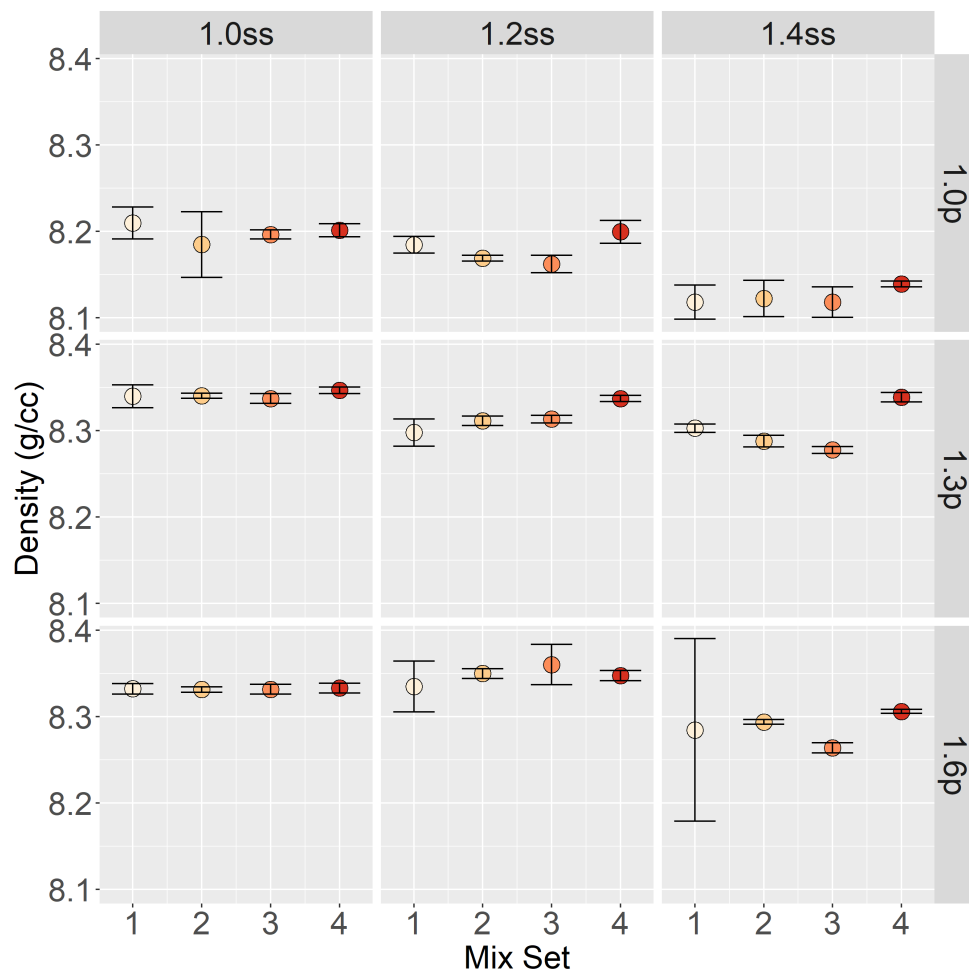


Figure 4.7. Density of samples from each mix set (color), in a grid of AM parameters. Each data point represents the average value, and error bars show one standard deviation.

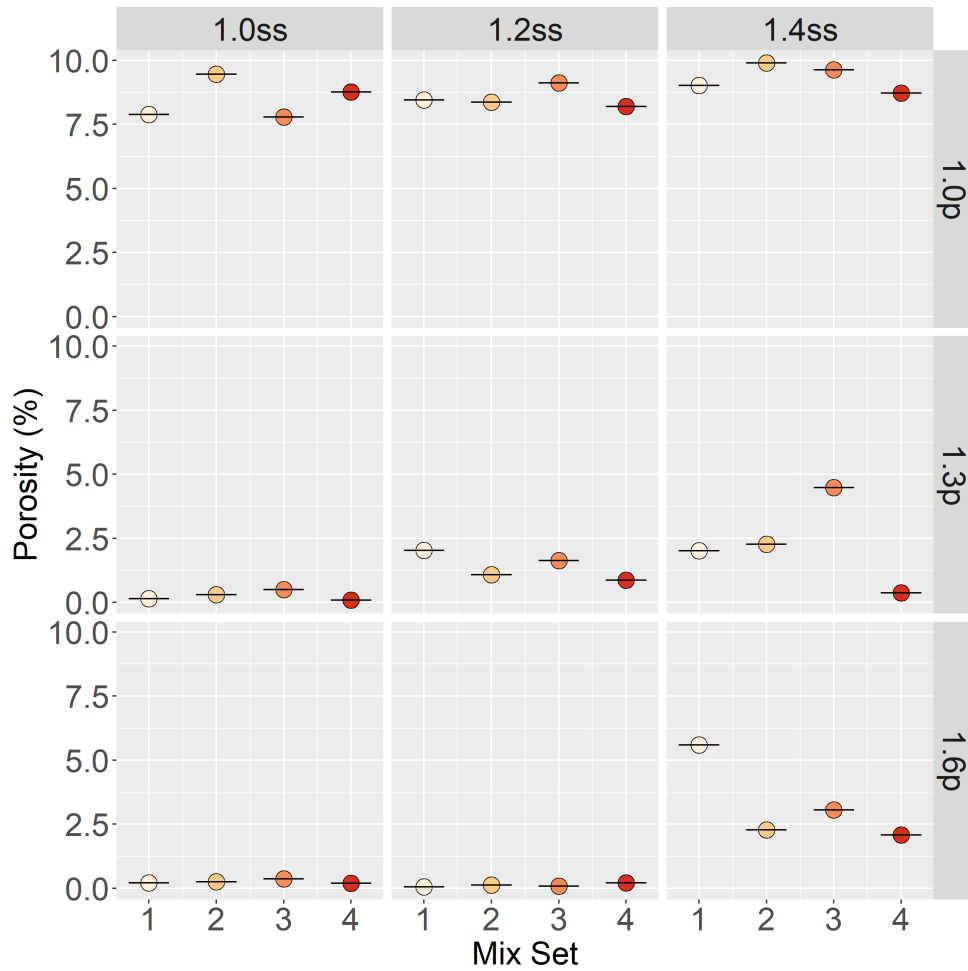


Figure 4.8. Porosity of samples from each mix set (color), in a grid of AM parameters. Each data point represents the average value, and error bars show one standard deviation.

Density and porosity are related to each other by the following equation:¹³⁶

$$\%porosity = 100 - \frac{\rho_{measured} * 100}{\rho_{theoretical}} \quad (4.2)$$

Therefore, they can be plotted against each other. Figure 4.9 shows the porosity vs density measurements with AM parameters represented by color and shape. The linear fit of the regression line (adjusted $R^2 = 0.95$) is largely attributed to having two distinct clumps of data. Not all porosity measurements represented viable AM samples, however, so

samples with porosity greater than 1% were removed, and the samples with $<1\%$ porosity are plotted in Figure 4.10. All samples in Figure 4.10 from just three laser power, scan speed combinations are entirely represented within this area: $1.3p, 1ss$; $1.6pp, 1ss$; and $1.6p, 1.2ss$. These correspond with build locations 21, 31, and 32, respectively.

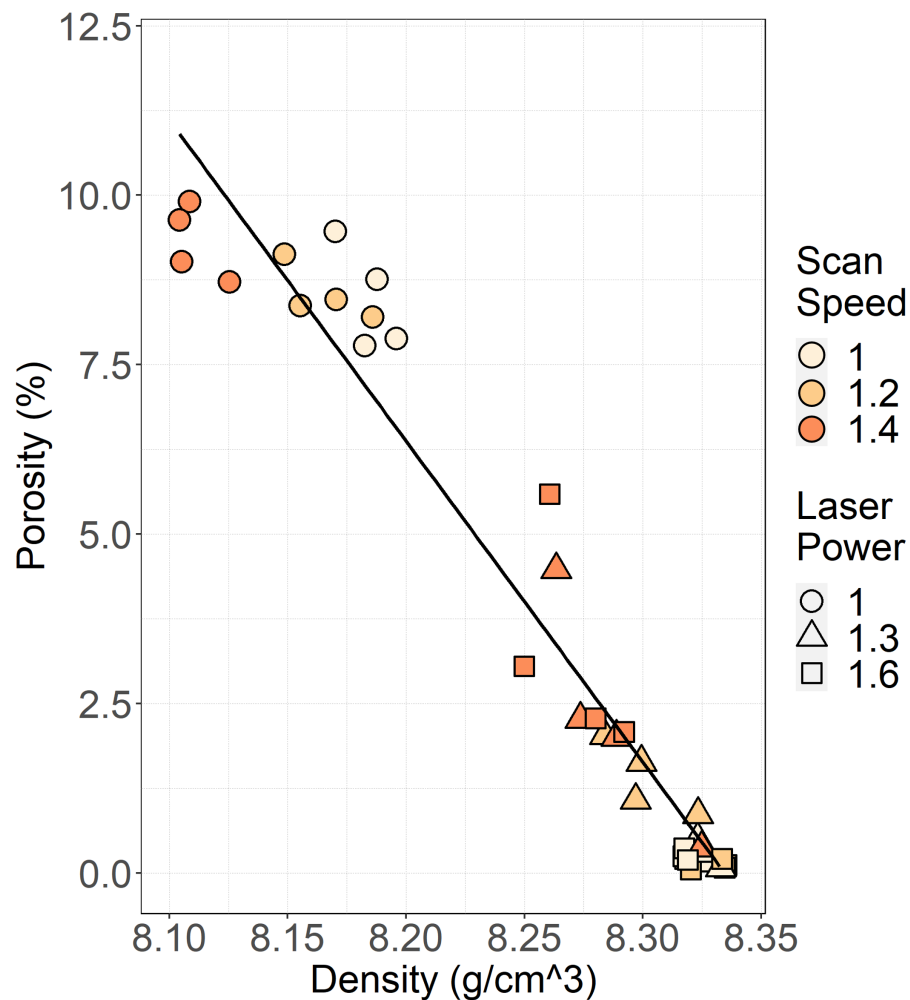


Figure 4.9. Porosity plotted against density, with normalized scan speed represented by color and normalized laser power represented by shape. The linear regression line is shown in blue.

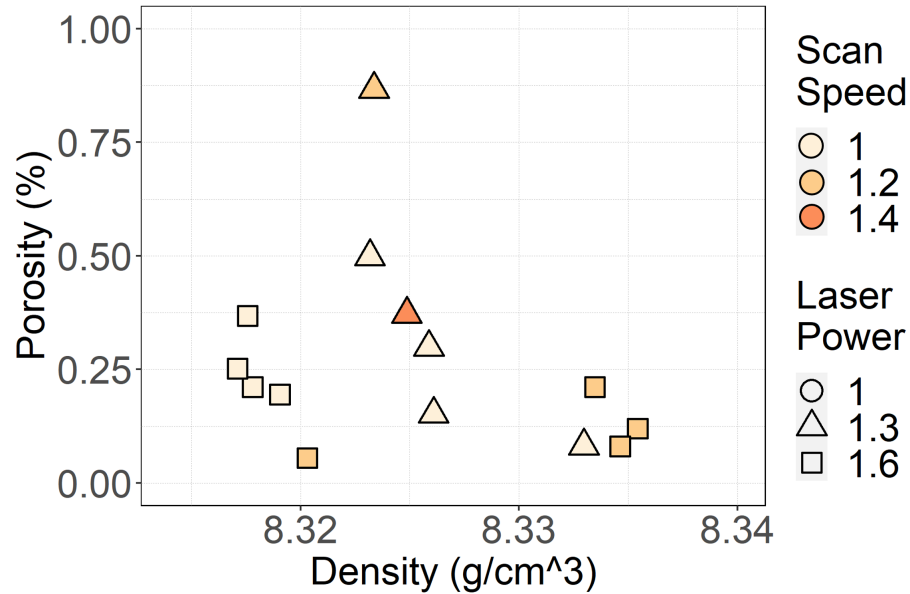


Figure 4.10. Porosity (less than 1%) plotted against density, with normalized scan speed represented by color and normalized laser power represented by shape.

4.3.2 AM Screening Results: Grain Size Distribution

The number of grains calculated from the Grain ID Maps (gathered from the 350x magnification EBSD images, which showed more grains than the higher magnification images) is shown in Figure 4.11. The grain aspect ratios are shown in Figure 4.12. Edge grains were excluded from these values. Figure 4.13 also shows a representative EBSD map with elongated grain structures in the z-direction (build direction, oriented left to right in this image). The grain aspect ratios, calculated from the same Grain ID Maps,

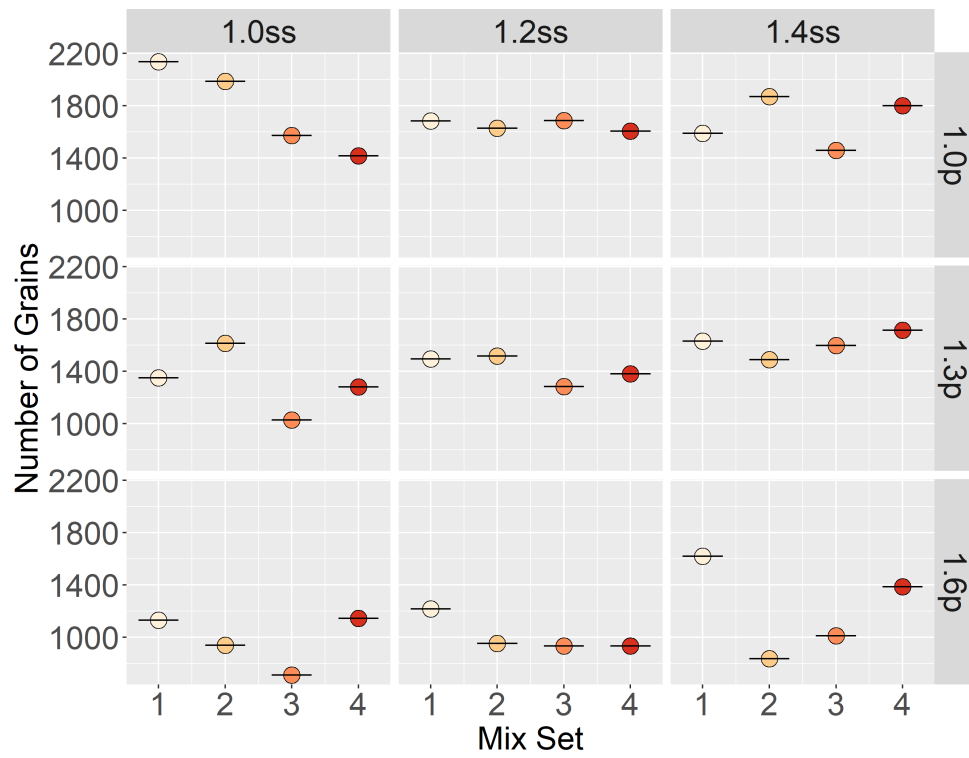


Figure 4.11. Number of grains (edge grains excluded) from EBSD Grain ID Maps, in a grid of AM parameters.

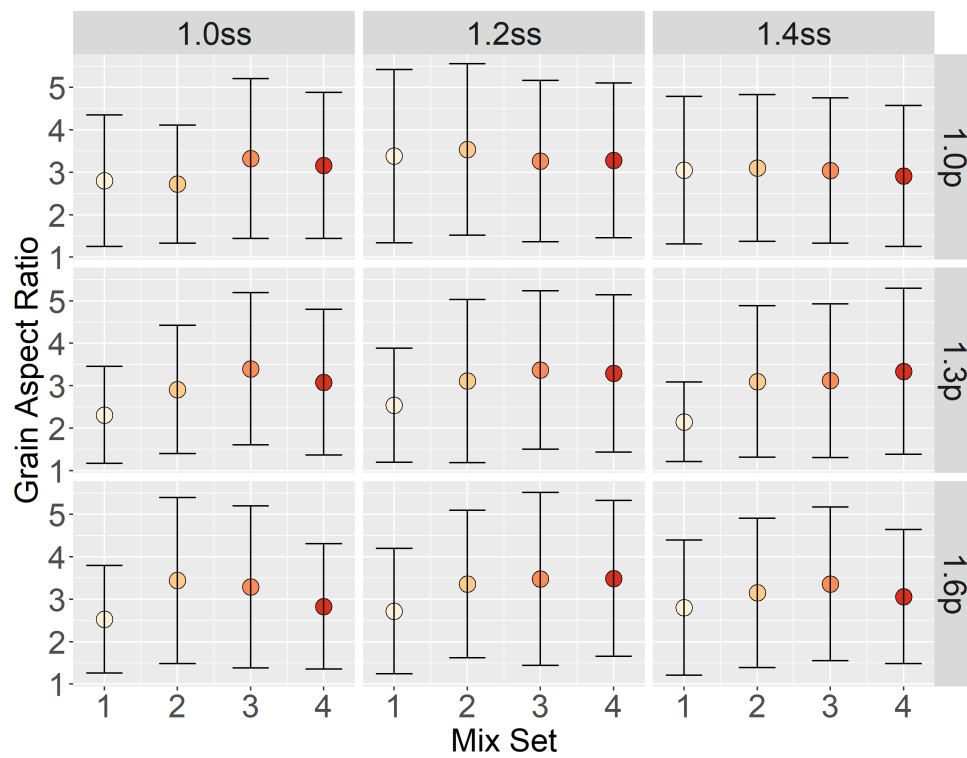


Figure 4.12. Grain aspect ratios with error bars (edge grains excluded) from EBSD Grain ID Maps, in a grid of AM parameters.

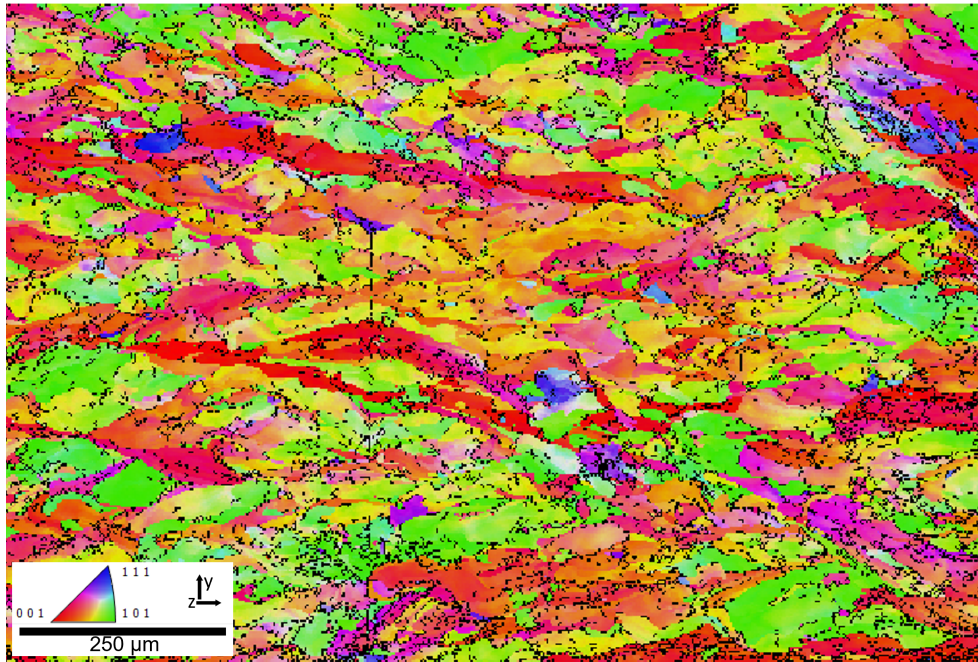


Figure 4.13. An EBSD map from a representative sample (Set 3, laser power $1.6p$, scan speed $1.4ss$ (a.k.a. build location 33)), showing the elongated grain structure parallel to the build direction (z-direction). The build direction is up-and-down relative to the 3D printer axes, and left-to-right in the orientation of the EBSD analyses.

4.3.3 Idealized AM Mechanical Properties: Microstructure and Oxide Distribution Results

The average number of yttria particles calculated from the oxide dispersion image analysis are shown in Figure 4.14. Figure 4.15 shows the number of yttria particles calculated from the oxide dispersion image analysis plotted by AM parameters (grid layout) and colored representing mix set. The number of yttria particles correlates with the precipitate area fraction and average yttria particle spacing, which were also calculated by the oxide distribution analysis, but not shown due to their similarity to the number of yttria particles data.

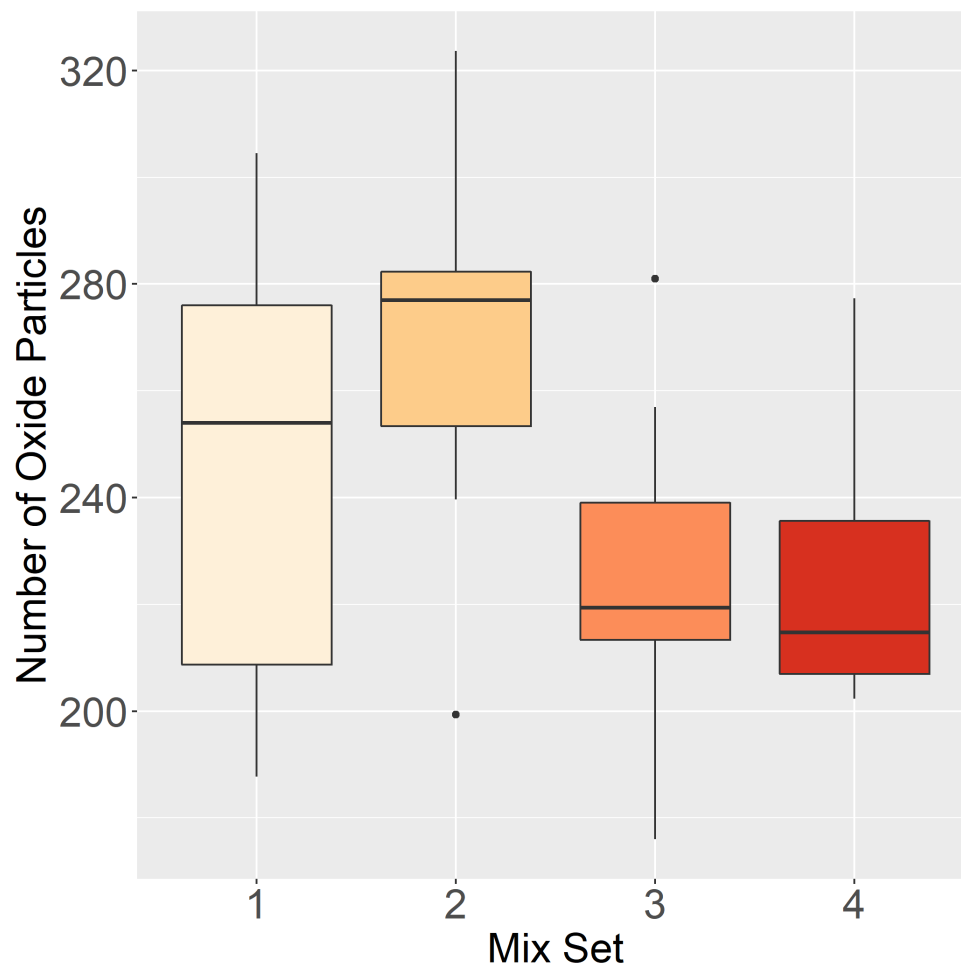


Figure 4.14. Distribution of the number of yttria particles detected from the oxide image analysis in the bulk samples from each mixing condition set, regardless of printing parameter.

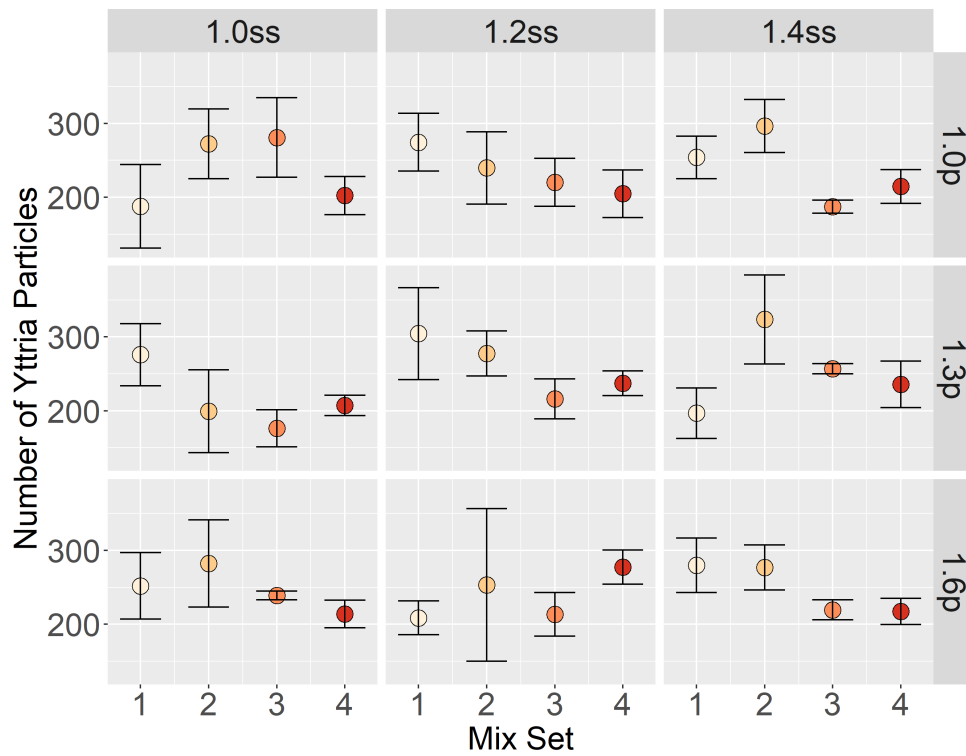


Figure 4.15. Distribution of the number of yttria particles detected from the oxide image analysis in the bulk samples from each mixing condition set, organized by printing parameters.

Figure 4.16 shows the results from the TOF-SIMS analysis of the printed samples. The height of the boxplots represent the spread of data collected for each sample and the heavy line in the middle of the boxes represents the mean value. The location of the mean line within the boxes is indicative of the data skew.

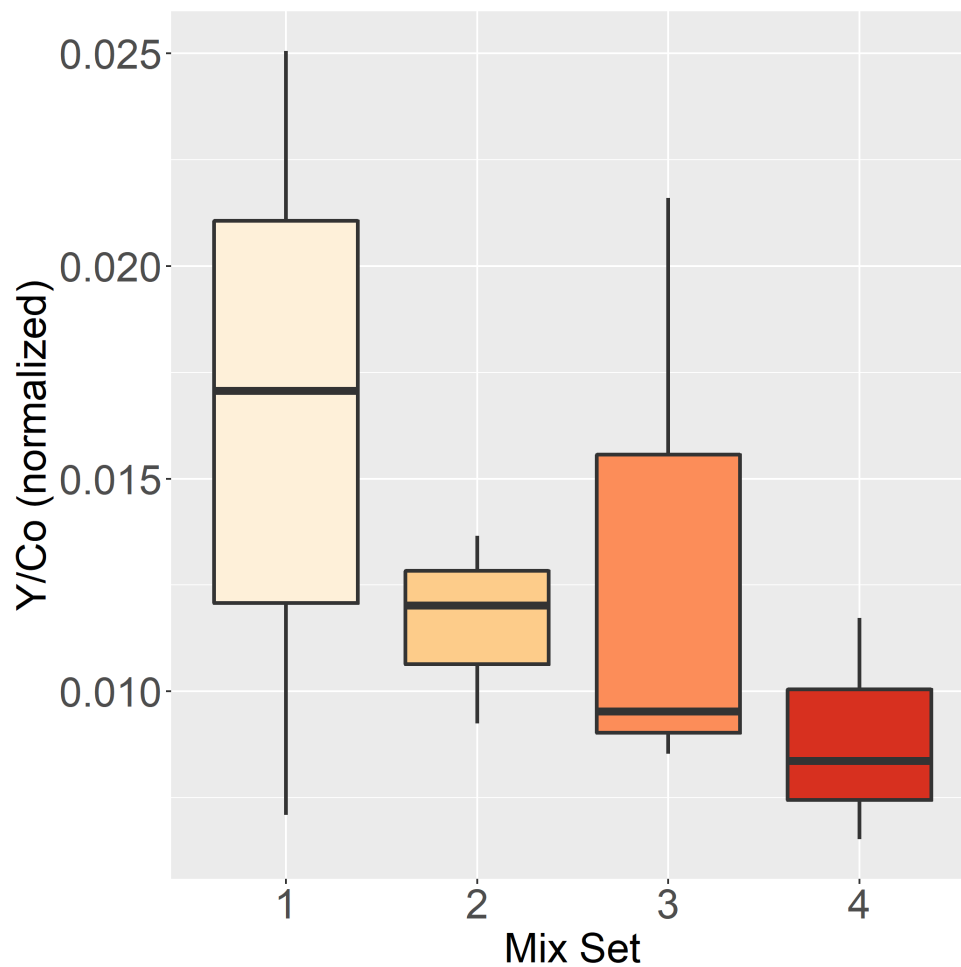


Figure 4.16. TOF-SIMS results of yttrium, from multiple locations in four printed samples.

4.3.4 Idealized AM Mechanical Properties Results: Tension Testing

The results and conditions from each of the four tension tests are shown in Table 4.4. The engineering and true stress-strain curves are shown in Appendix B Figures B.1 through B.4. The secondary electron images from each half of the broken tension samples (rotated to mirror-align the two halves) are shown in Figures 4.17 and 4.18. The room temperature fracture surfaces show the cup-and-cone structure common to ductile fracture.

The high temperature sample fracture surfaces had much less necking and show a flatter fracture surface perpendicular to the load direction. Features similarly sized to the weld pools can be seen on the surface, suggesting that "inter-weld pool" (as opposed to intergranular) fracture occurred (close-up image in Figure 4.19), which was possibly caused by lack of fusion between layers.

Sample	RT1	RT2	ET1	ET2
Temperature (°F)	70	71	2000	2000
Temperature (°C)	21.1	21.7	1093.3	1093.3
Modulus (Msi)	29.3	28.8	4.1	4.2
Modulus (GPa)	202.0	198.6	28.3	29.0
Yield Stress (ksi)	87.0	86.6	13.2	12.8
Yield Stress (MPa)	599.7	597.3	90.7	88.5
UTS (ksi)	118.1	117.5	13.5	13.3
UTS (MPa)	813.9	810.1	93.4	92.0
% Reduction in Area	65	62	12	11
True Stress at failure (ksi)	344.7	327.3	15.3	15.0
True Stress at failure (MPa)	2376.9	2257.0	105.6	103.2
True Strain at failure	1.0	1.0	0.1	0.1

Table 4.4. Tension test results in both SI and metric units. Yield stress is calculated at 0.2% of the yield. The sample names represent the two room temperature (RT1 and RT2) and 2000 °F elevated temperature (ET1 and ET2) specimens.

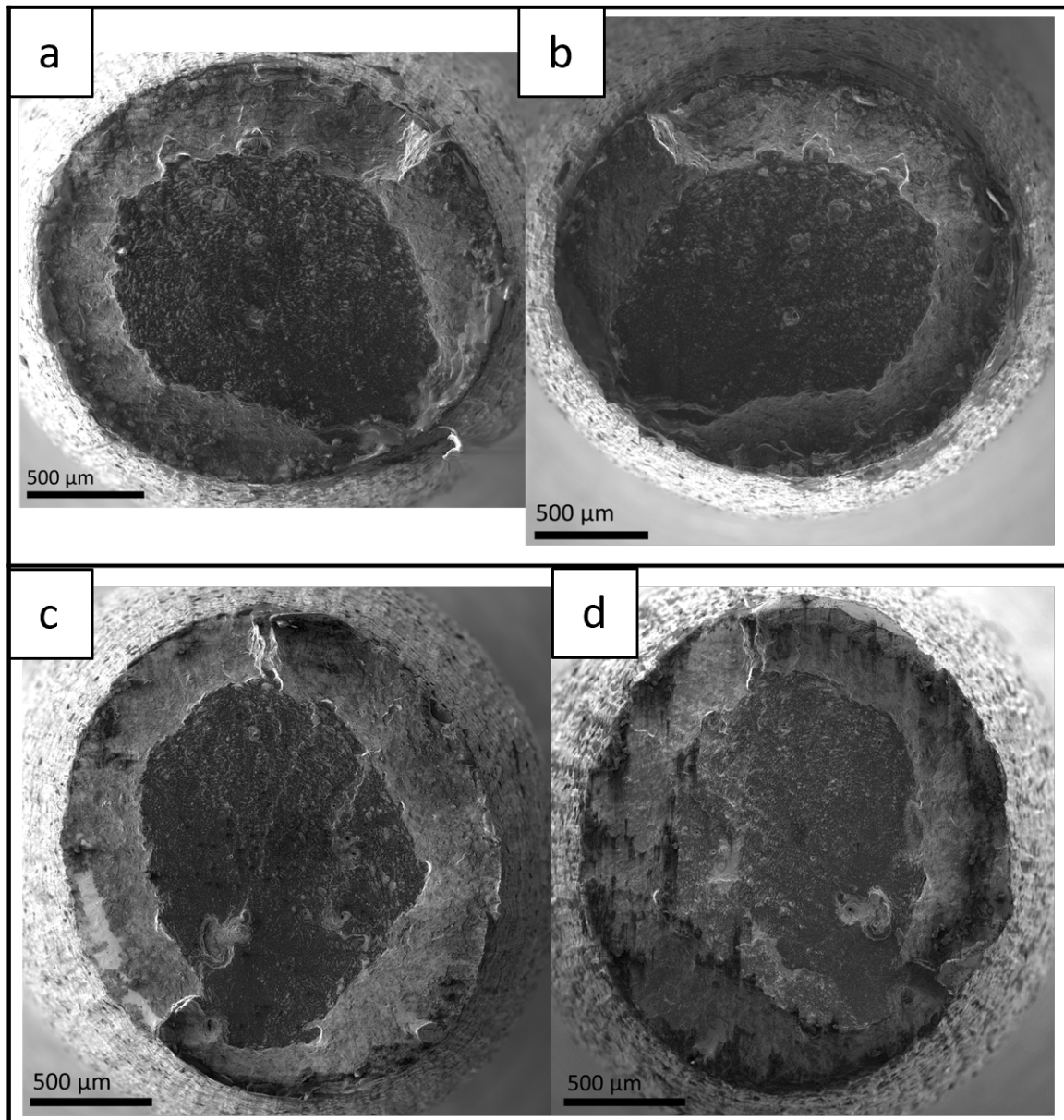


Figure 4.17. SEM secondary electron images showing both sides of the broken room temperature tensile samples. RT1 = top (a,b), RT2 = bottom (c,d). The images show the mirrored halves exhibiting the cup-and-cone structures from ductile fracture and necking represented by the smaller area of the fracture surface compared to the rest of the gauge section.

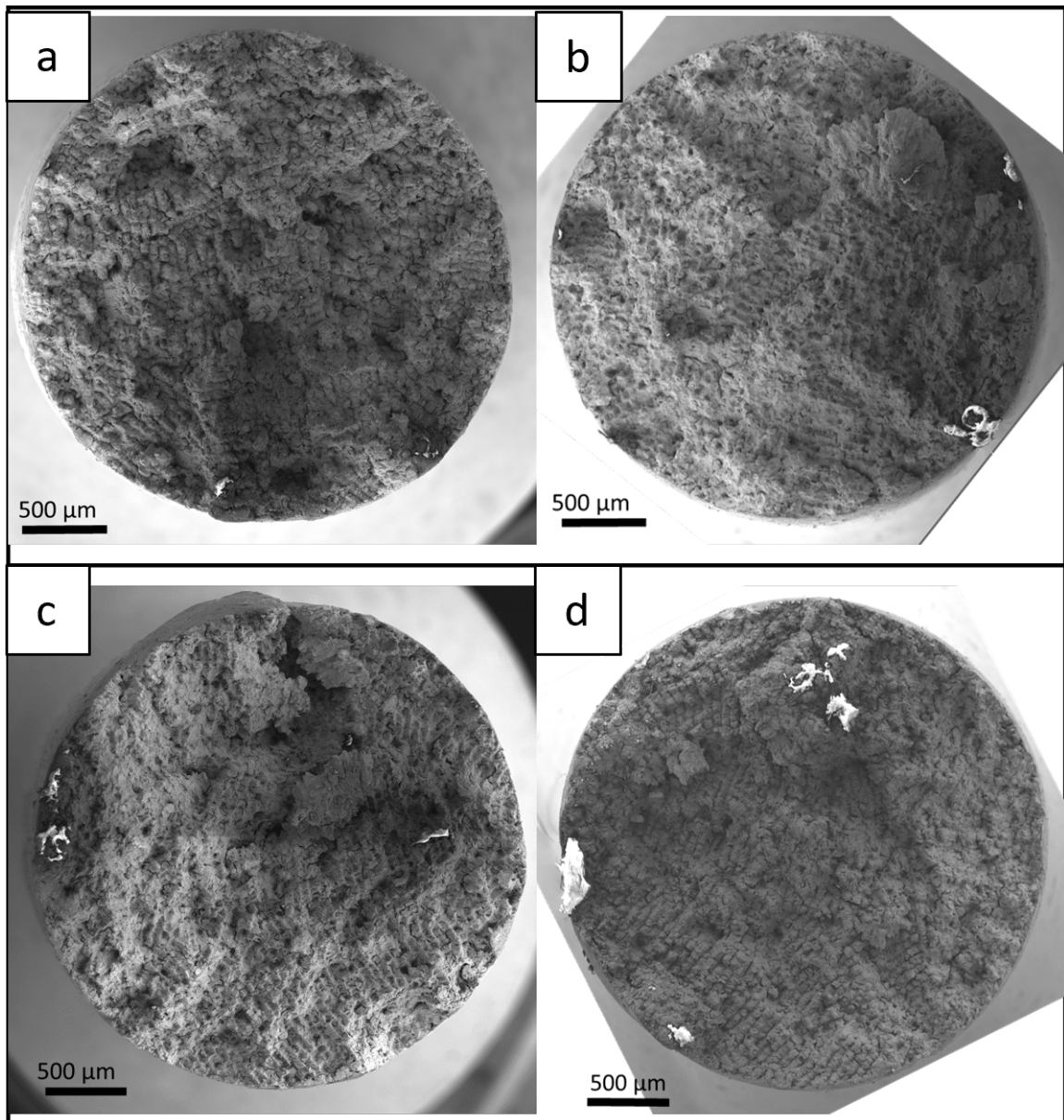


Figure 4.18. SEM secondary electron images showing both sides of the broken 2000 °F tensile samples. ET1 = top (a,b), ET2 = bottom (c,d). The flatter fracture surface and lack of significant necking is indicative of a brittle fracture.

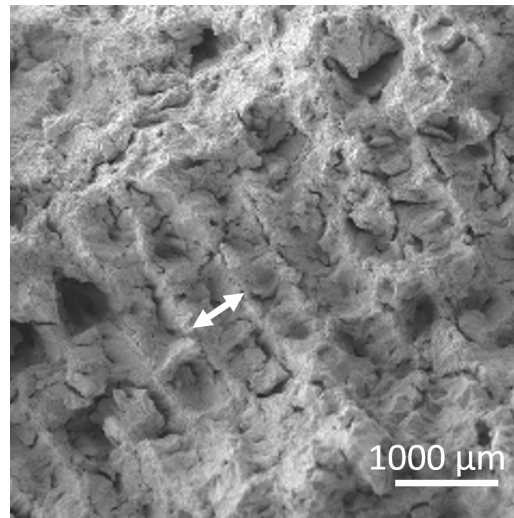


Figure 4.19. SEM secondary electron images showing a 0.5mm x 0.5mm close-up of part of ET2, a 2000 °F tensile samples. Features which are likely weld pools are visible (average width 0.055 mm), an example of which is marked with the two-headed arrow.

4.4 Discussion

4.4.1 AM Screening Discussion

Archimedes' density measurements are known to be accurate and a quicker way to attain porosity data than image based techniques prepared with metallographic methods.^{50,131,136,137} When multiple parameters are being tested (as in the case in this study, with a 3x3 grid of AM parameters), collecting Archimedes' density on all of the samples can quickly resolve which samples have the lowest porosity.

The theoretical density of NiCoCr has been reported as 8.27-8.32 g/cm³,^{138,139} and the theoretical density of Y₂O₃ is 5.03 g/cm³ (Data retrieved from the Materials Project for Y₂O₃ (mp-2652) from database version v2022.10.28). For the exact chemistry of this dissertation's material (Ni 33.1wt%, Co 34.7wt%, Cr 30.5wt%, Re 1.5wt%), the density is 8.415 g/cm³, based on element density data from the National Institute of Standards

and Technology. If we assume that the density of the ODS NiCoCr is the combination of the density of NiCoCr plus the density of Y_2O_3 multiplied by their respective volume fractions taking into account the amount of pores in the sample, then the density of the ODS NiCoCr sample (which is experimentally collected), the volume fraction of oxide (denoted as Vf_{oxide}), and the sample porosity (denoted as P) can be related:

$$\rho_{(ODSNiCoCr)} = (1 - P)[(1 - Vf_{oxide})\rho_{(NiCoCr)} + (Vf_{oxide})\rho_{(oxide)}] + P(\rho_{(air)}) \quad (4.3)$$

Equation 4.3, when using values from this study, results in calculated densities as shown in Table 4.5. The density of air used for the equation was 0.001225 g/cm^3 , according to International Standard Atmosphere. The volume fraction of oxide values are the average of the normalized yttrium (standardized with Co) amounts calculated from the TOF-SIMS analysis (Section 4.3.3). While these do not represent the actual volume fractions, these values are a relative representation. Regardless, the results show that for the lowest amount of oxide, which had the lowest measured porosity, the density (both calculated from the equation and measured) was highest. Also, sample with the highest measured porosity, which had the second highest amount of oxide, resulted in the lowest calculated density.

Mix Set	Vf(oxide)*	Porosity	Calculated Density	Measured Density
1	0.0164	0.0211	8.1828	8.3178
2	0.0116	0.0252	8.1643	8.3171
3	0.0132	0.0368	8.0620	8.3176
4	0.0089	0.0195	8.2212	8.3191

Table 4.5. Measured density values following Equation 4.3 and using the data from this study. (* the Vf(oxide) values are the average values of the normalized amounts of yttrium calculated from the TOF-SIMS results on the bulk samples.)

If we instead assume that $Vf_{oxide} = 0.0164$, based on having 1 wt% yttria, then we can rewrite equation 4.3 as:

$$\rho_{(ODSNiCoCr)} = (1 - P)[0.9836 * \rho_{(NiCoCr)} + 0.0164\rho_{(oxide)}] + P(\rho_{(air)}) \quad (4.4)$$

When the densities of the respective materials are added to equation 4.4 and plotted using the porosity values from this study, the result is shown in Figure 4.20. This confirms that the data satisfies the upper boundary of the rule of mixtures.

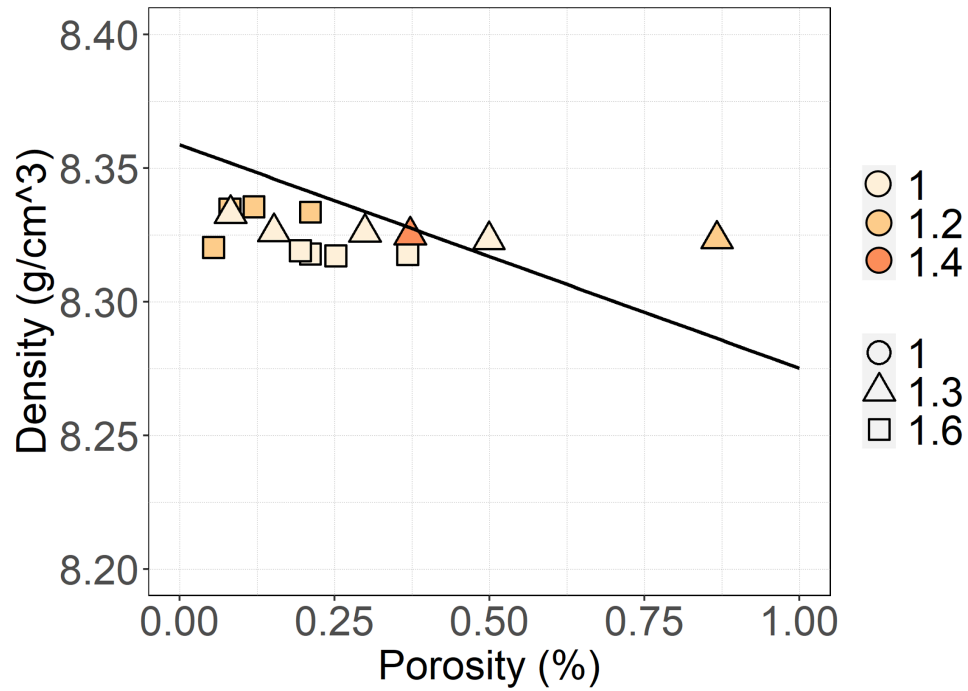


Figure 4.20. Porosity (less than 1 %) plotted against density, with normalized AM parameters represented by color and shape. Plot axes are switched from Figure 4.10 so porosity (i.e. volume fraction) is on the x-axis. The upper boundary of the rule of mixtures, calculated from equation 4.4, is shown in the plot as well.

Regardless, even if theoretical densities are not applied to convert the Archimedes' based density measurements to porosity, the density measurements are still a valid and more economical way to screen processing parameters to achieve the lowest density

samples. As a process validation method, it is not necessary to fully calculate the percentage of porosity for a material (from converting Archimedes' density to porosity with theoretical material density), simply to know which process results in the lowest porosity.

4.4.2 Porosity and AM Parameter Relationship

The relationships between the porosity and the AM parameters was also explored. Porosity was plotted against the normalized build parameters (top of Figure 4.21). It is worth mentioning that the differences in the low porosity samples do not correlate with either mixing condition or mixing time, and that the data points are plotted with slight jitter to show each point. Typical zones for lack of fusion and keyholing defects (described in the Literature Review chapter in section 2.3) are shown in relation to the build parameters,^{100,101,140} and the approximate location of the dissertation's data are indicated on that plot (bottom of Figure 4.21).

A multivariate linear model (with adjusted $R^2 = 0.71$) of the porosity against the laser power and scan speed results in the following relationship:

$$porosity = -12.615(laserpower) + 4.891(scanspeed) + 14.298 \quad (4.5)$$

(Mixing time and mixing condition were modeled along with laser power and scan speed, but the error on the correlations for the mixing parameters indicated a negligible contribution, so these were left off of the final model.) When the model is plotted on the same porosity vs build parameters plot, it can be used quantitatively to show various thresholds of porosity. This is done in Figure 4.22. The white line sits at 1.0% porosity (the intercepts are laser power = 1.42p and scan speed = 1.38ss). The space below the white line shows the build parameters (within the constraints of this design space) that

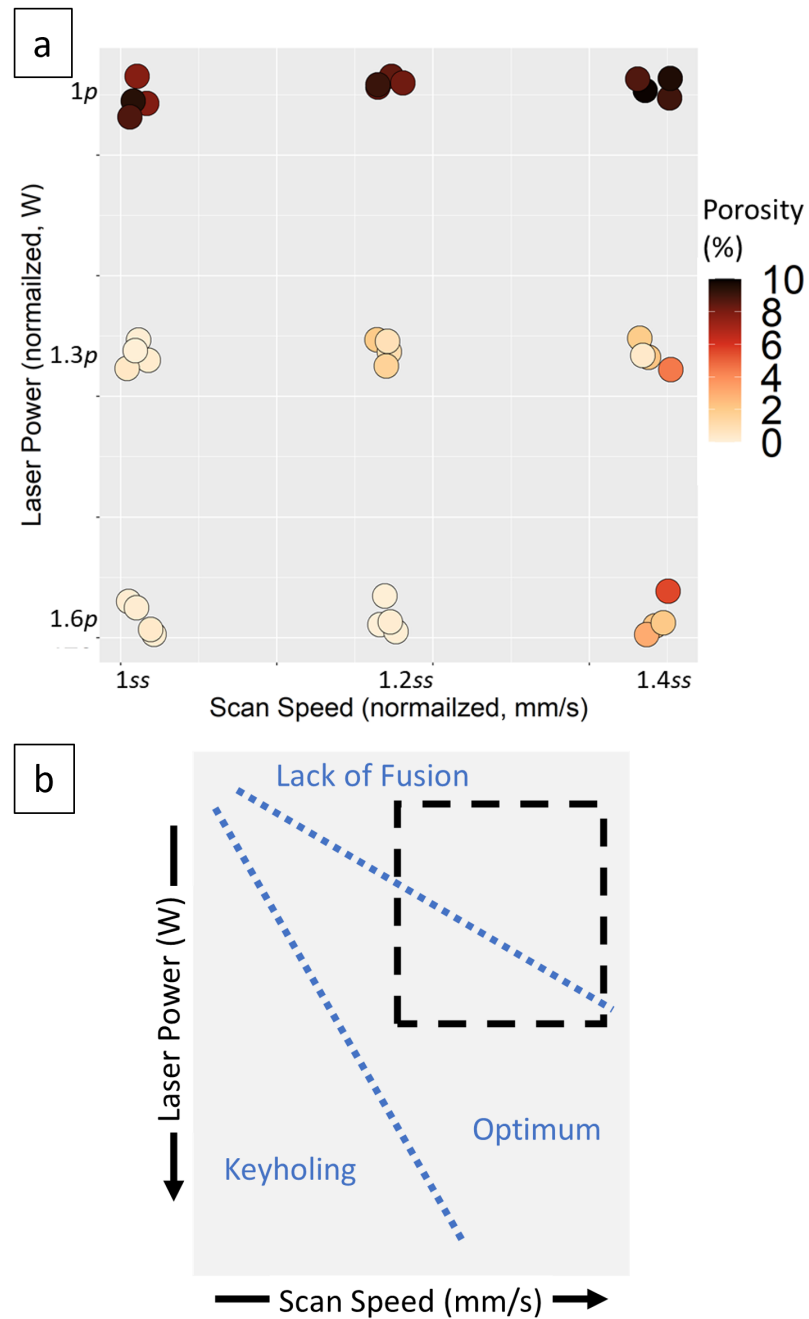


Figure 4.21. Porosity vs build parameter plot (top,a). The bottom plot (b) shows approximate zones for keyholing, lack of fusion, and optimum in relation to laser power and scan speed. The dashed black box represents the approximate location of this dissertation's data.

would result in samples with porosity less than 1%. The red-orange area represents the region on the graph with 0.05% porosity or less. The experimentally measured porosities are compared to the predicted porosity values (by the model) in Table 4.6. The residuals plot (Figure 4.23) shows that the data would be better captured with a non-linear model, but the linear model does accurately represent the lowest porosity samples in the lower left corner of the AM design space.

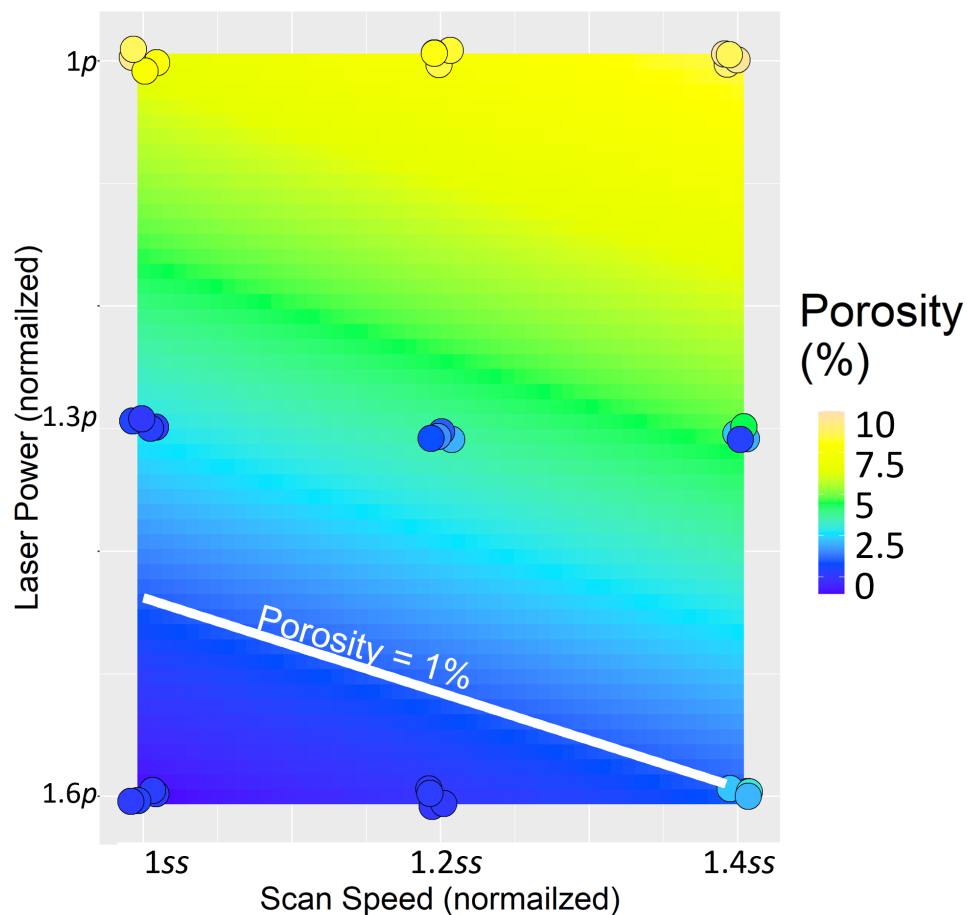


Figure 4.22. Porosity vs build parameter plot with the multivariate linear model overlaid in color. The same color scales apply to the points (measured values) and the background (predicted) for porosity. The white line represents porosity = 1%, with the space below the line representing porosity < 1.

Laser Power	Scan Speed	Porosity (%) Measured	Porosity (%) Calculated	Residual
1p	1ss	8.47 (0.8)	6.57	1.90
1p	1.2ss	8.54 (0.4)	7.55	0.99
1p	1.4ss	9.32 (0.5)	8.53	0.79
1.3p	1ss	0.26 (0.2)	2.79	-2.53
1.3p	1.2ss	1.4 (0.5)	3.77	-2.36
1.3p	1.4ss	2.28 (1.7)	4.75	-2.46
1.6p	1ss	0.26 (0.1)	-1.00	1.25
1.6p	1.2ss	0.12 (0.1)	-0.02	0.13
1.6p	1.4ss	3.25 (1.6)	0.96	2.29

Table 4.6. Table of the porosity % values experimentally measured (averaged across the four mixing conditions with standard deviation in parentheses) and porosity % values calculated from the multivariate linear model equation.

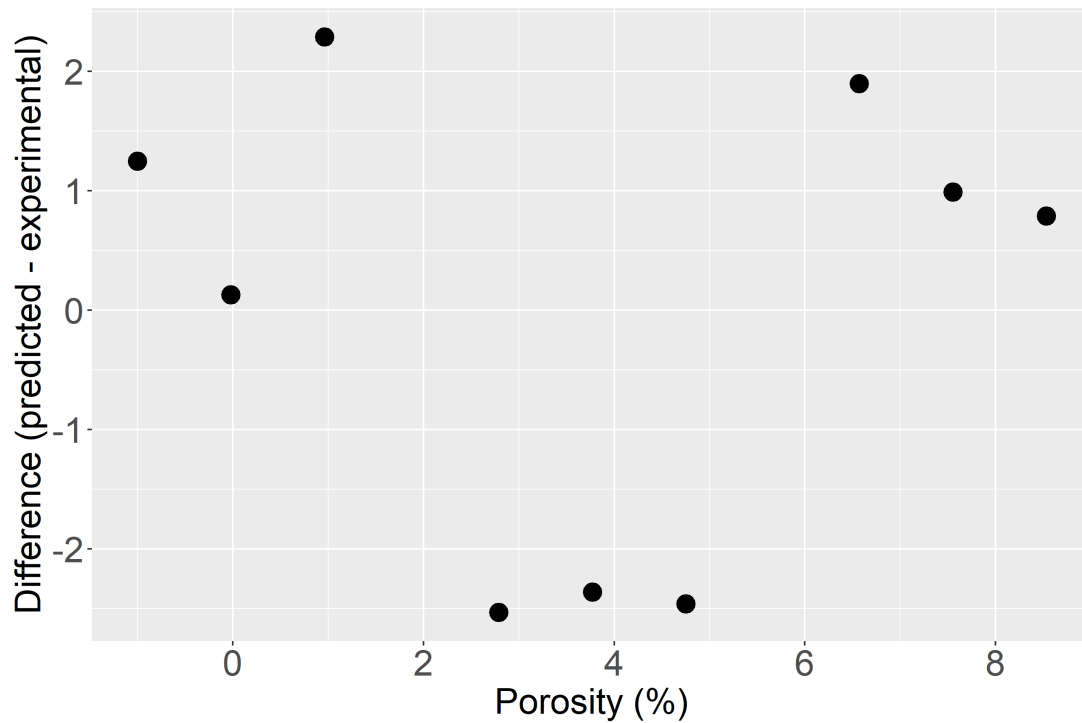


Figure 4.23. Residuals plot from the porosity vs processing parameters model. The non-random nature of the residuals indicate that a non-linear model would have fit better with the data.

4.4.3 Grain Size and Number Models

The models for grain size and number of grains also show that the grains are smaller (Figure 4.24) and more numerous (Figure 4.25) in samples built with lower laser power and higher scan speed. The equations for these models (with MC = mixing condition, MT = mixing time, LP = laser power, and SS = scan speed) are:

$$grainsize = -0.24(MC) - 2.62(MT) + 184.76(LP) - 48.00(SS) + 81.28 \quad (4.6)$$

$$numberofgrains = 0.93(MC) + 10.64(MT) - 1057.22(LP) + 351.88(SS) + 1965.40 \quad (4.7)$$

The adjusted R^2 fit of these models are 0.57 and 0.70 for grain size and number of grains, respectively. The residuals plots (Figures 4.26 and 4.27) for both models also show a random distribution, indicating that the linear models have fit the data well.

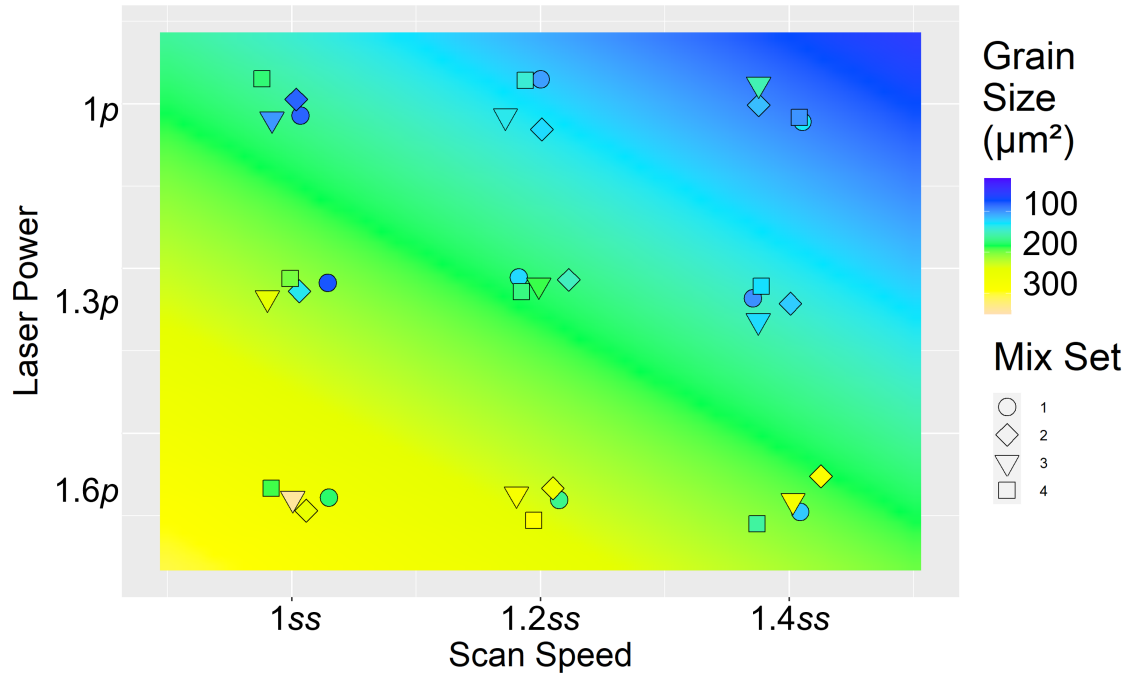


Figure 4.24. Average grain size for each sample plotted against build parameters. The background gradient shows the predicted values according to the model and the points represent the measured values. The same color scale applies to both predicted and measured values. The model has $R^2 = 0.57$.

It can be seen in Equations 4.6 and 4.7 that the mixing parameters (MC and MT) don't have a large effect compared to the AM parameters (LP and SS). Also, in both models, the laser power has $\sim 3\times$ the impact as scan speed does on the grain metrics. The relationship between the combination of scan speed and laser power with effect on the AM parts is mentioned in numerous studies.^{43–45} The 2019 study by Polozov et al., instead says that scan speed is the most impactful parameter, as determined by their

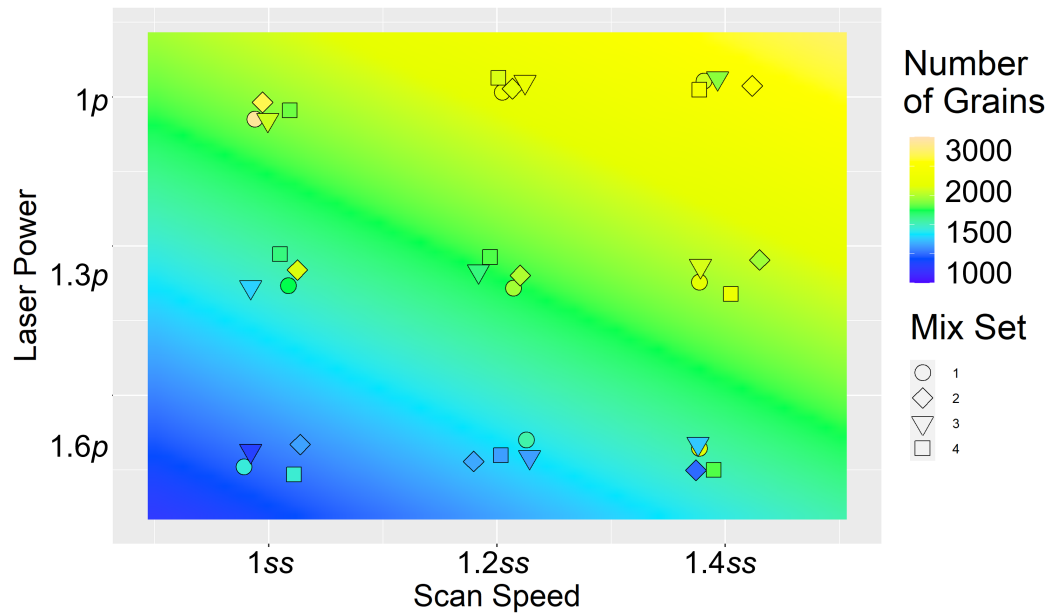


Figure 4.25. Average number of grains per sample plotted against build parameters. The background gradient shows the predicted values according to the model and the points represent the measured values. The same color scale applies to both predicted and measured values. The model has $R^2 = 0.70$.

Pareto chart.⁴⁰ A qualitative assessment of melt tracks of SLM steel samples grouped the results from various laser power and scan speed combinations by melting cases. While they note the combined parameters' impact on the SLM samples, they do not quantify the relationship.⁴¹ The study by Kohorasani et al., which utilized an artificial neural network to make conclusions about the most influential parameter on material surface characteristics, modeled the relationship between laser power, scan speed, and surface quality with similar slope as the models in this work. While the model was assessing AM parameters in relation to surface quality instead of grains, it still validates the laser power and scan speed relationships found in this study.⁴² Most of the AM parameter studies do not quantify the effect with a model, however, like the current study does. Quantifying

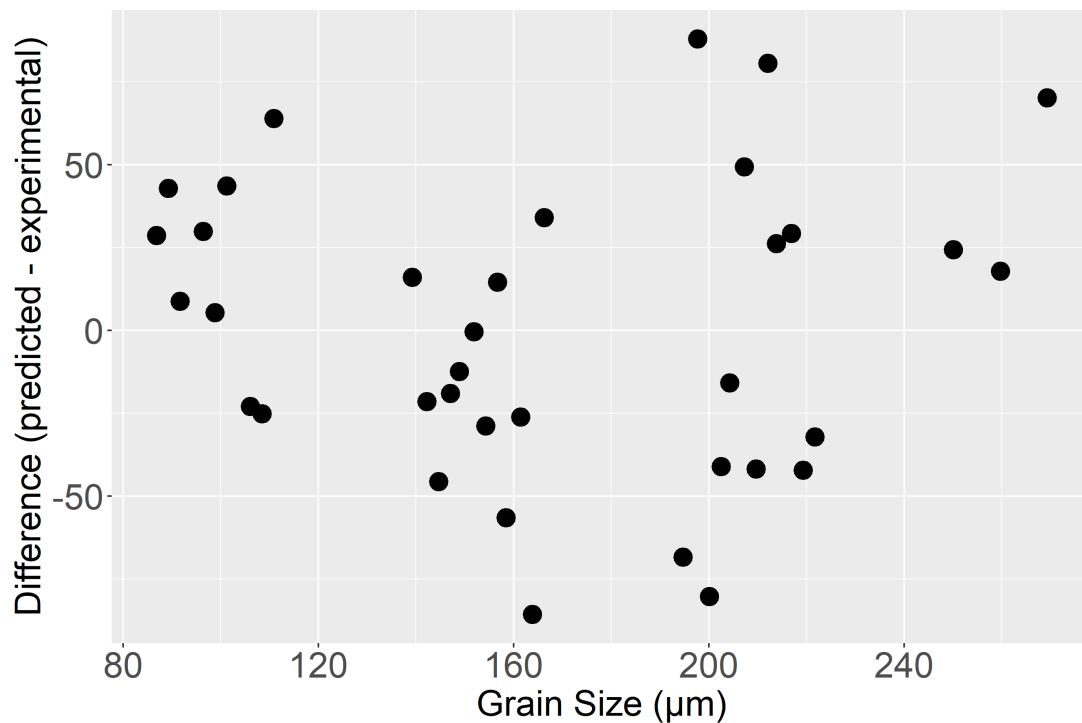


Figure 4.26. Residuals plot from the average grain size vs processing parameters model. The random nature of the residuals indicate that a linear fit was appropriate for the model.

and modeling the impact of specific AM processing parameters aids in defining the processing window and understanding the design space.

The two main strengthening mechanisms for ODS materials are believed to be Hall-Petch or other precipitation-based at lower temperatures^{52,53} and Orowan at higher temperatures.^{26,52–54,81} The increased number of grain boundaries in samples built with lower laser powers should contribute to the lower/standard temperature strength of the material. The major appeal of ODS materials is their strength at high temperatures, and it is the oxide distribution that will contribute to the material strength in that regime, and the oxide distribution does not seem to be affected by build or mix parameters.

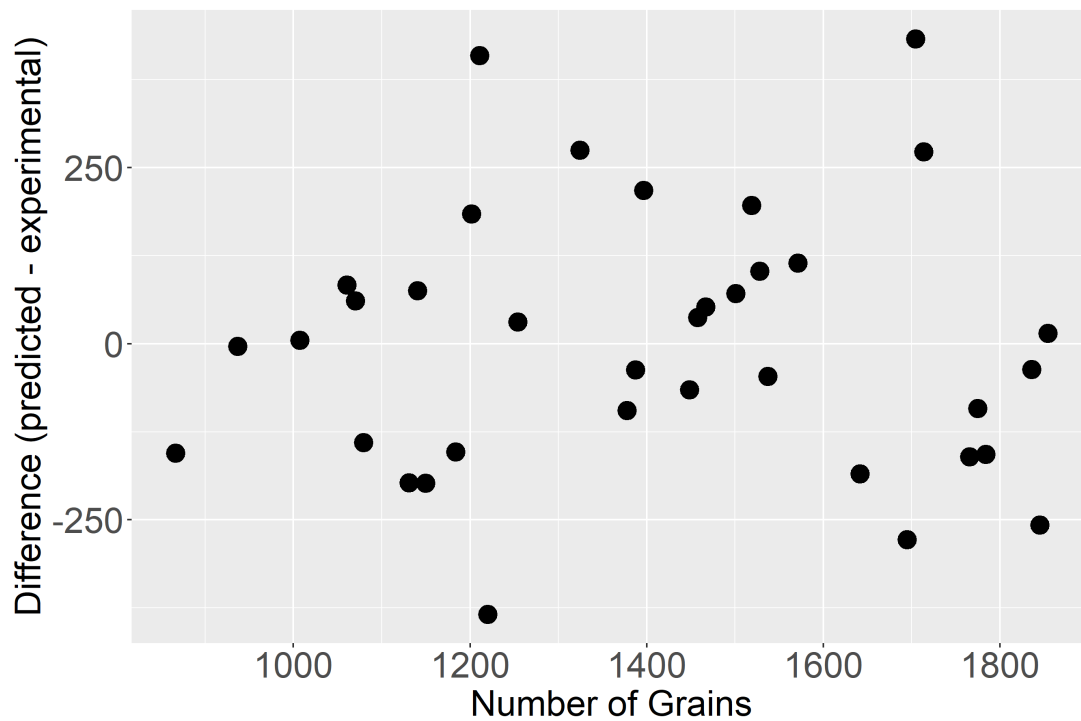


Figure 4.27. Residuals plot from the number of grains vs processing parameters model. The random nature of the residuals indicate that a linear fit was appropriate for the model.

4.4.4 Oxide Homogeneity Issues

Oxide homogeneity is critical in ODS materials.^{30,49} Both the oxide image analysis results (Figure 4.14) and the TOF-SIMS results (Figure 4.16) from bulk sample analysis show inconsistencies in the amount of oxide detected in the bulk samples. The samples tested from Mix Set 1, from both analysis types, show taller boxes in the box plots than the boxes from the other Mix Set. These results show that the inhomogeneity of the powder coating as a result of different mixing parameters (Table 3.3) translates to inhomogeneity of the oxide distribution in the printed parts. Although the melt pools in LPBF processes are known to be very turbulent, they are insufficient to homogeneously

distribute the yttria in parts printed from inhomogeneously oxide coated feedstock powder.^{17,141,142} The idea that poor feedstock powder preparation translates to poor qualities in the printed material is supported in a study modeling the impact of LPBF parameters on the surface quality of Ti-6V-4Al. The study confirms that the pre-processing parameters have an effect on the surface quality of LPBF-built parts.⁴²

The same inhomogeneity is not seen in the powder TOF-SIMS results (Figure 3.4), but this both confirms the conclusion from Chapter 3 that higher mixing time combined with higher mixing condition yield a better oxide coating and indicates that the printing process and what happens to the powder in the melt pools impact the oxide distribution in the printed material. This does not negate the conclusion that the LPBF process cannot completely correct poorly coated powder.

4.4.5 Idealized Property Discussion

One objective of this study was to see how idealized samples of ODS NiCoCr compared to similar materials. Figure 4.28 shows the yield strength values from similar material from multiple studies and the current results. This provides a frame of reference for how this dissertation's material relates to the strength of other MPEA, NiCoCr, ODS, and Ni-based superalloy materials. Elevated temperature results are shown in Table 4.7. The

The room temperature tensile tests from Han et al., showed fairly comparable results to the current study, but the small increase in yield stress can likely be attributed to smaller grain sizes in the NiCoCr material studied by Han et al., which exhibited higher Hall-Petch type strengthening.⁹² The difference in material processing likely contributed to the decreased yield stress seen in the study by Quao and colleagues.¹¹ Wu and colleagues also supported the strengthening effects of Cr additions to alloys in their

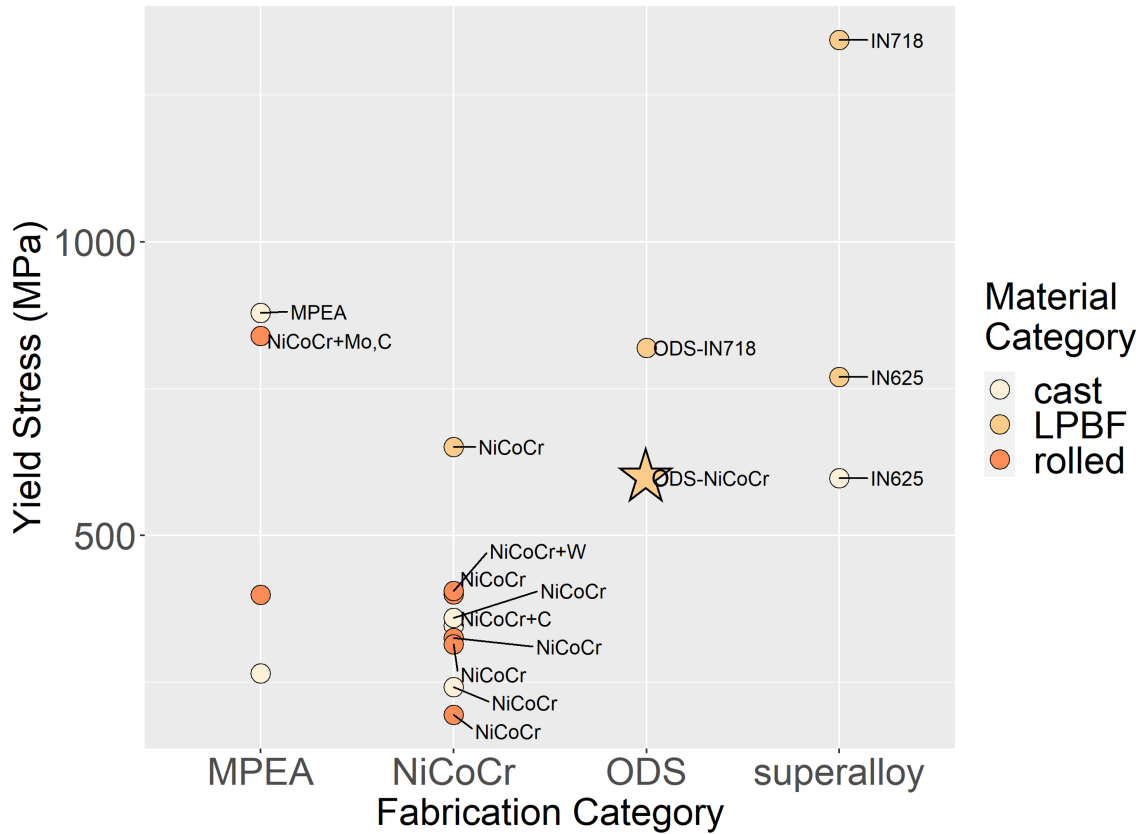


Figure 4.28. Yield strength of materials similar to ODS NiCoCr from room temperature tensile tests. The ODS NiCoCr from this work is marked with a star. The data points are grouped by material category, colored by fabrication category, and represent data from multiple studies.^{3–16}

Chemistry	Fabrication Method	Temp	Yield Stress (MPa)
ODS NiCoCr (this dissertation)	LPBF	1366K	89.6
NiCoCr ⁸	rolled	673K	~200
IN 718 ¹²	LPBF	923K	1061 (9)
IN 625 ¹³	rolled	1273K	98
IN 625 ¹⁴	LPBF	973K	520
Al ₁₀ Co ₂₅ Cr ₈ Fe ₁₅ Ni ₃₆ Ti ₆ + Hf, Mo ¹⁴³	cast	1173K	219 (6)
CoFeNi ₂ V _{0.5} Mo _{0.2} ¹⁴⁴	cast	1073K	187

Table 4.7. Comparative table of yield strengths for elevated temperature tension tests.

2014 work. Their study concluded that grain boundary strengthening was not a significant contributor to the temperature dependent differences in yield strength.⁸ None of the materials in that study were dispersion strengthened, and as grain boundary pinning is one of the prominent strengthening mechanisms present in ODS materials, it makes sense that the RT yield strength of the ODS NiCoCr is higher than that for similar (grain size) material, like from the Wu et al., study.

While not disregarding the factors contributing to the differences in results, the similarities in the various materials allude to explanations of the strength seen in the current study's material. Shang et al., saw effects of interstitial strengthening in their NiCoCr experiments. As they increased the amount of carbon solutioned into their material, they saw increase in strength without detriment to ductility.³ In their review of mechanical properties of HEAs, Shang et al., summarize many theories of material strengthening which center around the micro twinning known to occur in NiCoCr.¹⁴⁵ Laplanche and colleagues found that equiaxed grained NiCoCr had superior mechanical properties to equiaxed grained NiCoCrFeMn, primarily due to the earlier onset of nanotwins under strain.^{9,10} Chang and colleagues found that additions of W to their NiCoCr increased the strength of the material through retardation of grain boundary and dislocation motion during recrystallization.⁵ A study by Hu et al., looked at precipitation and solute strengthening with Mo and C additions to NiCoCr. They found that both additions to the NiCoCr provided a combined effect of solute drag and Zener pinning to strengthen their material. The grain size for their materials was much smaller (1-6 μm) than those used in the dissertation and the precipitate sizes were somewhat larger (100-550 nm) than the oxide particles in the dissertation.⁴ Both of these size factors contribute to different strengthening mechanisms being at play in the materials. Despite these differences, the

strengthening they saw with additions to the NiCoCr amounted to a rough doubling of yield stress.⁴

Borg et al., compiled a summary of the mechanical properties of over 600 MPEAs. At room temperature, the yield strengths ranged from ~250 MPa to ~2000 MPa, and at roughly 2000 °F (1366K), the yield strength range was from ~100 MPa to ~750 MPa.¹⁴⁶ The samples for this dissertation lie at ~30% of the maximum RT measurement and at the bottom of the range for high temperature measurements. While NiCoCr may not be the highest strength MPEA, it has other favorable qualities, including being chemically simple and making a good model system, that influenced its selection as the material for this dissertation. When compared to the other material examples (Figure 4.28 and Table 4.7), this project's ODS NiCoCr showed equivalent to superior yield strength at room temperature and comparable yield strength at high temperature. The Ni-based superalloys showed higher strengths, but these materials were tailored specifically to have such high strengths.

Figures 4.29 and 4.30 show how these results compare to the results from unmixed NiCoCr and mixed ODS NiCoCr also produced at NASA Glenn from the same starting materials and same mixing methods, but with different mixing parameters.¹⁷ The samples for this dissertation were more ductile at RT (but less at high temperature) compared to the ODS NiCoCr from Smith et al. This difference most likely due to the different processing parameters used in AM of the samples, which lead to increased slag in the samples for the dissertation.^{63,147} More slag would have more of an influence at high temperatures, which is why the strength at room temperature is comparable among the samples, but the stress-strain curve at high temperature shows a significant difference.

The difference in the ODS vs non-ODS samples is also more significant at higher temperatures owing to the oxides providing more strength (Orowan mechanism) than at room temperatures (where Hall-Petch dominates).^{52,53}

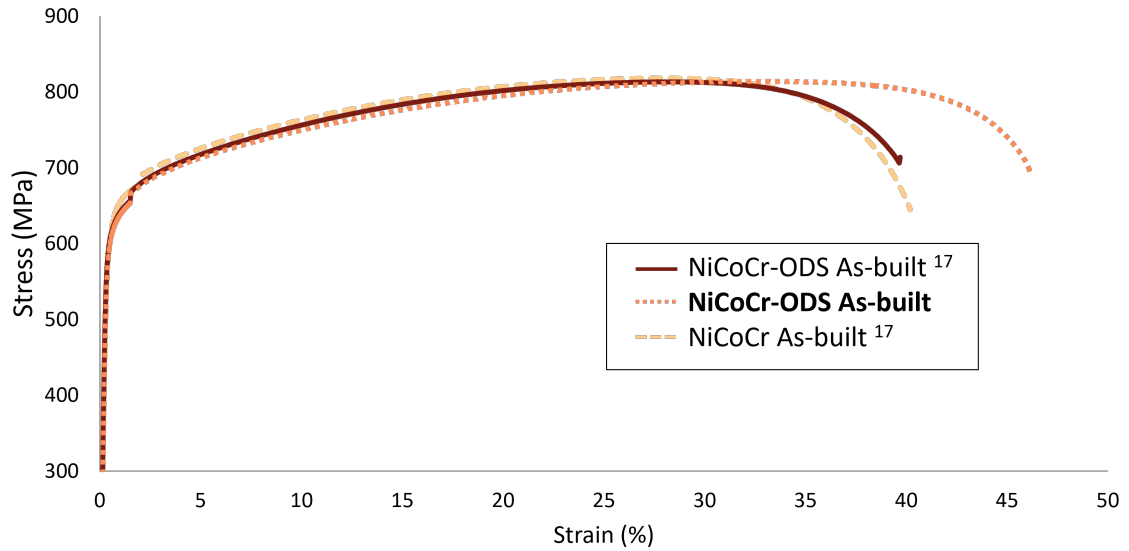


Figure 4.29. Room temperature engineering stress-strain tensile test results for non-mixed NiCoCr, ODS NiCoCr mixed with different parameters than this project, and ODS NiCoCr from this dissertation (bold). This figure shows data from both this dissertation and Smith et al., 2020.¹⁷

4.5 Conclusions

Several screening experiments were performed on the AM ODS NiCoCr to investigate how the print parameters impacted the density, porosity, and grain size distribution of LPBF printed multi-feature blocks. The scrutiny of the Archimedes' density and porosity (with metallographic sample preparation and image analysis) revealed that Archimedes' density can be used to quickly rank samples to find the lowest porosity. The grain size and number analyses showed that laser parameters are the primary indicator of grain size, and that laser power has a larger impact than scan speed.

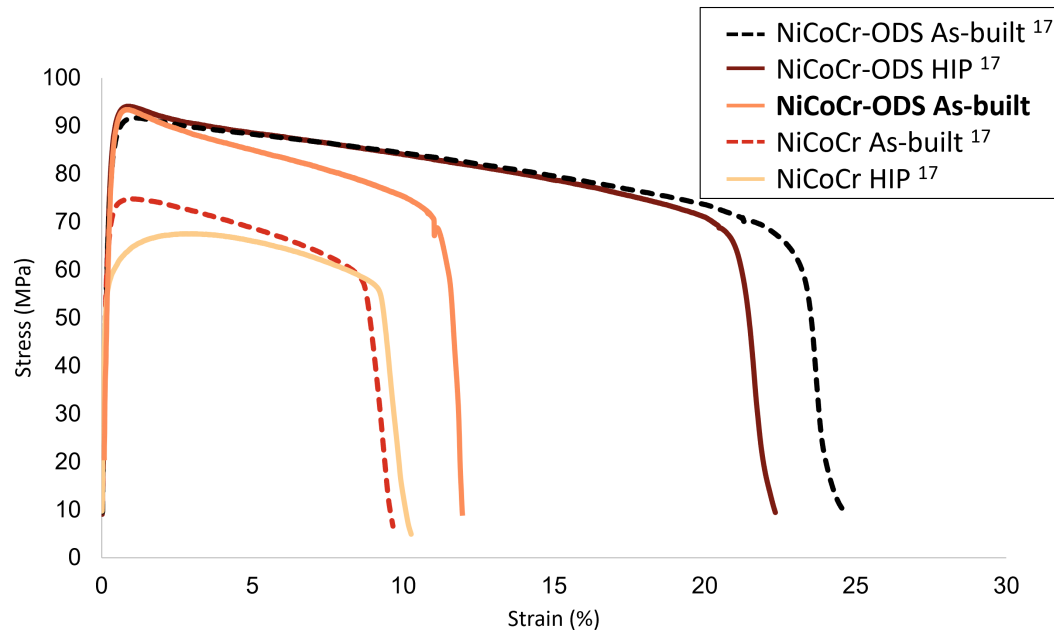


Figure 4.30. Elevated temperature engineering stress-strain tensile test results for non-mixed NiCoCr, ODS NiCoCr mixed with different parameters than this project, and ODS NiCoCr from this dissertation (bold). This figure shows this dissertation's data added to the results from Smith et al., 2020.¹⁷

After comparing the oxide distribution, both by code driven oxide distribution image analysis and TOF-SIMS, of multi-feature blocks printed with idealized AM parameters, it was concluded that any mixing occurring in the melt pool is insufficient to alleviate inhomogeneously mixed feedstock powder. Yield strength was also gathered from tensile samples of the ODS NiCoCr built with idealized AM parameters, and the results, when compared with similar materials, were comparable. When compared to the similar material also built at NASA Glenn, the material in this study was between ODS and non-ODS NiCoCr in high-temperature tensile tests and superior to both at room temperature.

5 Overall Conclusions

5.1 Powder Experiment Conclusions

The powder experiments were discussed in Chapter 3. These experiments were designed to understand the impact of the powder preparation parameters on the quality of the oxide distribution on the composite material. The powders mixed were a multi-principle element alloy, NiCoCr, which was nominally 25 μm in diameter and an oxide, yttria, which was roughly 100-200 nm in diameter. The oxide powder was added to the metal powder at a 1:99 weight ratio and combined using an acoustic resonance mixer (Resodyn³⁷). The mixing parameters in question were the mixing time and a condition fairly equivalent to energy input. Previous studies have shown that these are the main variables that can impact the extent of the mix in an acoustic mixer.³⁷⁻³⁹

The impact of these parameters on the distribution of yttria on the surface of the NiCoCr powder was evaluated qualitatively through analysis of secondary electron images of both whole and cross-sectioned mixed powder samples. A framework for characterizing the powder coatings was used to determine which mixing parameter combinations yielded the best and worst coatings on the powders. The framework considered percent coverage, consistency, and thickness of the oxide coating (this was tabulated in Table 3.3).

In order to understand the quantitative impact that the various mixing parameter combinations had on the oxide coating, Time of Flight Secondary Ion Mass Spectrometry (TOF-SIMS) was used to measure the amount of yttrium on the surface of the mixed ODS NiCoCr powders mixed with seventeen different parameter combinations. These evaluations indicated that more mixing time was advantageous to less, to an extent, and that higher mixing condition (energy) resulted in more yttrium on the surface of the powders.

Overall, these experiments proved that quantitative (or semi-quantitative by TOF-SIMS) or qualitative (SEM/EDS) evaluation of the surface of the ODS powder can help determine mixing parameters that will give homogeneous oxide distribution. The results from both are shown in Figure 5.1. The importance of a homogeneously distributed oxide in ODS materials is supported in numerous studies.^{19,30,49}

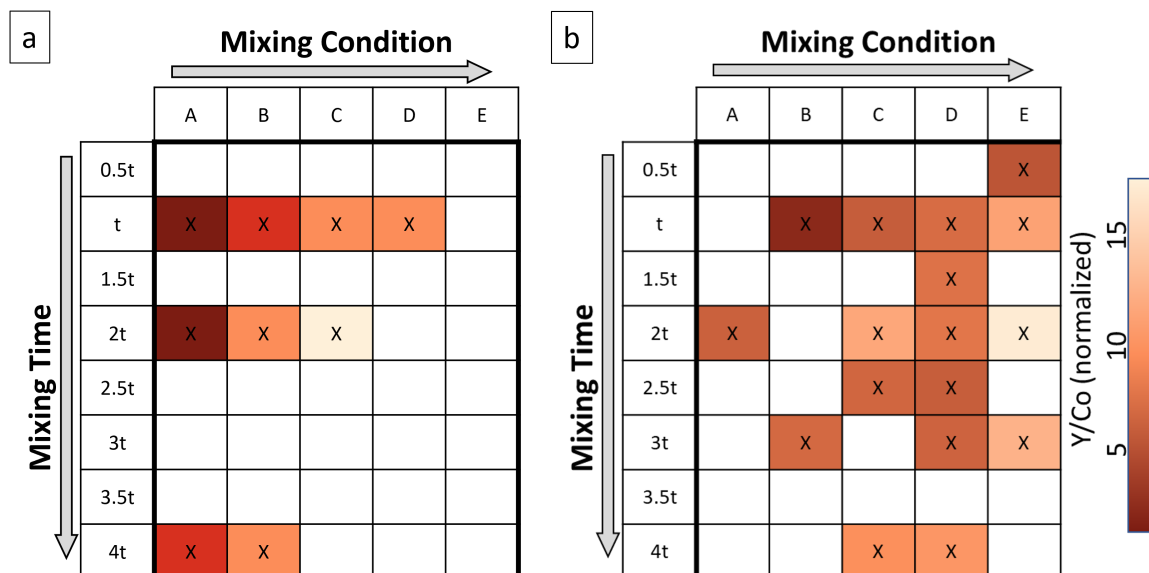


Figure 5.1. Results of the qualitative analysis (a) and the semi-quantitative analysis (b) both imposed on the mixing parameter matrix. Both tables follow a similar hue map coloration, with darkest boxes representing poor coatings with less yttrium, lightest boxes representing good coatings with the most yttrium, and intermediate boxes representing intermediate values.

5.2 Printed Material Conclusions

The experiments on the printed ODS NiCoCr material were divided into screening experiments and property evaluations of idealized material.

The screening experiments consisted of porosity, density, grain size, and number of grain analyses of thirty-six printed multi-feature blocks. The blocks were printed from material mixed with four different mixing parameter sets and following a 3x3 matrix of laser power and scan speeds (nine blocks). The mixing parameter sets included poorly coated, best coated, and intermediately coated powders, as determined in Chapter 3. The lack of statistically significant difference between either the porosity, density, or grain metrics for the powders mixed with different conditions indicate the robustness

of the ODS NiCoCr material production. The results also provided documented evidence Archimedes' density can be used as a quick screening tool to rank samples by their porosity. Additionally, the models created from the results of the grain size and number analyses showed that laser power had a greater impact on the grain metrics than the scan speed. A side by side figure of the screening experiment results is shown in Figure 5.2.

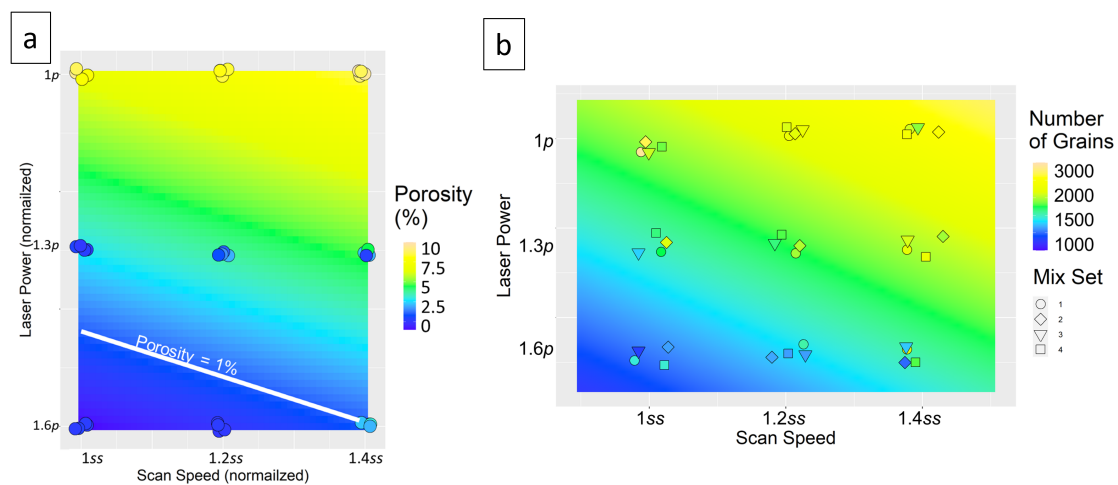


Figure 5.2. Results of the screening analyses. The left plot (a) shows the results of the EBSD analysis of the grain size and the right plot (b) shows the porosity results. Both plots are colored following the models of the respective analyses and indicate the idealized AM parameters are indicated in the lower-left corner (1.3-1.6 for laser power and 1-1.2 for scan speed).

Following the determination of which laser power and scan speed combinations yielded fully dense printed material^{35,36,50,51}, tensile samples were printed and tested. The yield stress and ultimate tensile strength were calculated from both room temperature and 2000 °F tension tests and compared to similar materials (Figure 4.28 and Table 4.7). The room temperature and elevated temperature stress-strain curves from this material and another ODS NiCoCr and non-ODS NiCoCr (from Smith et. al.¹⁷) are shown in Figure 5.3.

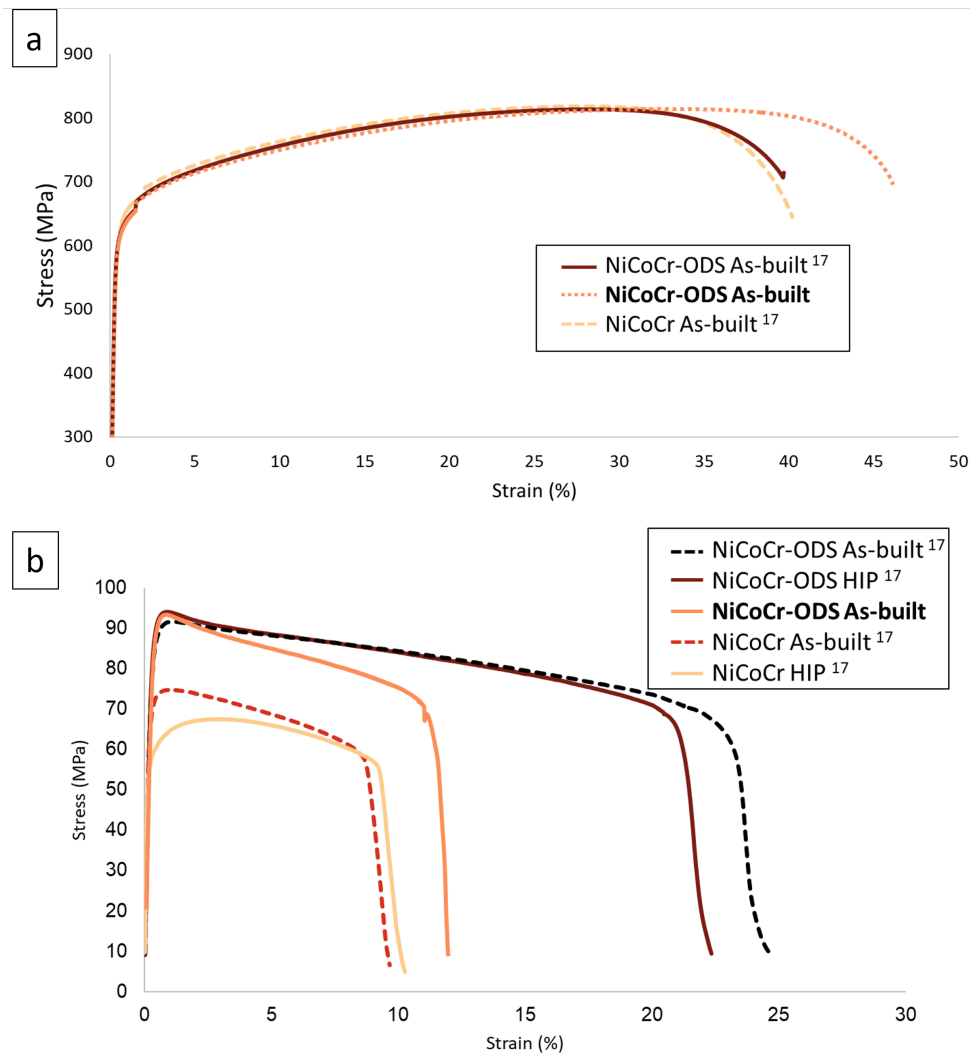


Figure 5.3. Results of the engineering stress-strain tension tests on idealized LPBFAM produced ODS NiCoCr material. The top plot (a) shows the stress-strain curve from the room temperature tension tests, and the bottom plot (b) shows the stress-strain curve for the elevated temperature tension tests. Both plots include results from this analysis as well as the material printed from the similar project at NASA Glenn¹⁷.

The final outcome of the printed material experiments, again on idealized printed material, was that a poor coating of oxide during the mixing phase translates to an inhomogeneous distribution of oxide in the printed material. This was determined from

both oxide distribution metrics calculated from image analysis of SEM micrographs of the printed material as well as from TOF-SIMS area analyses of the printed material. In both sets of experiments, the samples mixed with mixing parameters shown (in Chapter 3) to result in less yttrium on the surface of the NiCoCr powder showed wider distributions of oxide in the printed material than the others. This is illustrated in Figure 5.4.

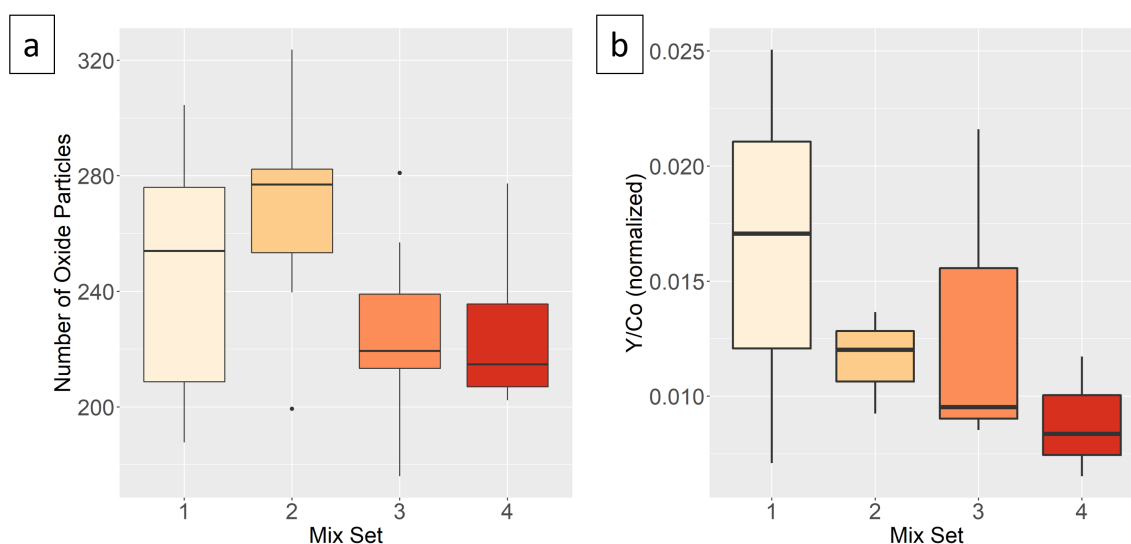


Figure 5.4. Results of the oxide distribution result (a) and the TOF-SIMS results (b) from the idealized printed samples. The results from Mix Set 1, which is mixing condition C and time 2t, shows a wider distribution of values, as indicated by the height of the box in both box plots. This suggests an inhomogeneous oxide distribution.

5.3 Overall Conclusion

When considered together, the results of the powder and printed material evaluations indicate that the combination of powder surface evaluation and printed component density can increase throughput of material development. High-throughput experimentation and lean approaches that strive to quickly eliminate failing materials are critical to achieve the goals of the aerospace industry in a timely manner. In an effort

to adopt these principles, evaluation of the oxide coating on the surface of acoustically mixed ODS powder can quickly indicate which mixing parameters result in a powder with a homogeneous oxide distribution. Once mixing parameters are determined, using Archimedes' density on LPBF AM parts to rank them by their porosity allows for a quick and simple screening determination of additive manufacturing parameters that result in a fully dense printed component. This can allow for expedited material development, which is imperative to high-throughput manufacturing principles.

5.4 Scientific Contributions

ODS NiCoCr powder prepared by acoustic mixing and additively manufactured is a new material that has been described in this dissertation and patented at NASA Glenn during the time of the dissertation. Novel characterization methodologies are presented in this study for characterizing this and similar materials. The characterization methodologies were applied as part of a well understood though seldom applied and documented iterative study design that employed loops to handle the multitude of variables and proved efficient experimentation. The overall contributions to the field that this project supplied are as follows:

- Acoustic mixing is shown to be a valid technique for combining dissimilarly sized oxide and metal powder that is fairly robust to the mixing parameters.
- The application of iterative study design and multiple project loops is documented.
- Numeric models are calculated to represent the impact of AM processing parameters on porosity and grain metrics of LPBF AMed samples. Though the relationships are noted in numerous studies, rarely are they quantified.

- TOF-SIMS is used in a novel application to characterize powder surface chemistry.
- A qualitative framework to characterize micrographs of powder surface is created and explained.
- The use of Archimedes' density as a quick tool to rank samples and screen AM parameters is presented.
- The combined use of qualitative or semi-quantitative powder surface analysis with Archimedes' density analyses is shown to be a valid high-throughput technique which can lead to process optimization of LPBF ODS material.

The findings from this study should apply to other ODS alloys for LPBF AM production in elevated temperature applications, as well.

6 Future Research

The sections in this chapter provide brief descriptions of both additional and further experiments and models that could be conducted with these and similar materials.

6.1 Optimization Studies

This project included screening and modeling experiments, as described by the NIST Engineering Handbook. Optimization is the final step in the design of experiments (DOE) outline and can be done with enough data to plot a response surface. This would allow for determining the minimum and maximum of a quadratic model, which would represent the desired output.⁴⁸ In order to optimize the mixing or AM parameters from this study, it would be necessary to collect more data. The semi-quantitative analysis in Chapter 3 evaluated seventeen samples, but wasn't able to define the entire response surface. Enough data is needed to model the local maximum or minimum, as well as the neighboring slope changes used to confirm that the high and low results are actually the extremum on the response surface. In order to quantitatively determine the extremum, quadratic modeling would be required.

6.2 Powder particle size vs Porosity

The current study did not include a large enough variety of particle size distributions to test the relationship between powder particle size and porosity, however this could be done through an extended mixing parameter space, such as the TOF-SIMS analyses from Chapter 3, combined with printing multi-feature blocks from those powder batches. Several previous studies have shown a correlation between powder size and porosity of the printed part.^{49,102} Roughly 5kg of powder is required to complete a print of multi-feature blocks on the EOS M100 at NASA Glenn, which is attained from combining 3 metal containers (900g full each) worth of mixed powder. Without knowing the standard deviation of the powder size distributions, the amount of samples can only be estimated. According to the NIST handbook of statistical methods, a sample size of 10 is estimated to be needed for a statistical correlation with 95% confidence interval with unknown standard deviation.⁴⁸ Therefore, at least 18 metal container samples would need to be produced and used to print 6 sets of multi-feature blocks to be able to quantify the powder particle size and bulk material porosity relationship.

6.3 Strength vs grain size

A number of studies have shown that grain size and dispersion extent have an effect on yield strength.^{4,8,11,71,92,102} Yield stress is affected by a combination of stresses, which include precipitate hardening and grain boundary strengthening.⁸ One study described how high grain aspect ratio (more than 10:1) were desirable for strength at very high temperatures for ODS alloys.⁷⁹ Wang et al., studied an AM Cantor alloy and related mechanically induced twins (a major strengthening element) to grain size. They determined a

critical grain size (and noted that this was hard to calculate for elongated grains) needed for the twins to form.¹⁰²

According to ASTM Standard E2627¹⁴⁸ and E1382,¹⁴⁹ at least five image frames encompassing at least 100 grains each with 500 or more indexed points is required to determine grain size. The EBSD frames collected from Loop 2 of this study included the correct number of grains, but only one image per sample was measured. At least four more EBSD maps would need to be collected per sample to properly determine the grain size. These results could couple with the mechanical test results to provide a quantitative correlation between grain size and mechanical strength for ODS NiCoCr.

6.4 Multivariate Linear Models and Beyond

This project included a number of multivariate linear models, but several of the correlations seen throughout this project would be better represented by non-linear models with quantified coefficients (yttrium vs mixing conditions correlations explored in Chapter 3 and shown in Figure 3.4). Non-linear models were outside the scope of the current project, but could help quantify those relationships.

6.5 Material Alternatives

Composite materials have long been studied for their favorable combinations of properties. Metal Matrix Composites have been studied for aerospace applications due to their lightweight, wear resistance, high strength, and high temperature resistance properties.^{150,151} Metal matrix nanocomposites, which are reinforced with nano-sized particles, have more recently been studied for aerospace applications.²⁷ Refractory metal complex alloys have also received interest in the aerospace industry for their superior

high temperature properties.⁷⁰ These fields of research may yield valuable material alternatives to ODS NiCoCr that offer similar or superior high temperature capabilities.

6.6 Micro-Fatigue and Full-Scale Fatigue Comparisons

(Yet) unpublished work has been exploring a mechanical testing method using scaled-down samples. The potential to validate the small-scale fatigue testing against full-scale fatigue tests could mean that accurate mechanical properties could be calculated without the need to create full-scale parts for evaluation. This (yet unpublished) work has been focusing on a copper alloy, GRCop-42, and as an additional validation step is set to include ODS NiCoCr samples. Full-sized fatigue testing sample bars have been machined out of LPBF ODS NiCoCr printed at NASA Glenn Research Center. The small-scale evaluations will be performed on sections of the multi-feature blocks used throughout this dissertation project.

Appendix A

Supplemental Experiments

1 Introduction

This appendix contains methodologies referenced to, but not described in the full body of the dissertation.

2 Particle Size Distribution

Particle size distribution was investigated using NASA Glenn's Horiba Partica LA-960V2 Laser Scattering Particle Size Distribution Analyzer following Horiba's standard procedures¹⁵² and according to ASTM-52907.¹²² In order to prepare for use, tap water was added to the chamber refill bucket under the machine and wipes and ethanol were made available. The computer program was set up to use water as the dispersion medium and Ni powder as the background reference material. Water was fed into the chamber, then an 'agitate and circulate' cycle was run. Alignment of the lasers was optimized for performance, followed by a de-bubbling cycle, and then the lasers were blanked. Using a metal spatula, a small amount of powder (1-5 grams) was added to the analysis chamber of the Horiba until the appropriate amount of particulates were detected by the machine (as indicated by the optimum zones marked on the red and blue laser level bars, roughly at 1000-1500 units). Once the powder was added to the water in the analysis chamber, the ultrasonic cycle was run for three minutes, followed by another de-bubble cycle. Once the normal measure cycle was concluded, the analysis chamber was drained, rinsed, and wiped clean with a paper towel and ethanol. The procedure was then repeated, beginning with feeding water into the chamber, for each analysis. A complete analysis of

each sample set consisted of six repetitions (measurement of six unique samples from each powder mix batch).

3 Morphologi Powder Dispersion Tool

The procedure for attaining an even powder dispersion on a carbon tape stub using the Malvern Morphologi Automated Particle Size & Shape Analyzer is as follows. After the computer and equipment are turned on and the software package Morphology is loaded, the air hose is first un-clipped and the dispenser removed. After removing the dispenser lid and blowing out the sample holder with the compressed air, the whole dispenser inside is wiped down with anti-static spray. Once the sample holder disc is replaced onto the dispenser, 5 mm³ of powder is placed into the center of the sample disc, using an appropriately sized dispensing spoon. The lid of the dispenser is then replaced and the dispenser and powder assembly is put back into its holder on the Malvern and reattached to the air hose. A SEM stub covered in carbon tape is then placed on the glass so that it will be moved to under the dispenser. Using the software, 'Measure' and then 'Disperse Sample' are then selected. On the next window, where pressure and time adjustments are made, 2 bars of pressure, 20 microseconds of air, and 60 seconds of rest were determined to be adequate for the powders used in this study. When done, the software's microscope view can be used to check the success of the powder dispersion. Selecting 'Load Position' in the Morphology software returns the sample glass slide to a position where the coated stub can be removed. The glass sample slide is then blown off and cleaned with lens cleaner and a Kim wipe.

Appendix B

Tension Test Result Figures

This Appendix contains the four stress/strain curves discussed in Chapter 4 and the engineering drawing used to machine the specimens.

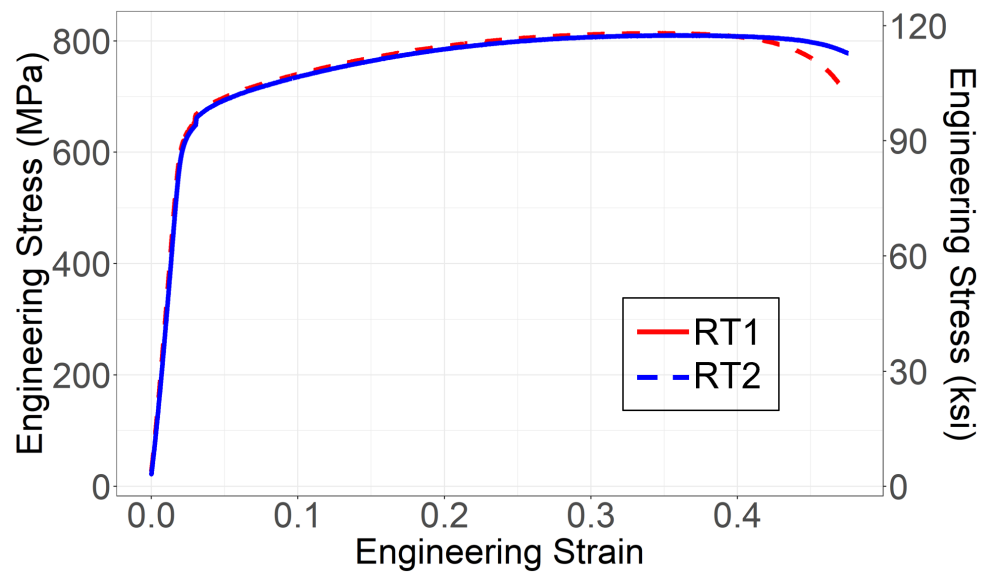


Figure B.1. Engineering stress/strain curves for room temperature tensile tests.

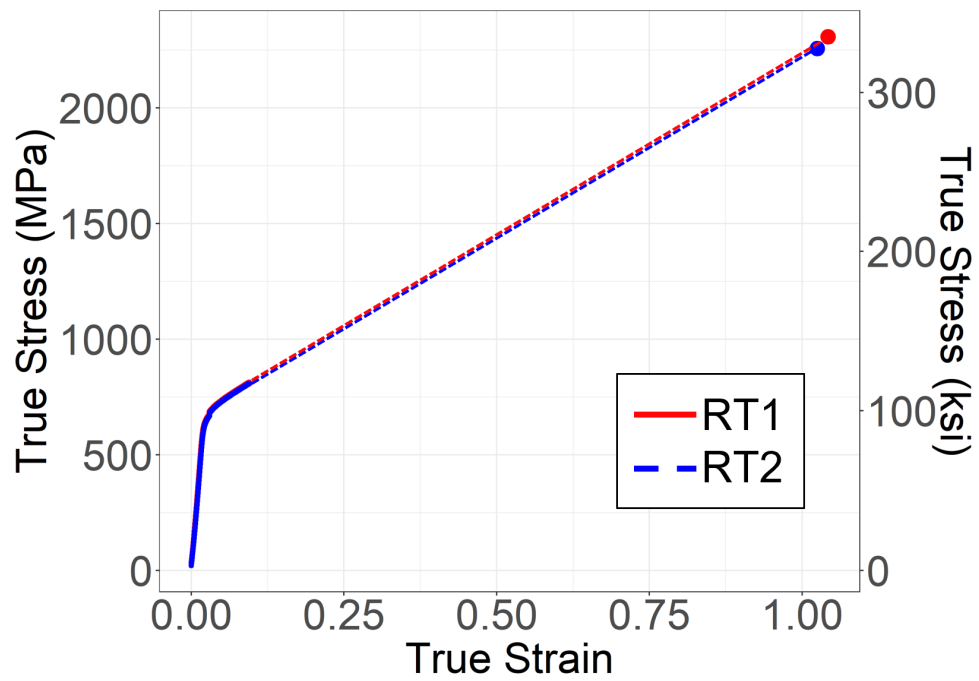


Figure B.2. True stress/strain curves for room temperature tensile tests.

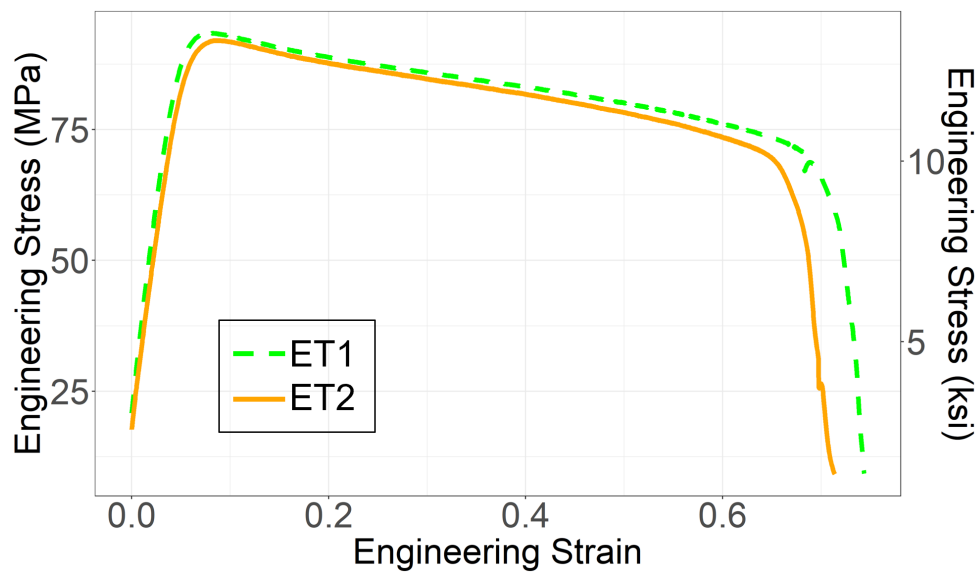


Figure B.3. Engineering stress/strain curves for 2000 °F tensile tests.

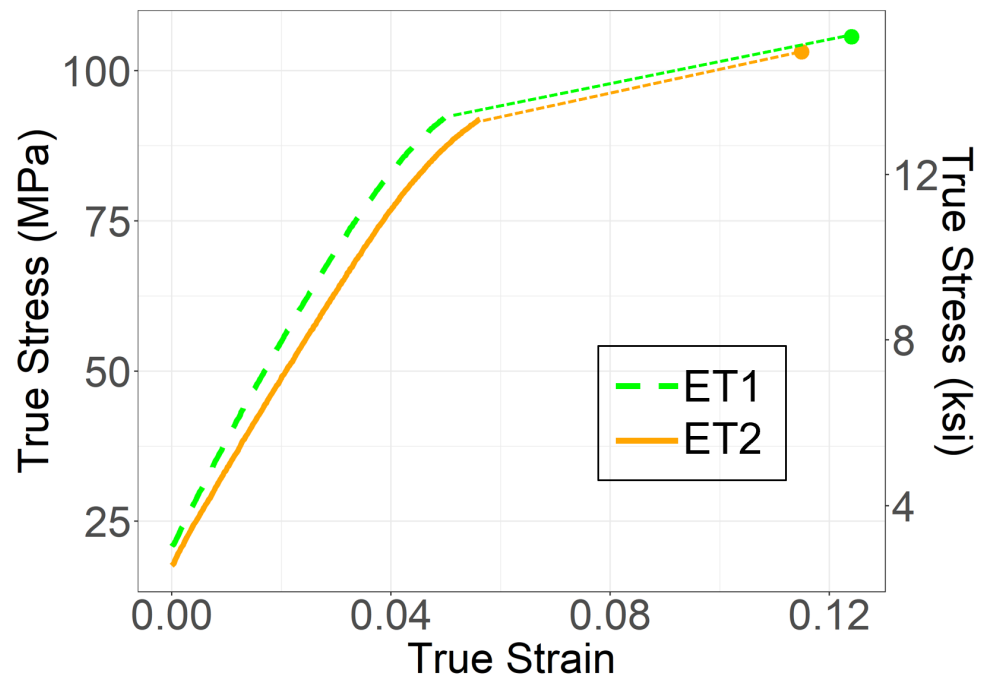


Figure B.4. True stress/strain curves for 2000 °F tensile tests.

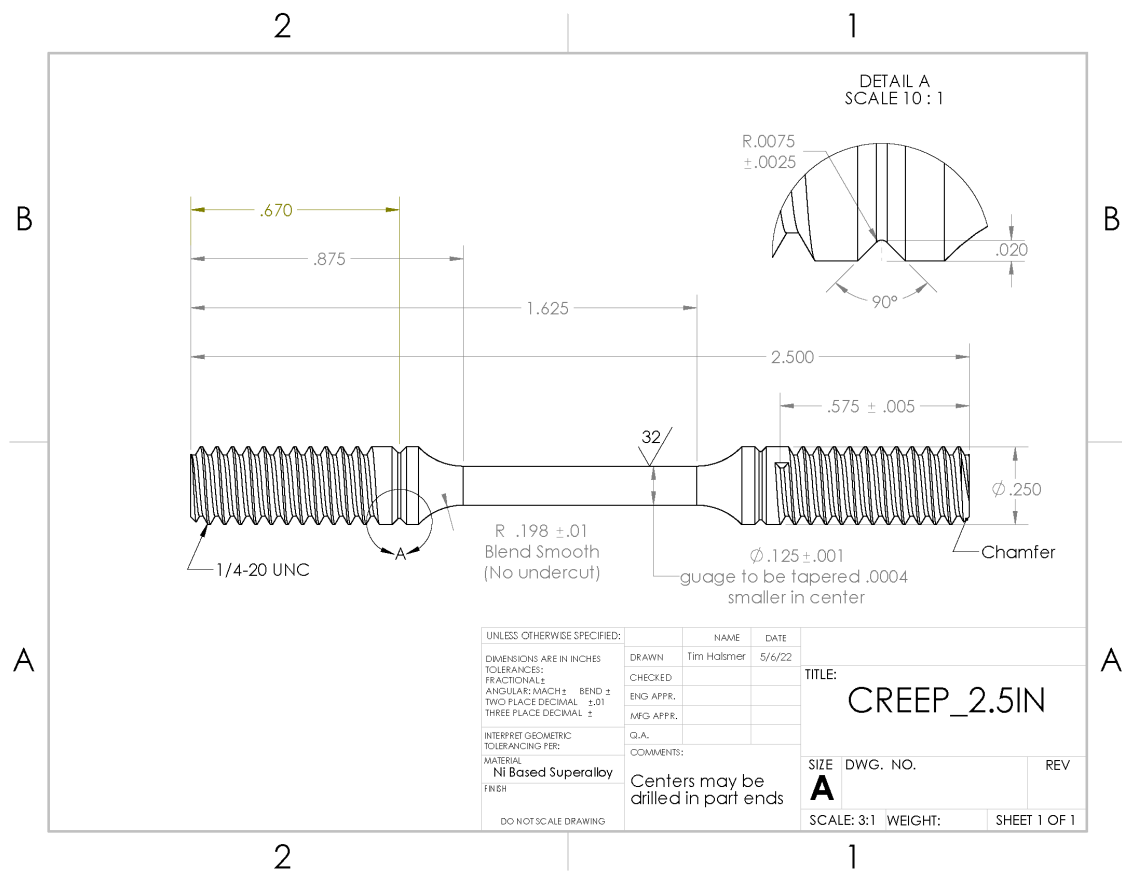


Figure B.5. Engineering drawing for the threaded tensile specimens.

Complete References

- [1] E28 Committee. ASTM-E8-04: Standard Test Methods for Tension Testing of Metallic Materials. Technical report, American Society for Testing and Materials, December 2011.
- [2] E28 Committee. ASTM-E21: Standard Test Methods for Elevated Temperature Tension Tests of Metallic Materials. Technical report, American Society for Testing and Materials, 2021.
- [3] Y. Y. Shang, Y. Wu, J. Y. He, X. Y. Zhu, S. F. Liu, H. L. Huang, K. An, Y. Chen, S. H. Jiang, H. Wang, X. J. Liu, and Z. P. Lu. Solving the strength-ductility trade-off in the medium-entropy NiCoCr alloy via interstitial strengthening of carbon. Intermetallics, 106:77–87, March 2019.
- [4] G. W. Hu, L. C. Zeng, H. Du, Q. Wang, Z. T. Fan, and X. W. Liu. Combined effects of solute drag and Zener pinning on grain growth of a NiCoCr medium-entropy alloy. Intermetallics, 136:107271, September 2021.
- [5] Ruobin Chang, Wei Fang, Xi Bai, Chaoqun Xia, Xin Zhang, Haoyang Yu, Baoxi Liu, and Fuxing Yin. Effects of tungsten additions on the microstructure and mechanical properties of CoCrNi medium entropy alloys. Journal of Alloys and Compounds, 790:732–743, June 2019.
- [6] Quanquan Han, Yuchen Gu, Rossitza Setchi, Franck Lacan, Richard Johnston, Sam L. Evans, and Shoufeng Yang. Additive manufacturing of high-strength crack-free Ni-based Hastelloy X superalloy. Additive Manufacturing, 30:100919, December 2019.
- [7] Binglun Yin, Shuhei Yoshida, Nobuhiro Tsuji, and W. A. Curtin. Yield strength and misfit volumes of NiCoCr and implications for short-range-order. Nat Commun, 11(1):2507, May 2020.
- [8] Z. Wu, H. Bei, G. M. Pharr, and E. P. George. Temperature dependence of the mechanical properties of equiatomic solid solution alloys with face-centered cubic crystal structures. Acta Materialia, 81:428–441, December 2014.
- [9] G. Laplanche, A. Kostka, C. Reinhart, J. Hunfeld, G. Eggeler, and E. P. George. Reasons for the superior mechanical properties of medium-entropy CrCoNi compared to high-entropy CrMnFeCoNi. Acta Materialia, 128:292–303, April 2017.

- [10] G. Laplanche, A. Kostka, O. M. Horst, G. Eggeler, and E. P. George. Microstructure evolution and critical stress for twinning in the CrMnFeCoNi high-entropy alloy. Acta Materialia, 118:152–163, October 2016.
- [11] Yu Qiao, Yan Chen, Fu-Hua Cao, Hai-Ying Wang, and Lan-Hong Dai. Dynamic behavior of CrMnFeCoNi high-entropy alloy in impact tension. International Journal of Impact Engineering, 158:104008, December 2021.
- [12] Qing Teng, Shuai Li, Qingsong Wei, and Yusheng Shi. Investigation on the influence of heat treatment on Inconel 718 fabricated by selective laser melting: Microstructure and high temperature tensile property. Journal of Manufacturing Processes, 61:35–45, January 2021.
- [13] Mauro M. de Oliveira, Antônio A. Couto, Gisele F. C. Almeida, Danieli A. P. Reis, Nelson B. de Lima, and Renato Baldan. Mechanical Behavior of Inconel 625 at Elevated Temperatures. Metals, 9(3):301, March 2019.
- [14] Jiwon Lee, Mathieu Terner, Sunyoung Jun, Hyun-Uk Hong, Etienne Copin, and Philippe Lours. Heat treatments design for superior high-temperature tensile properties of Alloy 625 produced by selective laser melting. Materials Science and Engineering: A, 790:139720, July 2020.
- [15] M. Yesim Yalcin, Bora Derin, and Eda Aydogan. Development and additive manufacturing of oxide dispersion strengthened inconel 718: Thermochemical and experimental studies. Journal of Alloys and Compounds, 914:165193, September 2022.
- [16] Y. D. Wu, Y. H. Cai, T. Wang, J. J. Si, J. Zhu, Y. D. Wang, and X. D. Hui. A refractory Hf25Nb25Ti25Zr25 high-entropy alloy with excellent structural stability and tensile properties. Materials Letters, 130:277–280, September 2014.
- [17] T. M. Smith, A. C. Thompson, T. P. Gabb, C. L. Bowman, and C. A. Kantzos. Efficient production of a high-performance dispersion strengthened, multi-principal element alloy. Sci Rep, 10(1):9663, June 2020.
- [18] Pierre Caron and Tasadduq Khan. Evolution of Ni-based superalloys for single crystal gas turbine blade applications. Aerospace Science and Technology, 3(8):513–523, December 1999.
- [19] T. K. Glasgow. An oxide dispersion strengthened Ni-W-Al alloy with superior high temperature strength. In Intern. Symp., 12-15 Sep. 1976, United States, January 1976.
- [20] G. W. Meetham. High-temperature materials — a general review. J Mater Sci, 26(4):853–860, February 1991.

- [21] Joyce A. Dever, Michael V. Nathal, and James A. DiCarlo. Research on High-Temperature Aerospace Materials at NASA Glenn Research Center. Journal of Aerospace Engineering, 26(2):500–514, April 2013.
- [22] William Bryan. 2020 NASA Technology Taxonomy. <http://www.nasa.gov/offices/oct/taxonomy/index.html>, August 2019.
- [23] Ezinne E Eop. National strategy for ADVANCED MANUFACTURING.
- [24] Junyang He, Surendra Kumar Makineni, Wenjun Lu, Yuanyuan Shang, Zhaoping Lu, Zhiming Li, and Baptiste Gault. On the formation of hierarchical microstructure in a Mo-doped NiCoCr medium-entropy alloy with enhanced strength-ductility synergy. Scripta Materialia, 175:1–6, January 2020.
- [25] X. W. Liu, G. Laplanche, A. Kostka, S. G. Fries, J. Pfetting-Micklich, G. Liu, and E. P. George. Columnar to equiaxed transition and grain refinement of cast Cr-CoNi medium-entropy alloy by microalloying with titanium and carbon. Journal of Alloys and Compounds, 775:1068–1076, February 2019.
- [26] Bei Jia, XiongJun Liu, Hui Wang, Yuan Wu, and ZhaoPing Lu. Microstructure and mechanical properties of FeCoNiCr high-entropy alloy strengthened by nano-Y2O3 dispersion. Sci. China Technol. Sci., 61(2):179–183, February 2018.
- [27] F. A. Mirza and D. L. Chen. A Unified Model for the Prediction of Yield Strength in Particulate-Reinforced Metal Matrix Nanocomposites. Materials (Basel), 8(8):5138–5153, August 2015.
- [28] E. Arzt and P. Grahle. High temperature creep behavior of oxide dispersion strengthened NiAl intermetallics. Acta Materialia, 46(8):2717–2727, May 1998.
- [29] J Whittenberger. Creep and Tensile Properties of Several Oxide Dispersion Strengthened Nickel Base Alloys, volume 8. July 1977.
- [30] G. Mervin Ault and H. M. Burte. Technical Applications for Oxide Dispersion-Strengthened Materials. In Metallurgical Society of America Conference.
- [31] John S. Benjamin. Dispersion strengthened superalloys by mechanical alloying. MT, 1(10):2943–2951, October 1970.
- [32] B. Triffleman. Manufacturing Techniques for Oxide Dispersion-Strengthened Alloys. In OXIDE DISPERSION STRENGTHENING, volume 47, pages 675–694, Bolton Landing, NY, 1966. Gordon and Breach, Science.
- [33] R. L. Dreshfield. The continuing battle against defects in nickel-base superalloys. In TMS Annual Meeting, 2-6 Mar. 1986, United States, January 1986.

- [34] Brian James. Powder Metallurgy Methods and Applications. In P. Samal and J. Newkirk, editors, Powder Metallurgy, pages 9–19. ASM International, 2015.
- [35] Y. Kok, X. P. Tan, P. Wang, M. L. S. Nai, N. H. Loh, E. Liu, and S. B. Tor. Anisotropy and Heterogeneity of Microstructure and Mechanical Properties in Metal Additive Manufacturing: A Critical Review. Materials & Design, 139:565–586, February 2018.
- [36] John J. Lewandowski and Mohsen Seifi. Metal Additive Manufacturing: A Review of Mechanical Properties. Annu. Rev. Mater. Res., 46(1):151–186, July 2016.
- [37] Industrial Mixing and Processing Products.
- [38] Juan G. Osorio and Fernando J. Muzzio. Evaluation of resonant acoustic mixing performance. Powder Technology, 278:46–56, July 2015.
- [39] Scott Coguill and Zilda Martineau. Vessel Geometry and Fluid Properties Influencing Mix Behavior for ResonantAcoustic ® Mixing Processes. June 2012.
- [40] Igor Polozov, Vadim Sufiiarov, Artem Kantyukov, and Anatoly Popovich. Selective Laser Melting of Ti2AlNb-based intermetallic alloy using elemental powders: Effect of process parameters and post-treatment on microstructure, composition, and properties. Intermetallics, 112:106554, September 2019.
- [41] Pavel Hanzl, Miroslav Zetek, Tomáš Bakša, and Tomáš Kroupa. The Influence of Processing Parameters on the Mechanical Properties of SLM Parts. Procedia Engineering, 100:1405–1413, 2015.
- [42] Amir Mahyar Khorasani, Ian Gibson, AmirHossein Ghasemi, and Alireza Ghaderi. Modelling of laser powder bed fusion process and analysing the effective parameters on surface characteristics of Ti-6Al-4V. International Journal of Mechanical Sciences, 168:105299, February 2020.
- [43] Inmaculada Lopez-Galilea, Benjamin Rutttert, Junyang He, Thomas Hammer-schmidt, Ralf Drautz, Baptiste Gault, and Werner Theisen. Additive manufacturing of CMSX-4 Ni-base superalloy by selective laser melting: Influence of processing parameters and heat treatment. Additive Manufacturing, 30:100874, December 2019.
- [44] L.N. Carter, M. M. Attallah, and R. C. Reed. Laser Powder Bed Fabrication of Nickel-Base Superalloys: Influence of Parameters; Characterization, Quantification and Mitigation of Cracking. Superalloys 2012, pages 577–586, 2012.

- [45] Haijun Gong, Hengfeng Gu, Kai Zeng, J.j.s Dilip, Deepankar Pal, Brent Stucker, Daniel Christiansen, Jack Beuth, and John Lewandowski. Melt Pool Characterization for Selective Laser Melting of Ti-6Al-4V Pre-alloyed Powder. August 2014.
- [46] David C. Wynn and Claudia M. Eckert. Perspectives on iteration in design and development. Res Eng Design, 28(2):153–184, April 2017.
- [47] Robert P. Smith and Pramanata Tjandra. Experimental observation of iteration in engineering design. Research in Engineering Design, 10(2):107–117, June 1998.
- [48] NIST. NIST/SEMATECH e-Handbook of Statistical Methods. 2013.
- [49] Eskandar Fereiduni, Ali Ghasemi, and Mohamed Elbestawi. Characterization of Composite Powder Feedstock from Powder Bed Fusion Additive Manufacturing Perspective. Materials, 12(22):3673, January 2019.
- [50] Xingfang Cai, Andrew Malcolm, Brian Wong, and Zheng Fan. Measurement and characterization of porosity in aluminium selective laser melting parts using X-ray CT. Virtual and Physical Prototyping, 10:1–12, November 2015.
- [51] Moataz M. Attallah, Rachel Jennings, Xiqian Wang, and Luke N. Carter. Additive manufacturing of Ni-based superalloys: The outstanding issues. MRS Bulletin, 41(10):758–764, October 2016.
- [52] Dheepa Srinivasan, Reed Corderman, and P. R. Subramanian. Strengthening mechanisms (via hardness analysis) in nanocrystalline NiCr with nanoscaled Y2O3 and Al2O3 dispersoids. Materials Science and Engineering: A, 416(1):211–218, January 2006.
- [53] Michel Ngranbe and Martin Heilmaier. Modelling of particle strengthening in the γ' and oxide dispersion strengthened nickel-base superalloy PM3030. Materials Science and Engineering: A, 387–389:609–612, December 2004.
- [54] Bernd Reppich. On the dispersion strengthening mechanisms in ODS materials. International Journal of Materials Research, 93(7):605–613, July 2002.
- [55] Robert P. Smith and Steven D. Eppinger. Identifying Controlling Features of Engineering Design Iteration. Management Science, 43(3):276–293, March 1997.
- [56] William E. Frazier. Metal Additive Manufacturing: A Review. J. of Materi Eng and Perform, 23(6):1917–1928, June 2014.
- [57] Lauralyn McDaniel. NASA's New Additive Manufacturing Material Built to Withstand Extreme Conditions.

<https://additivemanufacturing.com/2022/04/20/nasas-new-additive-manufacturing-material-built-to-withstand-extreme-conditions/>, April 2022.

- [58] ARPA-E's HITEMMP Program | High Intensity Thermal Exchange through Materials, and Manufacturing Processes. <http://arpa-e.energy.gov/technologies/programs/hitemmp>, August 2018.
- [59] Robert Schafrik and Robert Sprague. Superalloy Technology - A Perspective on Critical Innovations for Turbine Engines. Key Engineering Materials - KEY ENG MAT, 380:113–134, March 2008.
- [60] D. B. Arnold and L. J. Jr Klinger. Dispersion-Strengthened Nickel Base Alloys. In OXIDE DISPERSION STRENGTHENING, volume 47, pages 611–635, Bolton Landing, NY, 1966. Gordon and Breach, Science.
- [61] Liming Tan, Yunping Li, Feng Liu, Yan Nie, and Liang Jiang. Microstructure evolutions of a powder metallurgy superalloy during high-strain-rate deformation. Journal of Alloys and Compounds, 789:506–517, June 2019.
- [62] Haibo Long, Shengcheng Mao, Yinong Liu, Ze Zhang, and Xiaodong Han. Microstructural and compositional design of Ni-based single crystalline superalloys — A review. Journal of Alloys and Compounds, 743:203–220, April 2018.
- [63] Anthony De Luca, Christoph Kenel, Joanna Pado, Shreyas S. Joglekar, David C. Dunand, and Christian Leinenbach. Thermal stability and influence of Y₂O₃ dispersoids on the heat treatment response of an additively manufactured ODS Ni–Cr–Al–Ti γ/γ' superalloy. Journal of Materials Research and Technology, 15:2883–2898, November 2021.
- [64] S. H. Reichman and J. W. Smythe. New Developments in Superalloy Powders. In Henry H. Hausner, editor, Modern Developments in Powder Metallurgy, pages 73–84, Boston, MA, 1971. Springer US.
- [65] Blending and Premixing of Metal Powders and Binders[1]. In P. Samal and J. Newkirk, editors, Powder Metallurgy, pages 88–92. ASM International, 2015.
- [66] J. M. Torralba, P. Alvaredo, and Andrea García-Junceda. High-entropy alloys fabricated via powder metallurgy. A critical review. Powder Metallurgy, 62(2):84–114, March 2019.
- [67] J. J. Dunkley. 1 - Advances in atomisation techniques for the formation of metal powders. In Isaac Chang and Yuyuan Zhao, editors, Advances in Powder Metallurgy, Woodhead Publishing Series in Metals and Surface Engineering, pages 3–18. Woodhead Publishing, January 2013.

- [68] P. C. Collins, D. A. Brice, P. Samimi, I. Ghamarian, and H. L. Fraser. Microstructural Control of Additively Manufactured Metallic Materials | Annual Review of Materials Research. Annual Review of Materials Research, 46:63–91, July 2016.
- [69] Yevgeni Brif, Meurig Thomas, and Iain Todd. The use of high-entropy alloys in additive manufacturing. Scripta Materialia, 99:93–96, April 2015.
- [70] D. B. Miracle and O. N. Senkov. A critical review of high entropy alloys and related concepts. Acta Materialia, 122:448–511, January 2017.
- [71] M. Schneider, E. P. George, T. J. Manescau, T. Zálezák, J. Hunfeld, A. Dlouhý, G. Eggeler, and G. Laplanche. Analysis of strengthening due to grain boundaries and annealing twin boundaries in the CrCoNi medium-entropy alloy. International Journal of Plasticity, 124:155–169, January 2020.
- [72] C. E. Slone, J. Miao, E. P. George, and M. J. Mills. Achieving ultra-high strength and ductility in equiatomic CrCoNi with partially recrystallized microstructures. Acta Materialia, 165:496–507, February 2019.
- [73] Benay Uzer, S. Picak, J. Liu, T. Jozaghi, D. Canadinc, I. Karaman, Y. I. Chumlyakov, and I. Kireeva. On the mechanical response and microstructure evolution of NiCoCr single crystalline medium entropy alloys. Materials Research Letters, 6(8):442–449, August 2018.
- [74] J. Miao, C. E. Slone, T. M. Smith, C. Niu, H. Bei, M. Ghazisaeidi, G. M. Pharr, and M. J. Mills. The evolution of the deformation substructure in a Ni-Co-Cr equiatomic solid solution alloy. Acta Materialia, 132:35–48, June 2017.
- [75] Bernd Gludovatz, Anton Hohenwarter, Keli V. S. Thurston, Hongbin Bei, Zheng-gang Wu, Easo P. George, and Robert O. Ritchie. Exceptional damage-tolerance of a medium-entropy alloy CrCoNi at cryogenic temperatures. Nat Commun, 7(1):1–8, February 2016.
- [76] Bernd Gludovatz, Anton Hohenwarter, Dhiraj Catoor, Edwin H. Chang, Easo P. George, and Robert O. Ritchie. A fracture-resistant high-entropy alloy for cryogenic applications. Science, 345(6201):1153–1158, September 2014.
- [77] F. Otto, A. Dlouhý, K. G. Pradeep, M. Kuběňová, D. Raabe, G. Eggeler, and E. P. George. Decomposition of the single-phase high-entropy alloy CrMnFeCoNi after prolonged anneals at intermediate temperatures. Acta Materialia, 112:40–52, June 2016.
- [78] G. S. Ansell. The Mechanism of Dispersion-Strengthening: A Review. In OXIDE DISPERSION STRENGTHENING, volume 47, pages 61–141, Bolton Landing, NY, 1966. Gordon and Breach, Science.

- [79] Rc Benn. Microstructure and Property Relationships in Oxide Dispersion Strengthened Alloys. In Bl Bramfitt, Rc Benn, Cr Brinkman, and Gf Van-der Voort, editors, MiCon 86: Optimization of Processing, Properties, and Service Performance Through Microstructural Control, pages 238–238–31. ASTM International, 100 Barr Harbor Drive, PO Box C700, West Conshohocken, PA 19428-2959, January 1988.
- [80] Tim Smith. Producing Next Generation Superalloys Through Advanced Characterization and Manufacturing Techniques, January 2020.
- [81] R. O. Scattergood, C. C. Koch, K. L. Murty, and D. Brenner. Strengthening mechanisms in nanocrystalline alloys. Materials Science and Engineering: A, 493(1):3–11, October 2008.
- [82] T. E. Howson, D. A. Mervyn, and J. K. Tien. Creep and stress rupture of a mechanically alloyed oxide dispersion and precipitation strengthened nickel-base superalloy. Metall Mater Trans A, 11(9):1609–1616, September 1980.
- [83] SeungHyeok Chung, Bin Lee, Soo Yeol Lee, Changwoo Do, and Ho Jin Ryu. The effects of Y pre-alloying on the in-situ dispersoids of ODS CoCrFeMnNi high-entropy alloy. Journal of Materials Science & Technology, 85:62–75, September 2021.
- [84] Peng Chen, Chao Yang, Sheng Li, Moataz M. Attallah, and Ming Yan. In-situ alloyed, oxide-dispersion-strengthened CoCrFeMnNi high entropy alloy fabricated via laser powder bed fusion. Materials & Design, 194:108966, September 2020.
- [85] Igor Moravcik, Jan Cizek, Zuzana Kovacova, Jitka Nejezchlebova, Michael Kitzmantel, Erich Neubauer, Ivo Kubena, Vit Hornik, and Ivo Dlouhy. Mechanical and microstructural characterization of powder metallurgy CoCrNi medium entropy alloy. Materials Science and Engineering: A, 701:370–380, July 2017.
- [86] M. Soulier, A. Benayad, L. Teulon, Y. Oudart, S. Senol, and K. Vanmeensel. Nanocomposite powder for powder-bed-based additive manufacturing obtained by dry particle coating. Powder Technology, 404:117474, May 2022.
- [87] David J. am Ende, Stephen R. Anderson, and Jerry S. Salan. Development and Scale-Up of Cocrystals Using Resonant Acoustic Mixing. Org. Process Res. Dev., 18(2):331–341, February 2014.
- [88] Jian Wang, Jun Wang, Yaofeng Mao, Rufang Peng, and Fude Nie. The surface activation of boron to improve ignition and combustion characteristic. Defence Technology, 18(9):1679–1687, September 2022.

- [89] Su-Lan Yang, Ruixuan Xu, Wei He, Hongqi Nie, and Qi-Long Yan. Enhancing the thermal reactivity of AP crystals by coating of Al-based bi-metal nanocomposites. Fuel, 324:124588, September 2022.
- [90] Katie Jo Sunday and Mitra L. Taheri. NiZnCu-ferrite coated iron powder for soft magnetic composite applications. Journal of Magnetism and Magnetic Materials, 463:1–6, October 2018.
- [91] Jun Yang, Ales Sliva, Amit Banerjee, Rajesh N. Dave, and Robert Pfeffer. Dry particle coating for improving the flowability of cohesive powders. Powder Technology, 158(1):21–33, October 2005.
- [92] Bolun Han, Chengcheng Zhang, Kai Feng, Zhuguo Li, Xiancheng Zhang, Yao Shen, Xiaodong Wang, Hiroyuki Kokawa, Ruifeng Li, Zhiyuan Wang, and Paul K. Chu. Additively manufactured high strength and ductility CrCoNi medium entropy alloy with hierarchical microstructure. Materials Science and Engineering: A, 820:141545, July 2021.
- [93] Howard Mizes, Mary Ott, Elliott Eklund, and Dan Hays. Small particle adhesion: Measurement and control. Colloids and Surfaces A: Physicochemical and Engineering Aspects, 165(1):11–23, May 2000.
- [94] Stéphane Gorsse, Christopher Hutchinson, Mohamed Gouné, and Rajarshi Banerjee. Additive manufacturing of metals: A brief review of the characteristic microstructures and properties of steels, Ti-6Al-4V and high-entropy alloys. Science and Technology of Advanced Materials, 18(1):584–610, December 2017.
- [95] Theofilos Gatsos, Karim A. Elsayed, Yuwei Zhai, and Diana A. Lados. Review on Computational Modeling of Process–Microstructure–Property Relationships in Metal Additive Manufacturing. JOM, 72(1):403–419, January 2020.
- [96] S. Sun, M. Brandt, and M. Easton. Powder bed fusion processes. In Laser Additive Manufacturing, pages 55–77. Elsevier, 2017.
- [97] V. D. Divya, R. Muñoz-Moreno, O. M. D. M. Messé, J. S. Barnard, S. Baker, T. Illston, and H. J. Stone. Microstructure of selective laser melted CM247LC nickel-based superalloy and its evolution through heat treatment. Materials Characterization, 114:62–74, April 2016.
- [98] E. Hosseini and V. A. Popovich. A review of mechanical properties of additively manufactured Inconel 718. Additive Manufacturing, 30:100877, December 2019.
- [99] A. du Plessis and E. Macdonald. Hot isostatic pressing in metal additive manufacturing: X-ray tomography reveals details of pore closure. Additive Manufacturing, 34:101191, August 2020.

- [100] Subin Shrestha and Kevin Chou. Formation of keyhole and lack of fusion pores during the laser powder bed fusion process. Manufacturing Letters, 32:19–23, April 2022.
- [101] Jerard V. Gordon, Sneha P. Narra, Ross W. Cunningham, He Liu, Hangman Chen, Robert M. Suter, Jack L. Beuth, and Anthony D. Rollett. Defect structure process maps for laser powder bed fusion additive manufacturing. Additive Manufacturing, 36:101552, December 2020.
- [102] Pan Wang, Pengfei Huang, Fern Lan Ng, Wai Jack Sin, Shenglu Lu, Mui Ling Sharon Nai, ZhiLi Dong, and Jun Wei. Additively manufactured CoCrFeNiMn high-entropy alloy via pre-alloyed powder. Materials & Design, 168:107576, April 2019.
- [103] Fernando J. Alamos, Jessica Schiltz, Kirsten Kozlovsky, Ross Attardo, Charles Tomonto, Tom Pelletiers, and Steven R. Schmid. Effect of powder reuse on mechanical properties of Ti-6Al-4V produced through selective laser melting. International Journal of Refractory Metals and Hard Materials, 91:105273, September 2020.
- [104] Yiğit M. Arısoy, Luis E. Criales, Tuğrul Özel, Brandon Lane, Shawn Moylan, and Alkan Donmez. Influence of scan strategy and process parameters on microstructure and its optimization in additively manufactured nickel alloy 625 via laser powder bed fusion. Int J Adv Manuf Technol, 90(5):1393–1417, May 2017.
- [105] Sebastian Rott, Alexander Ladewig, Katrin Friedberger, Johannes Casper, Moritz Full, and Johannes Henrich Schleifenbaum. Surface roughness in laser powder bed fusion – Interdependency of surface orientation and laser incidence. Additive Manufacturing, 36:101437, December 2020.
- [106] Giovanni Strano, Liang Hao, Richard M. Everson, and Kenneth E. Evans. Surface roughness analysis, modelling and prediction in selective laser melting. Journal of Materials Processing Technology, 213(4):589–597, April 2013.
- [107] Youping Gao and John Malinzak. Selective Laser Melting Fundamentals and Its Applications for Rocket Engine Manufacturing. In Laser 3D Manufacturing II, Aro-jet Rocketdyne, Canoga Park, CA, February 2015.
- [108] Benjamin Wahlmann, Florian Galgon, Andreas Stark, Sören Gayer, Norbert Schell, Peter Staron, and Carolin Körner. Growth and coarsening kinetics of gamma prime precipitates in CMSX-4 under simulated additive manufacturing conditions. Acta Materialia, 180:84–96, November 2019.

- [109] Jinghao Xu, Hans Gruber, Donyong Deng, Ru Lin Peng, and Johan J. Moverare. Short-term creep behavior of an additive manufactured non-weldable Nickel-base superalloy evaluated by slow strain rate testing. Acta Materialia, 179:142–157, October 2019.
- [110] Haili Yao, Zhen Tan, Dingyong He, Zhenlu Zhou, Zheng Zhou, Yunfei Xue, Li Cui, Lijia Chen, Guohong Wang, and Ying Yang. High strength and ductility AlCrFeNiV high entropy alloy with hierarchically heterogeneous microstructure prepared by selective laser melting. Journal of Alloys and Compounds, 813:152196, January 2020.
- [111] Tadashi Fujieda, Hiroshi Shiratori, Kosuke Kuwabara, Takahiko Kato, Kenta Yamanaka, Yuichiro Koizumi, and Akihiko Chiba. First demonstration of promising selective electron beam melting method for utilizing high-entropy alloys as engineering materials. Materials Letters, 159:12–15, November 2015.
- [112] Wenqian Wu, Rui Zhou, Bingqiang Wei, Song Ni, Yong Liu, and Min Song. Nanosized precipitates and dislocation networks reinforced C-containing CoCrFeNi high-entropy alloy fabricated by selective laser melting. Materials Characterization, 144:605–610, October 2018.
- [113] Chenze Li, Michael Ferry, Jamie J. Kruzic, and Xiaopeng Li. Review: Multi-principal element alloys by additive manufacturing. J Mater Sci, 57(21):9903–9935, June 2022.
- [114] Andrea Huxol and Franz-Josef Villmer. DoE Methods for Parameter Evaluation in Selective Laser Melting. IFAC-PapersOnLine, 52(10):270–275, January 2019.
- [115] John A. Slotwinski and Edward J. Garboczi. Metrology Needs for Metal Additive Manufacturing Powders. JOM, 67(3):538–543, March 2015.
- [116] John A Wass. First Steps in Experimental Design— The Screening Experiment. page 9.
- [117] John S Benjamin. Mechanical alloying — A perspective. Metal Powder Report, 45(2):122–127, February 1990.
- [118] L Carter, M Attallah, and R Reed. Laser Powder Bed Fabrication of Nickel-base Superalloys: Influence of Parameters; Characterisation, Quantification and Mitigation of Cracking. page 10.
- [119] J. A. Slotwinski, E. J. Garboczi, P. E. Stutzman, C. F. Ferraris, S. S. Watson, and M. A. Peltz. Characterization of Metal Powders Used for Additive Manufacturing. J. RES. NATL. INST. STAN., 119:460, October 2014.

- [120] Zackary Snow, Richard Martukanitz, and Sanjay Joshi. On the development of powder spreadability metrics and feedstock requirements for powder bed fusion additive manufacturing. Additive Manufacturing, 28:78–86, August 2019.
- [121] F42 Committee. ASTM-F3049: Standard Guide for Characterizing Properties of Metal Powders Used for Additive Manufacturing Processes. Technical report, ASTM International, 2014.
- [122] F42 Committee. ASTM-52907: Additive Manufacturing–Feedstock Materials–Methods to Characterize Metallic Powders. Technical report, ASTM International, 2019.
- [123] B09 Committee. ASTM-B213: Standard Test Methods for Flow Rate of Metal Powders Using The Hall Flowmeter Funnel. Technical report, ASTM International, 2017.
- [124] Reza Baserinia, Katrina Brockbank, and Rajeev Dattani. Correlating polyamide powder flowability to mechanical properties of parts fabricated by additive manufacturing. Powder Technology, 398:117147, January 2022.
- [125] J. A. Bearden. X-Ray Wavelengths. Rev. Mod. Phys., 39(1):78–124, January 1967.
- [126] Kenton D. Childs, Brad A. Carlson, Lori A. LaVanier, John F. Moulder, Dennis F. Paul, William F. Stickle, and David G. Watson. Handbook of Auger Electron Spectroscopy. Physical Electronics, Inc., third edition, August 1995.
- [127] John F. Moulder, William F. Stickle, Peter E. Sobol, and Kenneth D. Bornben. Handbook of X-ray Photoelectron Spectroscopy. Perkin-Elmer Corporation, Physical Electronics Division, October 1992.
- [128] Atomic Weights and Isotopic Compositions for All Elements. https://physics.nist.gov/cgi-bin/Compositions/stand_alone.pl.
- [129] EOS M 100 - Ideal entry level model for industrial 3D printing. <https://www.eos.info/eos-m-100>.
- [130] Innovation Government of Canada. Volume correction factors—acetone (dimethyl ketone). <https://ised-isde.canada.ca/site/measurement-canada/en/laws-and-requirements/volume-correction-factors-acetone-dimethyl-ketone>, February 2017.
- [131] A.B. Spierings, M. Schneider, and R. Eggenberger. Comparison of density measurement techniques for additive manufactured metallic parts. Rapid Prototyping Journal, 17(5):380–386, January 2011.

- [132] RStudio.
- [133] James Gareth, Daniela Witten, Trevor Hastie, and Robert Tibshirani. An Introduction to Statistical Learning with Applications in R. Springer, 2013.
- [134] Hadley Wickham, Winston Chang, Lionel Henry, Thomas Lin Pedersen, Kohske Takahashi, Claus Wilke, Kara Woo, Hiroaki Yutani, Dewey Dunnington, and RStudio. Ggplot2: Create Elegant Data Visualisations Using the Grammar of Graphics, June 2021.
- [135] Kartikeya Bolar. STAT: Interactive Document for Working with Basic Statistical Analysis, April 2019.
- [136] Thibaut de Terris, Olivier Andreau, Patrice Peyre, Frédéric Adamski, Imade Koutiri, Cyril Gorny, and Corinne Dupuy. Optimization and comparison of porosity rate measurement methods of Selective Laser Melted metallic parts. Additive Manufacturing, 28:802–813, August 2019.
- [137] Pan Wang, Xipeng Tan, Chaoyi He, Mui Ling Sharon Nai, Ruoxuan Huang, Shu Beng Tor, and Jun Wei. Scanning optical microscopy for porosity quantification of additively manufactured components. Additive Manufacturing, 21:350–358, May 2018.
- [138] Zhenggang Wu. Temperature and Alloying Effects on the Mechanical Properties of Equiatomic FCC Solid Solution Alloys. Doctoral Dissertations, August 2014.
- [139] Xing Wang, Christopher M. Barr, Ke Jin, Hongbin Bei, Khalid Hattar, William J. Weber, Yanwen Zhang, and Karren L. More. Defect evolution in Ni and NiCoCr by in situ 2.8 MeV Au irradiation. Journal of Nuclear Materials, 523:502–509, September 2019.
- [140] Wenjia Wang, Jinqiang Ning, and Steven Y. Liang. Prediction of lack-of-fusion porosity in laser powder-bed fusion considering boundary conditions and sensitivity to laser power absorption. Int J Adv Manuf Technol, 112(1):61–70, January 2021.
- [141] W. H. Yu, S. L. Sing, C. K. Chua, C. N. Kuo, and X. L. Tian. Particle-reinforced metal matrix nanocomposites fabricated by selective laser melting: A state of the art review. Progress in Materials Science, 104:330–379, July 2019.
- [142] P. K. Farayibi, T. E. Abioye, A. Kennedy, and A. T. Clare. Development of metal matrix composites by direct energy deposition of ‘satellited’ powders. Journal of Manufacturing Processes, 45:429–437, September 2019.

- [143] Sebastian Haas, Anna M. Manzoni, Fabian Krieg, and Uwe Glatzel. Microstructure and Mechanical Properties of Precipitate Strengthened High Entropy Alloy Al₁₀Co₂₅Cr₈Fe₁₅Ni₃₆Ti₆ with Additions of Hafnium and Molybdenum. Entropy, 21(2):169, February 2019.
- [144] L. Jiang, Y. P. Lu, M. Song, C. Lu, K. Sun, Z. Q. Cao, T. M. Wang, F. Gao, and L. M. Wang. A promising CoFeNi₂V_{0.5}Mo_{0.2} high entropy alloy with exceptional ductility. Scripta Materialia, 165:128–133, May 2019.
- [145] Yuanyuan Shang, Jamieson Brechtel, Claudio Pistidda, and Peter Liaw. Mechanical Behavior of High-Entropy Alloys: A Review. February 2021.
- [146] Christopher K. H. Borg, Carolina Frey, Jasper Moh, Tresa M. Pollock, Stéphane Gorsse, Daniel B. Miracle, Oleg N. Senkov, Bryce Meredig, and James E. Saal. Expanded dataset of mechanical properties and observed phases of multi-principal element alloys. Sci Data, 7(1):430, December 2020.
- [147] Christoph Kenel, Anthony De Luca, Shreyas S. Joglekar, Christian Leinenbach, and David C. Dunand. Evolution of Y₂O₃ dispersoids during laser powder bed fusion of oxide dispersion strengthened Ni-Cr-Al-Ti γ/γ' superalloy. Additive Manufacturing, 47:102224, November 2021.
- [148] E04 committee. ASTM-E2627-13: Determining Average Grain Size Using Electron Backscatter Diffraction (EBSD) in Fully Recrystallized Polycrystalline Materials. Technical report, ASTM International, 2013.
- [149] E04 Committee. ASTM-E1382: Test Methods for Determining Average Grain Size Using Semiautomatic and Automatic Image Analysis. Technical report, ASTM International, 2010.
- [150] Subhashree Naik, Sudhansu Ranjan Das, and Debabrata Dhupal. Experimental Investigation, Predictive Modeling, Parametric Optimization and Cost Analysis in Electrical Discharge Machining of Al-SiC Metal Matrix Composite. Silicon, May 2020.
- [151] Usama Umer, Mustufa Haider Abidi, Jaber Abu Qudeiri, Hisham Alkhalefah, and Hossam Kishawy. Tool Performance Optimization While Machining Aluminium-Based Metal Matrix Composite. Metals, 10(6):835, June 2020.
- [152] Particle Size. https://www.horiba.com/en_en/products/scientific/particle-characterization/particle-size/.